

# Unequal Load-sharing in a Multi-stage Axial-flux Permanent Magnet Synchronous Machine

**James Ian Braid**

A dissertation submitted to the Faculty of Engineering and the Built Environment,  
University of the Witwatersrand, Johannesburg, in fulfilment of the requirements  
for the degree of Master of Science in Engineering.

Johannesburg, October 2011

# Declaration

I declare that this dissertation is my own, unaided work, except where otherwise acknowledged. It is being submitted for the degree of Master of Science in Engineering to the University of the Witwatersrand, Johannesburg. It has not been submitted before for any degree or examination in any other university.

Signed this \_\_\_ day of \_\_\_\_\_ 20\_\_

---

James Ian Braid.

# Abstract

Axial-flux machines, by the nature of their topology, are suited for high torque, low speed applications. In an attempt to improve the power-to-mass ratio of such a machine, the feasibility of stacking several alternate stator and rotor sections onto a common shaft in a multi-stage configuration was investigated. A prototype 5 kW double-stage machine was developed for comparison to other designs presented in the literature. Although the results appeared promising, whilst under evaluation, an unequal load-sharing anomaly was observed: even though both stages contributed to driving the load, one stage always dominated. Furthermore, the discrepancy appeared to be dependent on the direction of rotation. This research investigates and explains the cause of the unequal load-sharing and presents design considerations to aid the future development of multi-stage machines.

# Acknowledgements

For the life that I am fortunate enough to be living, the person that I am, and for the experiences and opportunities that I have had and will have, I am eternally grateful. To my family and friends, I thank them for their unending encouragement. My appreciation is especially due to Prof. Charles Landy, who after all these years, is still willing to read this thesis.

# Contents

<b>Abstract</b>	<b>ii</b>
<b>Acknowledgements</b>	<b>iii</b>
<b>Contents</b>	<b>iv</b>
<b>List of Figures</b>	<b>viii</b>
<b>List of Tables</b>	<b>xv</b>
<b>List of Symbols</b>	<b>xvii</b>
<b>1 Introduction</b>	<b>1</b>
1.1 Foreword to Problem . . . . .	1
1.2 Research Objectives . . . . .	2
1.3 Significance of Research . . . . .	2
1.4 Overview of Thesis . . . . .	2
<b>2 Research Background</b>	<b>4</b>
2.1 Axial-flux Machines . . . . .	4
2.1.1 The topology . . . . .	4
2.1.2 Permanent Magnet field excitation . . . . .	6

2.2	Application-based Design . . . . .	7
2.2.1	Stator-Rotor-Stator (SRS) sandwich . . . . .	7
2.2.2	Rotor-Stator-Rotor (RSR) sandwich . . . . .	8
2.2.3	Primary flux paths . . . . .	9
2.2.4	Stator windings . . . . .	11
2.2.5	Slotted stator cores . . . . .	11
2.2.6	Slotless stator cores . . . . .	12
2.3	Multi-stage Machines . . . . .	13
2.4	Multi-stage Prototype Machine . . . . .	14
2.4.1	Power-to-mass ratio . . . . .	15
2.5	Problem Identification . . . . .	17
<b>3</b>	<b>Derivation of Modelling Equations</b>	<b>20</b>
3.1	Overview of Synchronous Machine Theory . . . . .	20
3.1.1	Fundamentals of operation . . . . .	20
3.1.2	Equivalent circuit . . . . .	21
3.1.3	Phasor representation . . . . .	23
3.1.4	Influence of field excitation . . . . .	27
3.1.5	Influence of synchronous impedance . . . . .	28
3.1.6	Point of unity power factor . . . . .	29
3.1.7	Distinguishing points of operation . . . . .	30
3.2	Modelling Equations . . . . .	31
3.2.1	Current and RRA relationship . . . . .	32

3.2.2	Power Factor and RRA relationship . . . . .	35
3.2.3	Current and Power Factor relationship . . . . .	37
3.2.4	Power and RRA relationship . . . . .	44
3.3	Model Expansion for Multi-stage Machines . . . . .	46
<b>4</b>	<b>Modelling of Prototype Machine</b>	<b>54</b>
4.1	Quantization of Parameters . . . . .	54
4.1.1	Generator operation . . . . .	55
4.1.2	Winding resistance . . . . .	55
4.1.3	Characterisation of back EMF . . . . .	56
4.1.4	Measuring the Rotor Reference Angle (RRA) . . . . .	60
4.1.5	Determining the synchronous reactance . . . . .	61
4.1.6	Measuring the misalignment . . . . .	64
4.2	Completed Prototype Machine Model . . . . .	64
4.3	Model Predictions for Motoring Operation . . . . .	65
4.3.1	Current versus power factor . . . . .	65
4.3.2	Power factor versus RRA . . . . .	66
4.3.3	Current versus RRA . . . . .	69
4.3.4	Power versus RRA . . . . .	71
<b>5</b>	<b>Testing and Results</b>	<b>73</b>
5.1	Introduction to Testing . . . . .	73
5.2	Experimental Setup . . . . .	73
5.2.1	Prototype machine operating as a generator . . . . .	74

5.2.2	Prototype machine operating as a motor . . . . .	75
5.3	Verification of Models . . . . .	77
5.3.1	Synchronous reactance . . . . .	77
5.3.2	Individual stage models . . . . .	78
5.3.3	Model refinement . . . . .	79
5.4	Load Testing of Prototype Multi-stage Machine . . . . .	80
5.4.1	Verification of multi-stage models . . . . .	80
5.4.2	Refinement of multi-stage models . . . . .	80
5.4.3	Current versus load measurements . . . . .	84
5.4.4	Rotor misalignment . . . . .	87
5.4.5	Power factor versus load measurements . . . . .	90
5.4.6	Power versus load measurements . . . . .	94
<b>6</b>	<b>Review and Conclusion</b>	<b>96</b>
6.1	Review of Project . . . . .	96
6.2	Conclusion . . . . .	97
6.3	Future Work . . . . .	97
6.3.1	Considerations for future variations of the prototype . . . . .	98
6.3.2	Considerations for future developments . . . . .	98
	<b>References</b>	<b>102</b>
	<b>Appendix</b>	<b>104</b>

# List of Figures

2.1	Axial-flux and radial-flux topologies showing their primary flux paths (coloured) and principle dimensions. . . . .	5
2.2	Active conductors (thick coloured) and overhang (thin coloured) of an axial-flux and radial-flux stator. . . . .	5
2.3	Equivalent sized machines illustrating both sandwiching options respectively. . . . .	7
2.4	AFM with a SRS sandwich configuration in an industrial frame. The larger stator surface area allows for better cooling of the windings. . . . .	8
2.5	AFM in a RSR configuration used as an in-wheel drive where the two rotors form part of the wheel rim itself. . . . .	9
2.6	Resultant flux path through a RSR machine due to <i>unlike</i> poles aligned. . . . .	10
2.7	Resultant flux path through a RSR machine due to <i>like</i> poles aligned. . . . .	10
2.8	Resultant flux path through a double-stage RSR machine. Note the double-sided rotor sandwiched in the middle. . . . .	13
2.9	The prototype double-stage RSR machine. . . . .	15
2.10	Power distribution in the prototype machine for loads from no-load to full-load, rotating in the CW direction. . . . .	18
2.11	Power distribution in the prototype machine for loads from no-load to full-load, rotating in the CCW direction. . . . .	18
2.12	Individual power contributions from each stage, from no-load to full-load, for CCW rotation. . . . .	19

3.1	The steady-state per-phase equivalent circuit of a synchronous machine with motoring conventions. . . . .	22
3.2	The corresponding phasor diagram of an under-excited motor driving a heavy load. . . . .	23
3.3	Animated phasor diagrams of a motor driving loads of: 0, .25, .50, .75 and 1.00 pu respectively. Note the change of rotor reference angle and power factor. . . . .	24
3.4	Overlaid phasor diagrams from no-load (light orange) to full-load (dark brown). . . . .	25
3.5	Superimposed phasor diagrams of two machines, from no-load to full-load, having back EMFs of 0.75 pu (blue) and 0.80 pu (green), both with $R : X_S = 1 : 1$ . . . . .	27
3.6	Superimposed phasor diagrams of two machines, from no-load to full-load, having back EMFs of 0.75 pu (blue) and 0.80 pu (green), both with $R : X_S = 1 : 2$ . . . . .	28
3.7	Superimposed phasor diagram illustrating the influence of the field excitation on the power factor. Note the lagging (blue) and leading (green) power factors. . . . .	29
3.8	Phasor diagrams of distinguishing points corresponding to: no-load (orange), minimum current (red), and heavy load (brown). . . . .	30
3.9	Cosine rule triangle used to determine the current versus RRA $\sigma$ relationship. . . . .	32
3.10	General form of current versus RRA $\sigma$ relationship. . . . .	33
3.11	Current versus RRA $\sigma$ for two machines having back EMFs of 0.75 pu and 0.80 pu, both with $R : X_S = 1 : 1$ . . . . .	34
3.12	Current versus RRA $\sigma$ for two machines having back EMFs of 0.75 pu and 0.80 pu, both with $R : X_S = 1 : 2$ . . . . .	34
3.13	General form of power factor versus RRA $\sigma$ relationship. . . . .	36

3.14	Power factor versus RRA $\sigma$ for two machines having back EMFs of 0.75 pu and 0.80 pu, both with $R : X_S = 1 : 1$ . . . . .	38
3.15	Power factor versus RRA $\sigma$ for two machines having back EMFs of 0.75 pu and 0.80 pu, both with $R : X_S = 1 : 2$ . . . . .	38
3.16	Components of current versus RRA $\sigma$ : (a) parabola, (b) ellipse. . . . .	40
3.17	Resultant oval-shaped ellipse representing the current versus $\alpha$ function. . . . .	41
3.18	General form of current versus power factor relationship. . . . .	42
3.19	Current versus RRA $\sigma$ relationship for two machines having back EMFs of 0.75 pu and 0.80 pu, both with $R : X_S = 1 : 1$ . . . . .	43
3.20	Current versus RRA $\sigma$ relationship for two machines having back EMFs of 0.75 pu and 0.80 pu, both with $R : X_S = 1 : 2$ . . . . .	43
3.21	General form of power versus RRA $\sigma$ relationship. . . . .	44
3.22	Power versus RRA $\sigma$ relationship for two machines having back EMFs of 0.75 pu and 0.80 pu, both with $R : X_S = 1 : 1$ . . . . .	45
3.23	Power versus RRA $\sigma$ relationship for two machines having back EMFs of 0.75 pu and 0.80 pu, both with $R : X_S = 1 : 2$ . . . . .	45
3.24	Equivalent circuit of double-stage machine with parallel stages. . . . .	46
3.25	Multi-stage phasor diagrams for motoring in the CW and CCW directions respectively. . . . .	47
3.26	Animated phasor diagrams for motoring in the CW direction with <i>Stage2</i> (green) leading <i>Stage1</i> (blue), from no-load to full-load. . . . .	48
3.27	Animated phasor diagrams for motoring in the CCW direction with <i>Stage2</i> (green) lagging <i>Stage1</i> (blue), from no-load to full-load. . . . .	48
3.28	Current versus RRA $\sigma$ for CW rotation. Note that the <i>Stage2</i> minimum leads that of <i>Stage1</i> . . . . .	50
3.29	Current versus RRA $\sigma$ for CCW rotation. Note that the <i>Stage2</i> minimum lags that of <i>Stage1</i> . . . . .	50

3.30	Power factor versus RRA $\sigma$ for CW rotation. Note the equal $pf$ point in the $-\sigma$ quadrant. . . . .	51
3.31	Power factor versus RRA $\sigma$ for CCW rotation. Note the equal $pf$ point in the $+\sigma$ quadrant. . . . .	51
3.32	Current versus power factor; independent of any misalignment and direction of rotation. . . . .	52
3.33	Power versus RRA $\sigma$ for CW rotation from no-load to full-load. . . .	53
3.34	Power versus RRA $\sigma$ for CCW rotation from no-load to full-load. . .	53
4.1	The steady-state per-phase equivalent circuit of a synchronous generator. . . . .	55
4.2	Power generated by each stage versus total rated power. . . . .	56
4.3	Magnet B-H temperature curves with different points of operation marked for comparison. Refer to figure 4.4. . . . .	57
4.4	Temperature demagnetization profiles for the corresponding permeance lines. . . . .	58
4.5	Plotted back EMF measurements against increasing rotor temperatures. . .	60
4.6	Phase voltage and tacho pulse output waveforms when unloaded and loaded respectively, with the oscilloscope being triggered by the phase voltage. . . . .	61
4.7	Phasor diagram of generator under unity power factor load. . . . .	62
4.8	Synchronous reactances for each stage plotted against load current. .	63
4.9	Equivalent circuit of the prototype double-stage machine. Note the misalignment between the back EMFs results in <i>Stage2</i> lagging/leading <i>Stage1</i> by $+/- 0.8^\circ$ for CW and CCW rotation respectively. . . . .	65
4.10	Prototype models of current versus power factor for stages running individually; independent of the direction of rotation. . . . .	66
4.11	Prototype models of power factor versus RRA $\sigma$ for stages running individually; independent of the direction of rotation. . . . .	67

4.12	Prototype multi-stage model of power factor versus RRA $\sigma$ for rotation in the CW direction. Note the shift of <i>Stage2</i> to the right and hence the equal <i>pf</i> point in the $-\sigma$ quadrant. . . . .	68
4.13	Prototype multi-stage model of power factor versus RRA $\sigma$ for rotation in the CCW direction. Note the shift of <i>Stage2</i> to the left and hence the equal <i>pf</i> point in the $+\sigma$ quadrant. . . . .	68
4.14	Prototype models of current versus RRA $\sigma$ for stages running individually; independent of the direction of rotation. . . . .	69
4.15	Prototype multi-stage model of current versus RRA $\sigma$ for rotation in the CW direction. Note the current minimum of <i>Stage2</i> lagging by $\sigma \approx +1^\circ$ . . . . .	70
4.16	Prototype multi-stage model of current versus RRA $\sigma$ for rotation in the CCW direction. Note the current minimum of <i>Stage2</i> leading by $\sigma \approx -1^\circ$ . . . . .	70
4.17	Prototype models of power versus RRA $\sigma$ for stages running individually; independent of the direction of rotation. . . . .	71
4.18	Prototype multi-stage model of power versus RRA $\sigma$ for rotation in the CW direction. Note the decreased power contribution by <i>Stage2</i> . . . . .	72
4.19	Prototype multi-stage model of power versus RRA $\sigma$ for rotation in the CCW direction. Note the increased power contribution by <i>Stage2</i> . . . . .	72
5.1	Experimental setup for generator-based tests; shown for the individual testing of <i>Stage1</i> . . . . .	74
5.2	Experimental setup used for motoring tests; shown with both stages connected via variacs to emulate an infinite bus-bar supply. . . . .	75
5.3	Experimental setup used to run-up the prototype machine at start; shown with an inverter supplying <i>Stage1</i> via a knife switch. . . . .	76
5.4	Plotted RRA versus load current measurements proving their linear relationship. . . . .	77

5.5	Prototype models of current versus power factor for stages running individually, correlating with measurements from tests in the CCW direction. . . . .	78
5.6	Prototype models of current versus power factor verified with measurements for CW rotation. . . . .	81
5.7	Prototype models of current versus power factor verified with measurements for CCW rotation. . . . .	81
5.8	Refined prototype models of current versus power factor in correlation with measurements for CW rotation. . . . .	83
5.9	Refined prototype models of current versus power factor in correlation with measurements for CCW rotation. . . . .	83
5.10	Measured currents at corresponding rotor positions, from no-load to full-load, for CW rotation. The current minima are used to determine the rotor position offset from the RRA at $\sigma = 0$ . . . . .	85
5.11	Measured currents mapped onto individual RRA axes, corresponding from no-load to full-load, for CW rotation. . . . .	85
5.12	Measured currents at corresponding rotor positions, from no-load to full-load, for CCW rotation. The current minima are used to determine the rotor position offset from the RRA at $\sigma = 0$ . . . . .	86
5.13	Measured currents mapped onto individual RRA axes, corresponding from no-load to full-load, for CCW rotation. . . . .	86
5.14	Measured currents mapped onto a common <i>RRA</i> -axis, from no-load to full-load, for CW rotation. . . . .	88
5.15	Prototype model of currents versus RRA $\sigma$ in correlation with mapped measurements, from no-load to full-load, for CW rotation. . . . .	88
5.16	Measured currents mapped onto a common <i>RRA</i> -axis, from no-load to full-load, for CCW rotation. . . . .	89
5.17	Prototype model of currents versus RRA $\sigma$ in correlation with mapped measurements, from no-load to full-load, for CCW rotation. . . . .	89

5.18	Measured power factors at corresponding rotor positions, from no-load to full-load, for CW rotation. . . . .	90
5.19	Measured power factors at corresponding rotor positions, from no-load to full-load, for CCW rotation. . . . .	91
5.20	Measured power factors mapped onto a common <i>RRA</i> -axis, from no-load to full-load, for CW rotation. . . . .	92
5.21	Prototype model of power factor versus <i>RRA</i> $\sigma$ , in correlation with mapped measurements, from no-load to full-load, for CW rotation. . . . .	92
5.22	Measured power factors mapped onto a common <i>RRA</i> -axis, from no-load to full-load, for CCW rotation. . . . .	93
5.23	Prototype model of power factor versus <i>RRA</i> $\sigma$ , in correlation with mapped measurements, from no-load to full-load, for CCW rotation. . . . .	93
5.24	Prototype model of power versus <i>RRA</i> $\sigma$ , in correlation with mapped measurements, from no-load to full-load, for CW rotation. . . . .	95
5.25	Prototype model of power versus <i>RRA</i> $\sigma$ , in correlation with mapped measurements, from no-load to full-load, for CCW rotation. . . . .	95
6.1	Axial flux path through machine with an extended right-most airgap. . . . .	99
6.2	Transverse flux path through machine with an extended right-most airgap. . . . .	100
6.3	A toroidal flux path may be established from the use of (a) toroidal coils, (b) folded coils. . . . .	101
4	Coloured temperature strips on rotor backiron. . . . .	105
5	Holes in rotor backiron for insertion of temperature probes. . . . .	105
6	Power factor intersection point for CW rotation; by means of linear interpolation. . . . .	106
7	Power factor intersection point for CCW rotation; by means of quadratic interpolation. . . . .	106

# List of Tables

5.1	Refined equivalent circuit parameters used for the CW rotation models.	82
5.2	Refined equivalent circuit parameters used for the CCW rotation models. . . . .	82
5.3	Rotor position offsets determined from the current minima measured for CW rotation. . . . .	85
5.4	Rotor position offsets determined from the current minima measured for CCW rotation. . . . .	86
5.5	Current minima and corresponding RRAs for CW rotation. . . . .	88
5.6	Current minima and their corresponding RRAs for CCW rotation. . . . .	89
5.7	Points of equal power factor for CW rotation. . . . .	92
5.8	Point of equal power factor for CCW rotation. . . . .	93
1	Specifications of prototype multi-stage machine. . . . .	104
2	Dimensions of prototype multi-stage machine. . . . .	104
3	Instruments used to quantify the back EMF and winding resistance.	107
4	Principle equipment used in the generator experimental setup. . . . .	107
5	Instruments used to record primary measurements during generator tests. . . . .	107
6	Principle equipment used in motor experimental setup. . . . .	108
7	Instruments used to record primary measurements during motor tests.	108

8	Additional equipment used to perform inverter start. . . . .	108
9	Rotor backiron temperatures and corresponding back EMFs. . . . .	109
10	Measurements recorded during generator tests, conducted at synchronous speed, for increasing load. . . . .	109
11	Individual motoring tests, <i>Stage1</i> . . . . .	110
12	Individual motoring tests, <i>Stage2</i> . . . . .	110
13	Measurements recorded during motor tests with both stages connected in parallel, fed from a common 180 V supply, for increasing load. CW rotation. . . . .	111
14	Measurements recorded during motoring tests with both stages connected in parallel, fed from a common 180 V supply, for increasing load. CCW rotation. . . . .	112
15	Measurements recorded during motor tests with both stages connected in parallel, fed from a common 180 V supply, for increasing load. CW rotation. . . . .	113
16	Measurements recorded during motor tests with both stages connected in parallel, fed from a common 180 V supply, for increasing load. CCW rotation. . . . .	114

# List of Symbols

$V$	supply voltage
$I$	stator current
$E_0$	back EMF
$E$	resultant EMF
$R$	winding resistance
$X_L$	leakage reactance
$X_A$	armature-reaction reactance
$X_S$	synchronous reactance
$Z_S$	synchronous impedance
$\delta$	load angle
$\sigma$	rotor reference angle
$\theta$	power factor angle
$pf$	power factor
$\angle Z_S$	impedance angle
$\alpha$	acute reference angle

# Chapter 1

## Introduction

Axial-Flux Permanent Magnet Synchronous Machines (AFPMSMs) have found many new uses in high torque, low speed applications ranging from domestic washing machines to wind turbines to ship propulsion drives [1]. The topology of these machines is such that the flux links the disk-like stator and rotor cores in the axial plane. As a result, large torque moments are developed. With sufficient torque to drive loads directly, the need for a reduction gearbox and their inherent disadvantages becomes redundant. This allows the drive to be incorporated into the load itself; such as a spindle motor of a compact disk drive or a direct-drive washing machine drum. By stacking additional stator and rotor sections alternately onto a common shaft to form a multi-stage machine, even higher powers can be achieved, making them suitable for restricted volume applications [2]. An example of such a machine is an in-wheel drive for an electric vehicle.

### 1.1 Foreword to Problem

With this concept in mind, a multi-stage prototype machine was developed in an earlier final-year project for the investigation into these possibly increased power densities. Although the results yielded promising power-to-mass ratios, during testing, it was revealed that the load was unequally shared between the multiple stages, resulting in drawbacks that suppressed the gains. Subsequently, this research aims to investigate and to understand the causes of the unequal load-sharing, so that the knowledge may be used to benefit the future design of these machines.

## 1.2 Research Objectives

With this foundation in place, the aims of the research are to:

- Derive the underlying equations that are required to develop suitable models; for both multi-stage machines in general and the prototype under evaluation.
- Gain an understanding of the electrical relationships and electro-mechanical conversion process using the models and associated phasor diagrams.
- Perform experimental work to verify and refine the models against test data from the prototype machine.
- Identify the possible causes based on the knowledge gained from the modelling, and hence propose design considerations for future work.

The scope of this work is limited to single-stage and multi-stage AFPMSMs running as motors from a constant supply voltage. It may easily be adapted for machines used as generators. In some cases, the prototype machine was tested under generating conditions to determine certain equivalent circuit parameters. The modeling is focused on the relevant electrical relationships only, under steady-state conditions. Again, it may be expanded to include the mechanical interaction with the load, or modified to investigate transient responses.

## 1.3 Significance of Research

AFPMSMs play a promising role in the future design of load-incorporated, direct-drive machines as presented in the existing literature. Multi-stage machines offer comparatively higher power densities and several papers look into their design for various applications. The literature suggests that, to create a multi-stage machine, additional stator and rotor sections can simply be stacked onto a common shaft [1]. From the experience gained after construction of such a prototype, this suggestion proved to be naïve, and certainly not as effortless as anticipated.

## 1.4 Overview of Thesis

Chapter 2 reviews the literature on the design and application of AFPMSMs, introduces the multi-stage machine topology on which this research is primarily focused,

and identifies the problem from the anomalies observed whilst evaluating the prototype. Chapter 3 examines the relevant synchronous machine theory, derives the underlying equations from the equivalent circuits, and plots the general models for various important relationships. In Chapter 4 the prototype's equivalent circuit parameters are evaluated from experimentation and are subsequently used to model the machine. Chapter 5 presents the experimental setup and tests conducted, verifies and refines the models, and analyses the predicted and measured data. Finally, Chapter 6 reviews the overall project and proposes recommendations and future work.

## Chapter 2

# Research Background

Although the first electric motors invented were Axial-Flux Machines (AFMs), they were superseded relatively quickly by their Radial-Flux Machine (RFM) counterparts [3]. Whilst RFMs have since become the conventional topology, some specialised exceptions exist, one being printed circuit servomotors. With much research currently being undertaken into the possibility of improved power-to-mass ratios offered by AFMs, it is predicted that there will be renewed interest in these in the near future, especially in applications taking advantage of their unique qualities.

### 2.1 Axial-flux Machines

This section describes the nature and design of AFMs. It starts with the topology, looks at the field excitation, winding configurations, and then expands to multi-stage machines.

#### 2.1.1 The topology

Figure 2.1 illustrates the primary flux paths and principal dimensions of an axial-flux and a radial-flux machine respectively [3]. Unlike in a RFM (blue), the primary flux path (across the airgap) in an AFM (red) flows axially through the machine, parallel to the shaft. Subsequently, the active conductors are radially located, as illustrated in figure 2.2, hence the stator and rotor cores take on disk-like forms.

The main design limitation of a RFM is the converging flux path at the bottom of the rotor teeth. Careful design needs to be undertaken here to avoid saturation in the core material. Furthermore, since the rotor core has limited surface area for

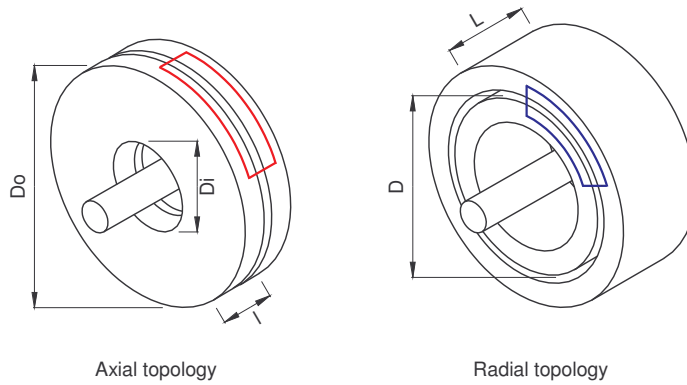


Figure 2.1: Axial-flux and radial-flux topologies showing their primary flux paths (coloured) and principle dimensions.

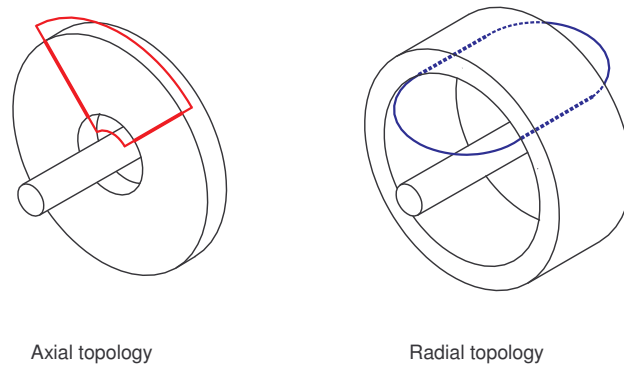


Figure 2.2: Active conductors (thick coloured) and overhang (thin coloured) of an axial-flux and radial-flux stator.

heat dissipation, special consideration needs to be given to cooling techniques. In an AFM however, the large facial surfaces on the outer sides of the stator and rotor cores radiate heat more effectively.

One disadvantage of the classical axial-flux topology is the strong magnetic attraction that exists between the stator and rotor sections, trying to close the airgap. In a RFM, since the rotor is concentrically positioned inside the stator, the magnetic forces are inherently balanced. By implementing a sandwiched axial-flux configuration as described later in this chapter, this problem can be alleviated.

Referring to figures 2.1 and 2.2, the torque producing moment in an AFM is determined by the mean radius between the inner ( $D_i$ ) and outer ( $D_o$ ) diameters of the stator core. Similarly, the length of the active conductors is the difference in radii.

The active surface area is given by  $A = \frac{\pi}{4}(D_o^2 - D_i^2)$  and is independent of the axial length ( $l$ ). During the design process, the required active area governs the overall diameter, whilst the desired flux density in the stator and rotor backiron determines the axial length only [4]. The active surface area dimensions  $D_i$  and  $D_o$  are limited by the overhang congestion between the stator core and shaft, or frame respectively.

In a RFM, the torque producing moment is determined by the radius of the airgap diameter ( $D$ ). The active conductor length is set by the axial length ( $L$ ) of the stator core and the active surface area is given by  $\frac{\pi}{4}D^2L$ . Therefore during the design process, the required active area determines both the diameter and length of the machine. For a given framesize, the active surface area dimension  $D$  is limited by the thickness of the stator backiron, and  $L$  by the overhang congestion between the stator core and end-walls. The inner diameter of the rotor core is limited by saturation in the backiron. The remaining space between it and the shaft results in a poor volume utilization factor [5].

For two machines of the same power rating, generally speaking, the AFM will have a larger framesize and hence a greater moment, thus developing more torque. The larger mean diameter would allow for a higher pole count and as a result, the machine would rotate at a slower speed; resulting in the same output power as an RFM. And hence, the AFM yields its high torque, low speed characteristic [6]. The higher number of poles requires thinner stator and rotor backiron making the axial length substantially shorter in comparison [7].

### 2.1.2 Permanent Magnet field excitation

A synchronous machine with a Permanent Magnet (PM) field system, compared to a wire-wound one, draws no additional magnetizing current and hence surpasses in efficiency; for any power rating [8]. Since the field winding is typically installed on the rotor, a PM produced field makes the need for slip rings and their associated problems, redundant. Because the field flux ideally remains constant, the rotor backiron can be in the form of a solid steel disk.

With the high coercive forces exerted by today's rare earth magnets, very high power densities can be achieved, although assembly can be somewhat challenging. With the steady decrease in magnet material price, the cost of manufacturing these machines is becoming cheaper, aided too by the fewer and simpler parts. One disadvantage of a PM machine is its limited field weakening ability, as required by some synchronous applications such as traction drives [5].

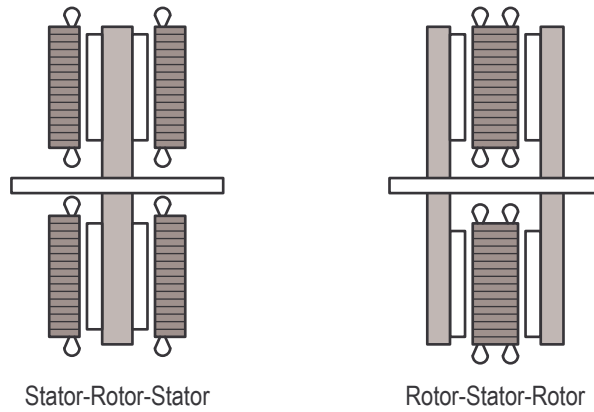


Figure 2.3: Equivalent sized machines illustrating both sandwiching options respectively.

## 2.2 Application-based Design

In the classical AFM topology, a strong magnetic axial force exists between the stator and rotor cores. Generally, angular contact bearings are required to carry the high axial load. As shown in figure 2.3, with the addition of another core, by sandwiching the alternate one between them e.g. a stator between two rotors, strong but balanced axial forces are exerted, cancelling each other. Similarly, a rotor can be sandwiched between two stators; the choice being motivated during design by the application. In both forms, the amount of active material (magnets, steel and copper volume) remains much the same resulting in little performance difference between either type. The key difference is the stator and rotor backiron surface areas, having an impact on cooling.

Whichever configuration is adopted, a *single-stage* machine is hereafter referred to. Both configurations and their applications are briefly reviewed.

### 2.2.1 Stator-Rotor-Stator (SRS) sandwich

For machines designed to undergo a significant temperature rise or with minimal forced cooling, having two stators sandwiching a rotor, for cooling reasons, is more beneficial. Since the primary source of losses are from the stator cores and their windings, the increased surface area on the back of the stator cores aids in heat dissipation, resulting in a lower temperature rise. Improved dissipation can be achieved with the addition of radiation fins onto these surfaces. The disadvantages of this configuration include the costs of the additional laminated stator core, and manufacture

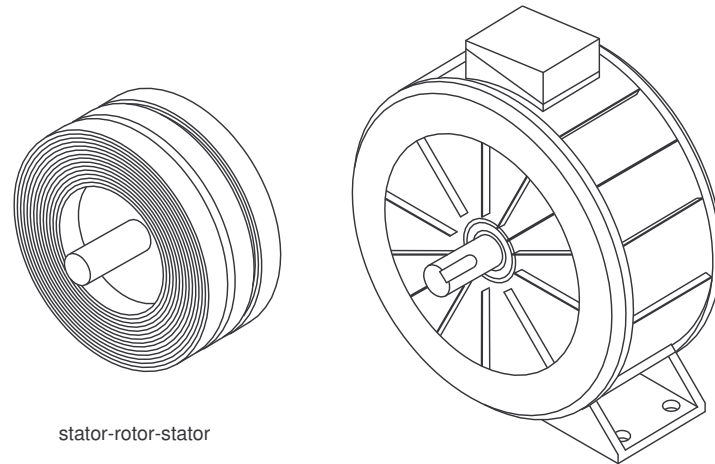


Figure 2.4: AFM with a SRS sandwich configuration in an industrial frame. The larger stator surface area allows for better cooling of the windings.

and installation of the second winding.

One benefit of sharing the stator windings between two cores is that, if connected in parallel, should an open-circuit fault occur in one, the machine remains operational, albeit at reduced power. With a single rotor comprising thicker permanent magnets, the magnet count is lower, simplifying the rotor assembly - permanent magnets are fickle components to handle and are the cause of many assembly difficulties.

Figure 2.4 illustrates an AFM where the sandwiched rotor is connected to the shaft and the stator fixed inside a frame. A typical domestic example of such a configuration may include a water pump drive, where the stator would be rigidly mounted onto a chassis or bed plate.

### 2.2.2 Rotor-Stator-Rotor (RSR) sandwich

For machines designed for applications where the shaft is fixed to a chassis and the frame rotates, it may be mechanically easier to sandwich a single stator (mounted to the shaft) between two rotors. In an in-wheel drive of an electric vehicle as illustrated in figure 2.5 for example, the two rotors could be incorporated into the wheel rim itself [9]. The major disadvantage is the minimal surface area of the laminated stator core from which heat can dissipate. However, the manufacture of a single stator core and winding is a gain.

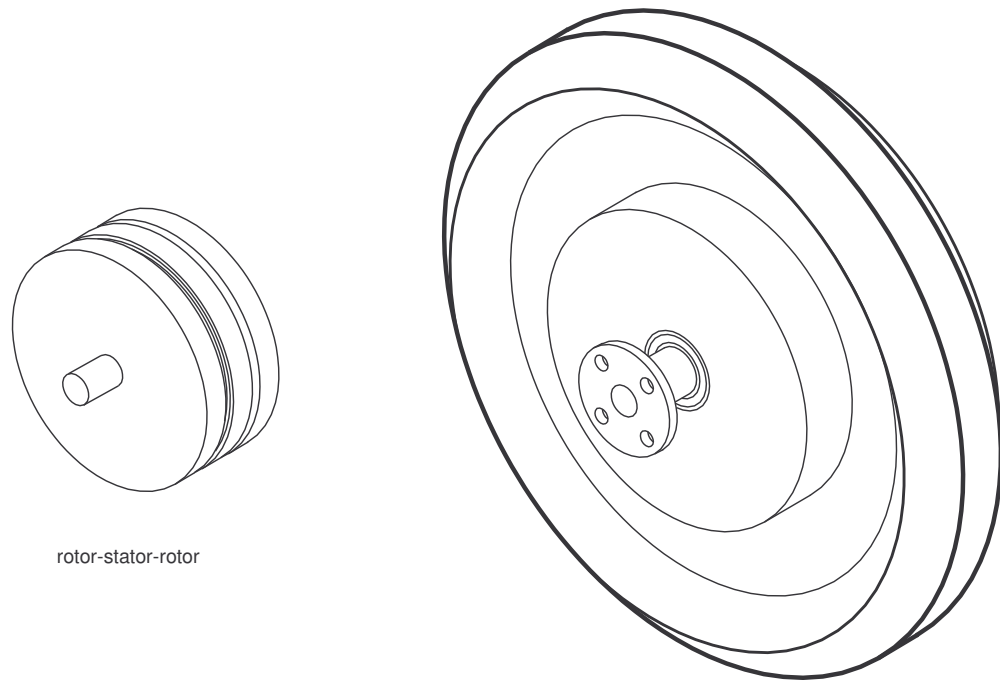


Figure 2.5: AFM in a RSR configuration used as an in-wheel drive where the two rotors form part of the wheel rim itself.

With two rotors, the magnet thickness is halved at the expense of a doubling in parts count. Since the rotor backiron is relatively straightforward to manufacture, the addition of a second one does not impose a major cost increase; unlike the manufacture of a second stator core and winding.

### 2.2.3 Primary flux paths

By sandwiching the stator between two rotors, depending upon the alignment of the rotors' magnet poles, one of two possible flux patterns can be established through the stator core, as illustrated in figures 2.6 and 2.7 [4].

Referring to fig. 2.6, by aligning *unlike* poles, one flux path links both rotors and is axially directed through the stator core. With *like* polarities aligned as in fig. 2.7, two flux paths symmetrically link each rotor with the stator, resulting in a transverse flux path through the stator core.

In the first instance, because the flux within the stator core is directed in one direction only, grain oriented silicon steel can be used to form the tape-wound laminated core. Since the axial length of the core has little effect on the reluctance of the

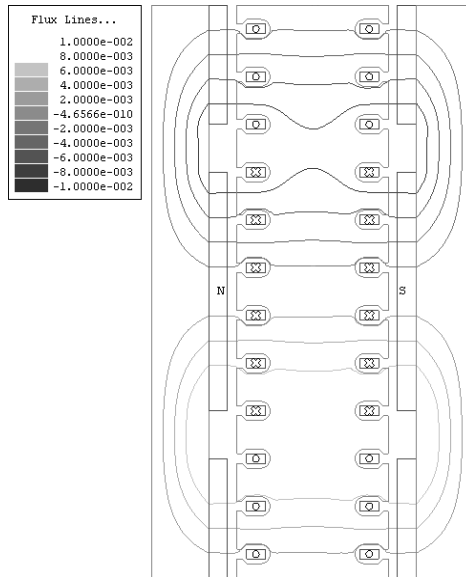


Figure 2.6: Resultant flux path through a RSR machine due to *unlike* poles aligned.

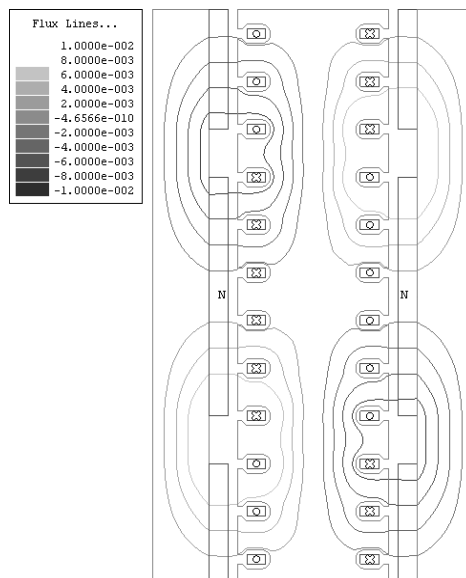


Figure 2.7: Resultant flux path through a RSR machine due to *like* poles aligned.

magnetic circuit, it can be reduced to a minimum, limited only by the necessary mechanical strength. In the second case however, since the flux is directed in two orthogonal directions, the steel required needs to be non-grain oriented, and thus the core will yield slightly higher iron losses. Due to the concentric flux path within the stator core, the reluctance of the magnetic circuit is dependent upon the cross-sectional area of the steel and hence the axial thickness must be chosen appropriately.

#### **2.2.4 Stator windings**

Referring to fig. 2.2, due to the topology of a RFM, the armature coil centre-lines can only point in a radial direction, thus the winding is located in slots around the inner diameter of the stator core. In an AFM, since the flux path through the stator can be oriented in one of two directions, the armature winding can take on two possible forms: either the coils can be installed into slots in the core with their center-lines pointing axially (as illustrated), or they can be toroidally wound around a slotless core. Both options are justified primarily by manufacturing arguments.

The core itself ideally needs to be iron-based, to direct maximum flux through the stator windings. Traditionally, steel laminations have been used. A current topic evident in the literature is the use of iron powder metallurgy to cast solid stator cores, with or without slots [6]. Research into the use of ironless cores has also been conducted, greatly simplifying construction [10], [11]. Tradeoffs include the extra volume of magnet material required, and larger leakage reactances. Despite this, for small machines, etching the armature winding onto an ironless PCB has a significant manufacturing advantage [12].

#### **2.2.5 Slotted stator cores**

Like RFMs, the stator core can be manufactured with slots, albeit radially directed, on one or both sides of the core. Cutting the slots into the steel can be done using one of a few methods. Either, whilst rolling the strip steel into a toroidal core, a CNC punch can stamp out slots at the required tooth pitch; the slot shape determined by the profile of the die - ideally semi-closed. Or, once the core has been rolled, slots can be milled into it with a milling machine. In this case, the slot shape is given by the profile of the end-mill, generally parallel sided. This method is very time consuming and uneconomical; suitable for prototype manufacturing only. Alternatively, a combination of radially- and axially-oriented laminations can be combined together [13]. This however results in a lower iron utilization factor.

Since the end-windings depend on the pole pitch, and inner and outer diameters of the stator core, a fairly significant overhang is inherent, especially around the outer diameter. By increasing the number of poles, the pole pitch decreases, shortening the length of the overhang. Irrespectively, the copper utilization is poor, resulting in higher copper losses. Due to the slotted nature, the airgap is smaller but the (albeit higher) flux distribution may contain a tooth harmonic, transmitted to the load as a torque ripple. Associated with the slotted core are tooth saturation problems and additional iron losses in the teeth. Although the efficiencies of this stator design are not the highest achievable, it follows traditional manufacturing techniques and benefits from being easier to assemble [14].

### 2.2.6 Slotless stator cores

Alternatively, the armature winding can be toroidally wound around the stator core, thus requiring no slots to house the coils. With the complete lack of slots, the associated tooth harmonic is eliminated, establishing a smooth flux distribution in the airgap and hence no torque ripple. Furthermore, no tooth saturation problems or additional iron losses exist. Since the end-windings are governed by the axial length of the stator core only and are independent of the pole pitch, the copper utilization is very good resulting in minimal overhang and low copper losses [15], [16].

The difficulty with such a stator design is the process of toroidally winding the copper coils around the core. From the literature survey, one solution is to segment the stator core into wedge-shaped sections, each with an individual winding installed [1]. This method requires the accurate alignment of the adjacent sections to minimize any small airgaps that may occur between the segment contact surfaces, resulting in lower core flux densities. Furthermore, to achieve a uniformly distributed winding over a segmented core may prove difficult. From a mechanical point of view, the rigidity of this structure would be inherently weak. Alternatively, with the careful setup of a toroidal winding machine, the copper conductors of each phase could be wound directly around the core into the desired coil groups. Mechanically, the solid-piece stator in this case would be far more rigid. Since the stator core is enshrouded by the winding, a major drawback of this design is the lack of, or very limited, options for fixing it to an external frame.

Because the windings are located on the surfaces of the stator core, to allow ample clearance between the rotors and coils, the physical airgap needs to be extended. In order to boost the otherwise low flux density in the longer airgap, a larger volume

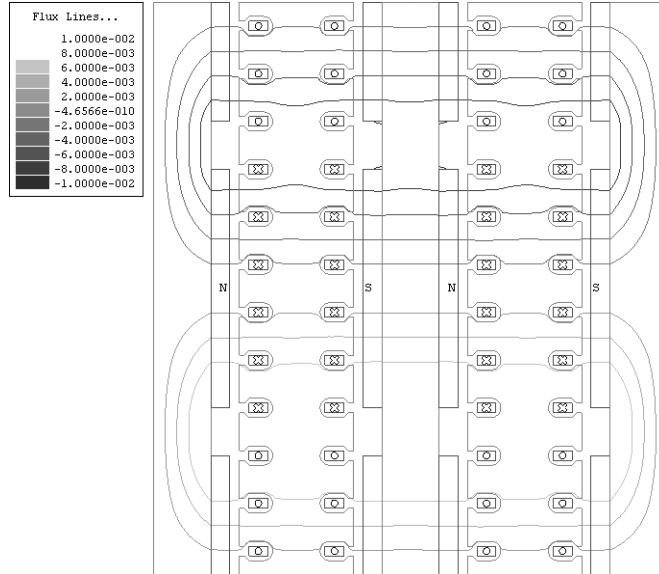


Figure 2.8: Resultant flux path through a double-stage RSR machine. Note the double-sided rotor sandwiched in the middle.

of permanent magnet material is required. The large airgap results in a higher reluctance path and hence increased leakage flux. Although this stator design results in the best efficiencies achievable, it does present some manufacturing challenges.

The first design results in a more compact machine with the greatest saving in iron and permanent magnet material, whilst the second results in the best utilization of copper and hence offers a higher efficiency.

## 2.3 Multi-stage Machines

Referring to figure 2.8, the MMF required to cross each airgap is sourced from the adjacent magnet pole. By stacking additional stages onto a common shaft, the MMF and flux density in each airgap remains unchanged. With parallel-connected windings, the phase coils are supplied with a common voltage and hence draw equal currents. Since the electric and magnetic loading of each stage is independent of the others, the total power rating is scaled by the number of stages [1]. For example, if a single stage is rated at 3 kW, by stacking two together, although the electric and magnetic loading constants do not change, the total deliverable power is doubled to 6 kW.

The advantages of stacking multiple stages include:

- More power from fixed framesizes. This is of particular benefit to in-wheel drive applications, where the framesize is limited by the inner diameter of the tyre. In this case, increasing the total power can be achieved with the addition of stages, extending the machine's axial length within the wheel hub only [2].
- Inherent parallel redundancy. Since each stage is independent of the others, should a fault occur in one, the inherent isolation allows the healthy stages to remain operational, albeit that the total deliverable power is derated. Should one stator winding be disconnected after a fault condition, the zero electrical loading would result in no power being contributed; as if that stage did not exist at all.
- Higher power densities. Since some of the active material is shared amongst adjacent stages, the resultant power-to-weight ratio improves with each addition. For example, in designs where two rotors are added back-to-back, they can be replaced by one double-sided rotor; it essentially being only one rotor core with permanent magnets mounted on both sides (as is the middle rotor in fig. 2.8).
- Single framesize manufacturing. Since machines of higher power ratings can be assembled by stacking multiple stages, the common framesize significantly reduces the costs and inventory associated with a range of different sized products. By means of an example, a 10 kW, 15 kW or 20 kW machine can be assembled from the same 5 kW stage parts, with the only difference being in the axial lengths of the respective machines. This ease of manufacture is probably the most significant benefit of employing a multi-stage configuration.

The fundamental assumptions made are that each stage is electro-magnetically and mechanically identical, shares a common supply voltage, and thus contributes equally to the load-sharing.

## 2.4 Multi-stage Prototype Machine

*Zhang et al* [14] compared several different types of AFMs to establish the optimum design, using the highest output power and efficiency with the lowest material mass as the criteria, for an electric vehicle in-wheel drive application. Their comparison consisted of machines comprising slotted and slotless stator cores, and surface- and

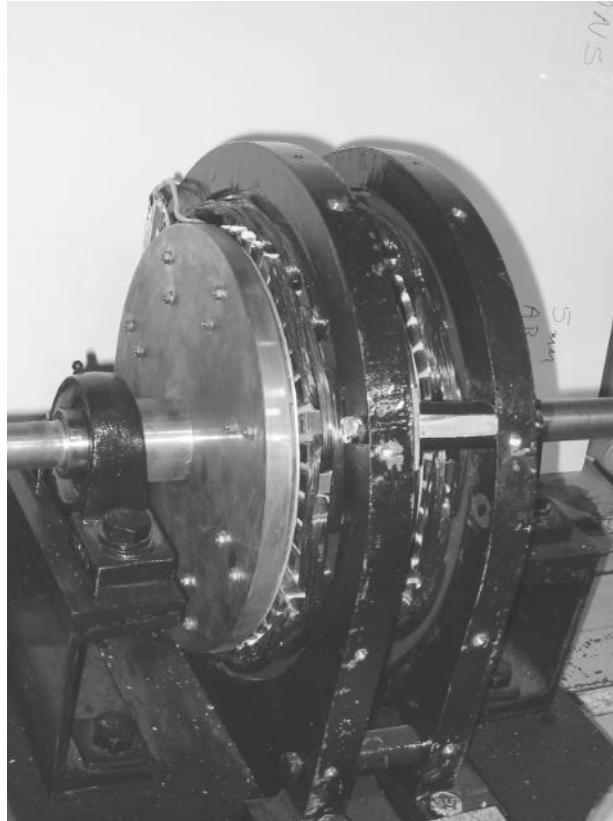


Figure 2.9: The prototype double-stage RSR machine.

interior-mounted PM rotors. They concluded that, to achieve their stipulated criteria above, a machine comprising a stator winding housed in a slotted core, with surface-mounted magnets on the rotor, would be the most optimum; despite the slotless designs having a more-sinusoidal airgap flux distribution.

From their conclusion, it was subsequently decided to develop such a prototype as a final-year project, to investigate the improvement of the power-to-mass ratios in multi-stage machines [17]. The specification ratings and mechanical dimensions of the prototype are given in tables 1 and 2 in the appendix respectively, and the machine itself is pictured in figure 2.9.

#### 2.4.1 Power-to-mass ratio

As described earlier, the sharing of common active material results in a higher power density; the ratio of power to mass. Experimental data gathered from the prototype double-stage machine was used for comparison to other similar sized multi-stage machines evaluated in [14].

From the results recorded, the improved power-to-mass ratios correlated well with [14]. Since the thickness of the mid-rotor backiron and stator core has little influence on the primary magnetic circuit, by minimizing them, the power-to-mass ratios can be maximized. This holds optimism for multi-stage Printed Circuit Board motors where the armature is etched onto a thin PCB; subsequently explored by the author [18]. A limit to the number of stages that can be stacked onto a common shaft is dictated by its mechanical strength and rigidity; especially should the situation arise where the compounded axial magnetic forces become slightly unbalanced. As the number of stages increases, so too must the axial load-rating of the bearings. Experience gained from construction of the prototype showed that the alignment of the stages and spacing of the airgaps is critical, and ironically almost impossible to achieve.

As promising as the results appear, whilst conducting experimental tests, two undesirable anomalies were observed:

- Rapid temperature rise of the rotor backiron. Whilst running, totally independent of the load applied, the rotor temperatures rose rapidly to reach a steady-state value of  $80^{\circ}\text{C}$ , not far below the Curie point of the permanent magnets. As concerning as this was, no immediate cause could be found. Although the rotor backiron is solid steel, assuming a sinusoidally distributed flux in the airgap and operating at synchronous speed, no obvious source of possible eddy currents could be established. Since the stator winding temperature was cooler, convective heating across the airgap could not be responsible. In the end, eddy currents, possibly caused by a non-synchronous zig-zag flux or a non-sinusoidal flux distribution in the airgap due to the wide parallel-sided slots, were assumed to be the cause.
- Unequal load-sharing between stages. The power drawn by each stage was not the same, implying that the load was unequally shared. Although both stages contributed to driving the load, one stage always dominated; the discrepancy being dependent on the direction of rotation. Along with this came unbalanced currents and a lower efficiency than expected. Subsequently, establishing the cause of the unbalanced load-sharing became the thrust of this research.

## 2.5 Problem Identification

With an electric vehicle in-wheel drive application in mind, the original aim of this research was to design a suitable four-quadrant controller for the prototype machine. However, the two anomalies observed rendered the prototype machine unsuitable as an in-wheel drive, and certainly unsuitable as a test platform for a control-related project. Before such a project can be undertaken, the design of the prototype machine needs to be reviewed and improved, so that the benefits it offers can be exploited to their full potential in its desired application.

The prototype machine comprises two stages connected in parallel, each rated to approximately 3 kW. Assuming, for illustration purposes only, that 100% of the power consumed by each stage is contributed to driving the load, by plotting each contribution against the total power drawn by the machine clearly demonstrates the unequal load-sharing. When loaded from no-load to full-load, figure 2.10 shows the power distribution while rotating in the clockwise direction, and similarly, figure 2.11 for counter-clockwise rotation.

To ensure that both stages produce 3 kW as claimed, each stage was run individually with the other open-circuited. Also, each stage was loaded whilst motoring in both directions. By plotting the power contribution of each stage against the sum of the two i.e. as if two smaller machines were coupled together and driving a common load, figure 2.12 shows that both machines contribute evenly, as expected. Although only plotted for rotation in the counter-clockwise direction, a similar if not identical graph would result for clockwise rotation.

Comparing the three graphs hints towards the possible cause. When running as a multi-stage machine, the load is unequally shared; yet when operating as two individual machines coupled together, power is contributed evenly. From an electromagnetic point of view, in the former, both stages share a common flux path, whilst in the latter, each stage is completely independent of the other. Therefore, it appears that the balance of the magnetic coupling of the two fields in the multi-stage configuration is somehow modified, leading to the power imbalance.

Consequently, the aim of this research is to investigate and understand the cause of the unbalanced load-sharing. With the subsequent knowledge gained, design considerations are proposed to aid the future development of such machines.

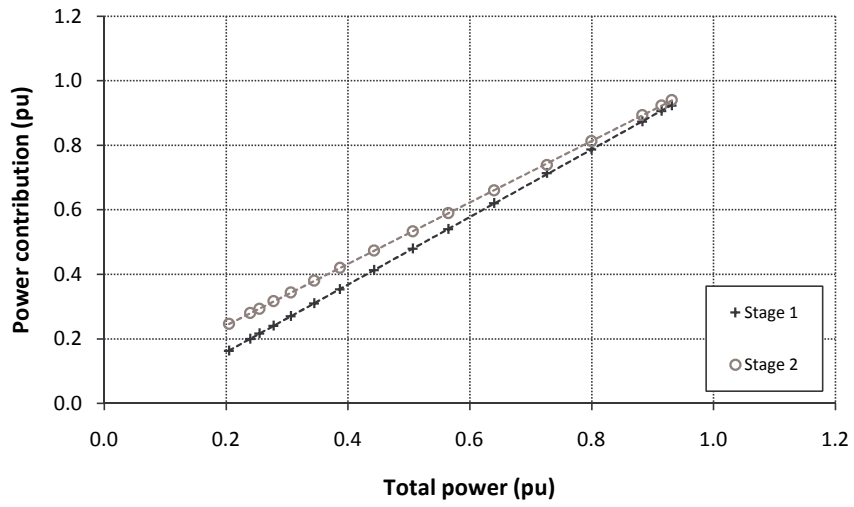


Figure 2.10: Power distribution in the prototype machine for loads from no-load to full-load, rotating in the CW direction.

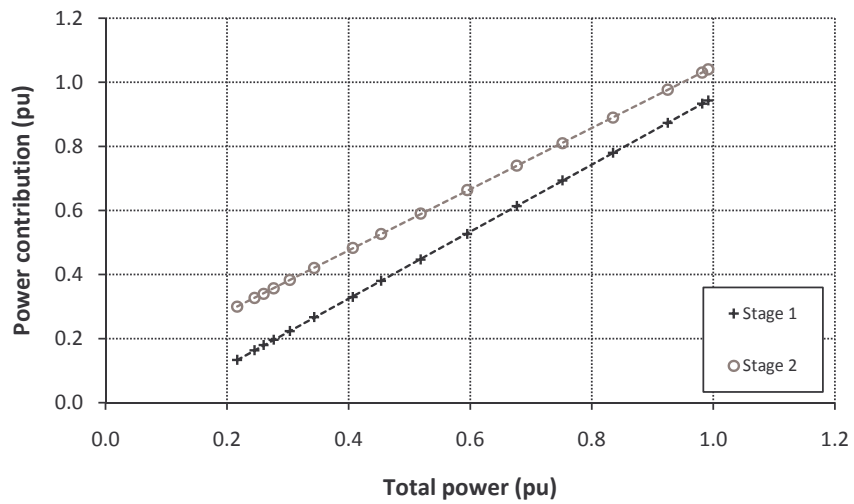


Figure 2.11: Power distribution in the prototype machine for loads from no-load to full-load, rotating in the CCW direction.

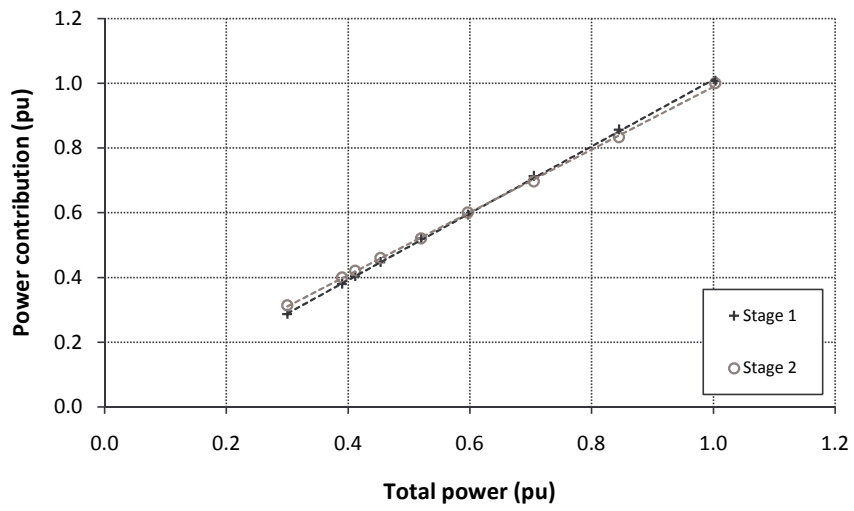


Figure 2.12: Individual power contributions from each stage, from no-load to full-load, for CCW rotation.

The underlying equations derived from synchronous machine theory are developed in the next chapter. These equations are used to develop general models for the key electrical relationships of these machines.

## Chapter 3

# Derivation of Modelling Equations

The problem identified in the prototype built is the unequal load-sharing between the two stages. It is therefore anticipated that the cause of the imbalance can be determined by exploring the relationship between the power drawn and the load power output for each stage.

This chapter begins with an overview of the relevant synchronous machine theory pertaining to motoring operation. From the equivalent circuit, the corresponding phasor diagrams are constructed, from which the modelling equations are derived. Models for the individual stages are developed and their characteristic relationships introduced. The stage models are then coupled together to represent a multi-stage machine. Finally, power-versus-load models for a multi-stage machine are derived.

### 3.1 Overview of Synchronous Machine Theory

Extensive literature exists on the operation of synchronous machines, one fine example is *Say* [19]. The text below is used merely to introduce the unfamiliar reader to the equivalent circuit and phasor diagrams. Since it pertains to the prototype, the theory reviewed focuses mainly on under-excited machines operating as motors.

#### 3.1.1 Fundamentals of operation

Briefly, a synchronous machine comprises two basic parts: a poly-phase *armature winding* (normally on the stator) that produces a travelling magnetic wave, and a *field winding* (on the rotor) that establishes constant flux poles across the air-gap. When the stator is energized, the interaction of the magnetic fluxes of the

armature- and field-windings result in a torque being produced on the rotor, and hence motoring operation. Conversely if the rotor is driven, the field flux induces phase voltages in the armature winding and generator operation takes place. In general, synchronous machines work equally well as a motor or generator and can metamorphose from one to the other whilst running - depending on the operating conditions.

When operating as a motor, the flux poles of the field 'lock-on' and rotate with the travelling magnetic wave developed by the rotating armature MMF, and hence the rotor turns at synchronous speed. The torque produced is proportional to the airgap flux density (hence field excitation) and armature current. The mechanical speed is synchronous and is directly proportional to the frequency of the supply. Assuming an ideal (frictionless) machine, under no-load conditions, the field and armature poles align directly opposite one another and the flux crosses the airgap perpendicularly. As the rotor is loaded mechanically, the field poles begin to drag behind the armature poles and the flux 'stretches' across the airgap. Despite the unaligned poles, the rotor continues to turn at synchronous speed; unlike an induction motor for example, where the rotor speed would slow down resulting in an increase in slip. When the rotor is too heavily loaded, the airgap flux becomes too 'stretched' across the airgap, the poles slip away from one another and the machine *stalls*. Because the angle of misalignment between the stator and rotor is proportional to the load, this angle is referred to as the *load angle*.

When operating as a generator, the rotating field poles induce phase voltages in the armature winding at a frequency synchronous with the rotor's speed. The magnitude and frequency of the voltage generated is proportional to the flux linkage and speed of rotation respectively. When rotating at a constant speed, the required output voltage can be controlled by varying the field excitation. By increasing the MMF of the field winding, more flux links with the armature across the airgap, resulting in a higher EMF being induced.

### 3.1.2 Equivalent circuit

The derivation of the steady-state per-phase equivalent circuit for a synchronous machine is well documented. In brief, the equivalent circuit is developed by considering the armature and field components individually, and their interaction with one another. Figure 3.1 illustrates the general equivalent circuit of a synchronous machine with motoring conventions.

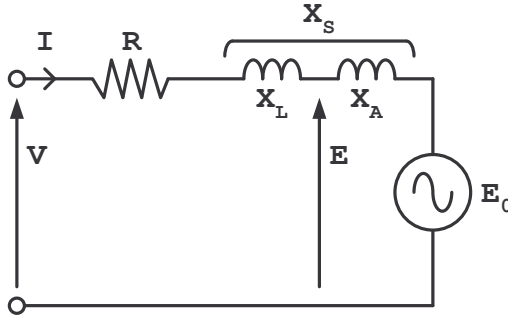


Figure 3.1: The steady-state per-phase equivalent circuit of a synchronous machine with motoring conventions.

The armature winding is represented by a *winding resistance* ( $R$ ) in series with a *leakage reactance* ( $X_L$ ). The field comprises either coils (connected via slip rings) or permanent magnets and links with the armature via the flux linkage across the airgap i.e. no direct electrical connection to the armature. Assuming that no MMF is dropped across the iron portion of the machine and that the magnetic circuit has a constant permeability (linear magnetization curve and constant airgap), the resultant flux across the airgap would be directly proportional to the total ampere-turns applied. Thus each MMF source in the magnetic circuit would produce its own flux component, resulting in a corresponding EMF in the armature winding. The MMF of the rotating field ( $F_0$ ) produced by either a DC field current or permanent magnets therefore induces a *back EMF* ( $E_0$ ) in the armature coils at synchronous frequency, leading  $\vec{F}_0$  by  $90^\circ$ . Similarly, the current ( $I$ ) flowing through the armature produces its own MMF ( $F_A$ ) and hence a corresponding EMF in the winding, seen as a voltdrop leading  $\vec{I}$  by  $90^\circ$ . Therefore the winding reaction to this MMF is modelled by the *reactance of armature reaction* ( $X_A$ ). Typically, synchronous machines have large airgaps (compared to induction machines) usually allowing any saturation effects to be ignored, hence  $X_A$  remains almost constant. The resultant EMF across the armature coils ( $E$ ) is due to the resultant MMF across the airgap ( $F$ ) and leads  $\vec{F}$  by  $90^\circ$ . With  $I$  flowing into the winding,  $R$  and  $X_L$  appear as two additional series voltdrops.

$$\vec{V} = \vec{E}_0 + \vec{I}\vec{Z}_S \quad (3.1)$$

Finally,  $X_L$  and  $X_A$  are combined as the *synchronous reactance* ( $X_S$ ) and together with  $R$ , are lumped as the *synchronous impedance* ( $Z_S$ ). Thus the modelling of a synchronous machine reduces to the vector expression given by 3.1.

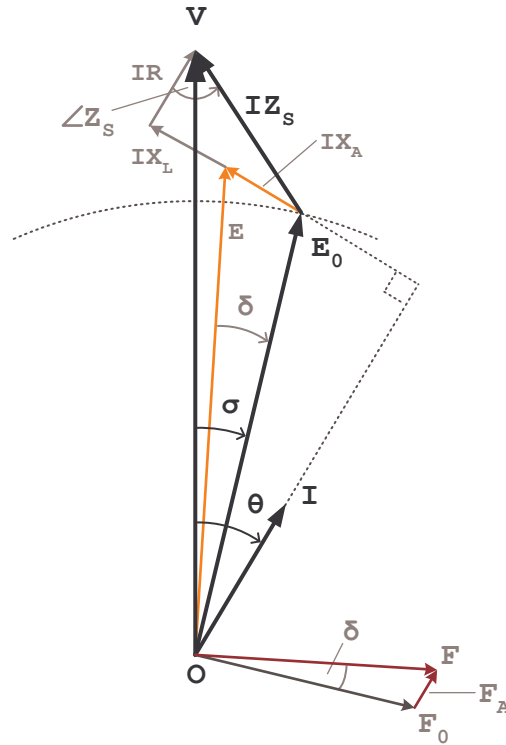


Figure 3.2: The corresponding phasor diagram of an under-excited motor driving a heavy load.

### 3.1.3 Phasor representation

The corresponding phasor diagram is illustrated in figure 3.2 <sup>1</sup>. This phasor diagram represents an under-excited motor (as is the prototype) with an *impedance ratio* ( $R : X_S$ ) of 1 : 2. For illustration purposes  $R$ ,  $X_L$  and  $X_A$  are made to have equal magnitudes. Starting with  $\vec{V}$  as a reference,  $\vec{E}_0$  lags by angle  $\sigma$ , proportional to the load being driven. In this document,  $\sigma$  is defined as the *Rotor Reference Angle* (*RRA*) since it relates the vector position of the field (on the rotor) with respect to the supply voltage. Similarly,  $\vec{I}$  lags  $\vec{V}$  by angle  $\theta$ , the *power factor angle*. For both angles, a negative or positive sign implies a *leading* or *lagging* vector respectively.

The magnitude of the back EMF  $E_0$  will remain constant if the field excitation, or MMF, is constant. Therefore any variation in load conditions will require the tip of  $\vec{E}_0$  to move along the arc of a circle with centre  $\hat{O}$  and radius proportional to  $|\vec{E}_0|$ . Since  $V$  and  $E_0$  are constant, the voltdrop across  $\vec{I}\vec{Z}_S$  represents the current  $I$  because  $Z_S$  is constant.

<sup>1</sup>The primary vectors on which the modelling equations are based are printed in dark bold type.

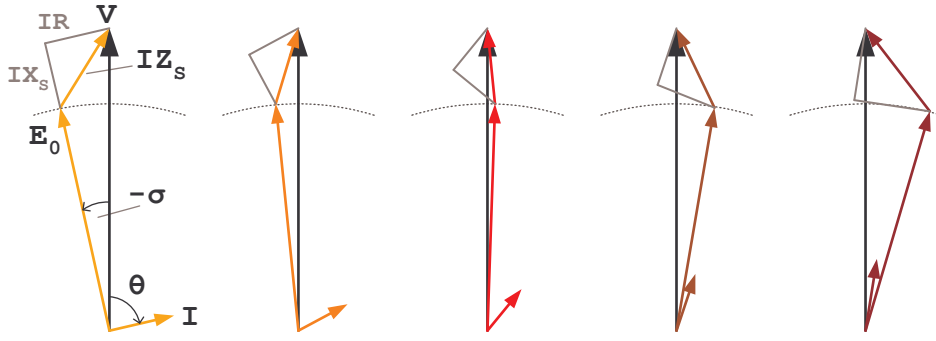


Figure 3.3: Animated phasor diagrams of a motor driving loads of: 0, .25, .50, .75 and 1.00 pu respectively. Note the change of rotor reference angle and power factor.

Consequently, the greater the angle between  $\vec{V}$  and  $\vec{E}_0$ , the larger is the current drawn. Due to the geometry of the triangle constructed by  $\vec{V}$ ,  $\vec{E}_0$  and  $I\vec{Z}_S$ ,  $\sigma$  and  $\theta$  are inter-dependent. Hence, as the load changes, so too does the power factor.

The *load angle* is defined as the angle  $\delta$  between the *flux axis* ( $\vec{F}$ ) and the *pole axis* ( $\vec{F}_0$ ), as shown in fig. 3.2 [20]. Under no-load conditions, the resultant flux crosses the airgap perpendicularly such that  $\vec{F}$  and  $\vec{F}_0$  are inline with one another. As the mechanical load increases, the resultant flux crosses the airgap obliquely such that  $\vec{F}_0$  lags  $\vec{F}$  by  $\delta$ , until maximum torque is reached at  $90^\circ$ .

Since triangle  $E - \hat{O} - E_0$  is similar to  $F - \hat{O} - F_0$ , the load angle is preserved in the electrical equivalent circuit as the angle between  $\vec{E}$  and  $\vec{E}_0$ . As a rough approximation, by assuming that  $R$  and  $X_L$  are significantly smaller than  $X_A$ , then  $\vec{V} \approx \vec{E}$  and hence  $\sigma \approx \delta$ .

Because  $X_S$  cannot be split easily into its components  $X_L$  and  $X_A$ , determining the magnitude and direction of  $\vec{E}$  (and hence  $\delta$ ) is difficult, and even more so to physically measure when in operation. In contrast  $\sigma$ , the angular displacement between  $\vec{V}$  (the supply voltage) and  $\vec{E}_0$  (the quadrature-axis of the rotor), is simple to measure.

Although the load angle  $\delta$  and rotor reference angle  $\sigma$  are proportional (albeit not directly) to one another, by expressing the amount of loading in terms of  $\sigma$  instead of  $\delta$ , significantly simplifies the modelling and experimentation. Consequently, splitting  $X_S$  into its two components is no longer necessary. The relationship between the rotor reference angle and load is illustrated in the animation of figure 3.3 where the machine is loaded from no-load to full-load.

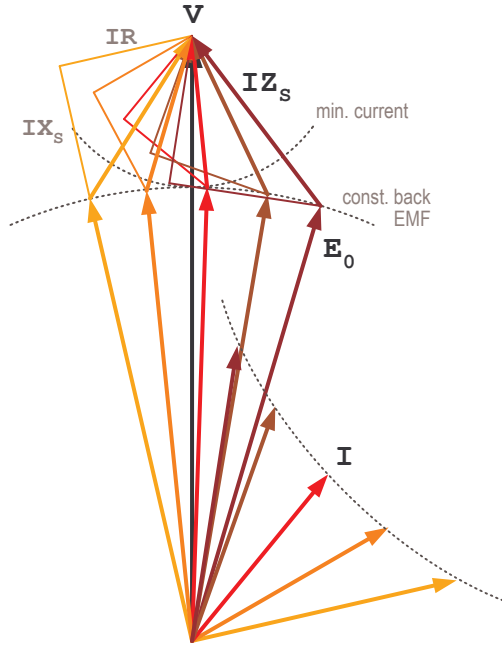


Figure 3.4: Overlaid phasor diagrams from no-load (light orange) to full-load (dark brown).

Under no-load conditions, due to the similar triangles (refer to fig. 3.2),  $\vec{E}_0$  and  $\vec{I}X_A$  would be in phase with one another. As a result,  $\vec{E}_0$  and  $\vec{I}X_S$  are inline and  $\vec{E}_0$  leads  $\vec{V}$  by  $-\sigma$ . Since  $\vec{I}$  is in phase and parallel with  $\vec{I}R$ , a poor power factor results. As the load increases, the top of the  $\vec{E}_0$  phasor moves along an arc of constant excitation. Consequently, the load angle increases and  $\sigma$  increases from leading  $\vec{V}$  to being inline with it, to lagging it. As a result of the new scaling and orientation of the right-angled triangle  $\vec{I}Z_S$  (with components  $\vec{I}R$  and  $\vec{I}X_S$ ), the magnitude of the current decreases to a minimum before increasing again, whilst the power factor improves from approximately zero towards unity.

These two relationships with respect to the load generally characterize synchronous motors and are the foundations on which the models are built. For clarity, the phasor diagrams in fig. 3.3 are redrawn overlying one another in figure 3.4 <sup>1</sup>.

<sup>1</sup>The locus of constant field excitation is represented by a dashed arc. For comparison of the stator currents, a locus with a radius equal to the minimum current is also represented by a dashed arc. A third dashed arc illustrates the magnitude of the current for increasing loads.

### Current versus load relationship

On no-load, the large difference between  $\vec{V}$  and  $\vec{E}_0$  (i.e.  $\vec{I}\vec{Z}_S$ ) due to a large  $-\sigma$  results in a significant current being drawn. As the motor is loaded the current decreases as the tail of the  $\vec{I}\vec{Z}_S$  vector moves with  $\vec{E}_0$  to a minimum when  $\vec{V}$  and  $\vec{E}_0$  are inline, at  $\sigma = 0$ . If the load increases further, as  $\sigma$  increases, the current similarly rises. The magnitude of the current is determined from the  $|\vec{I}\vec{Z}_S|$  phasor and changes marginally from no-load to full-load. Hence as a first approximation,  $|\vec{I}|$  may be assumed to remain constant.

### Power factor versus load relationship

On no-load, the power factor starts at a poor lagging value. As the load angle increases, the power factor improves steadily towards unity. With  $|\vec{V}|$  remaining constant and  $|\vec{I}|$  approximately constant, as a fair approximation, the input power ( $P = VI \cos \theta$ ) is directly proportional to the power factor. Since the power factor is proportional to the power drawn from the supply it is approximately proportional to the power delivered to the load.

Further geometrical analysis reveals that the limits within which the power factor varies corresponding to no-load and full-load, are determined mainly by the difference in the magnitudes of  $\vec{V}$  and  $\vec{E}_0$ , with the ratio  $R : X_S$  having a lesser effect. This is further discussed in sections 3.1.4 and 3.1.5.

### Current versus power factor relationship

Comparing the current vectors in fig. 3.4, a characteristic relationship exists between the magnitude and direction (i.e. power factor) of the currents. Since the power factor can be considered proportional to load, this relationship gives a convenient approximation of the current versus load; requiring simple electrical measurements only.

Three characteristics of the relationship are evident: on no-load, a high current is drawn at a poor power factor; at a certain load level, minimum current is drawn when  $pf = \cos(\angle Z_S)$ ; as the load increases further, the current rises and the power factor continues to improve towards unity.

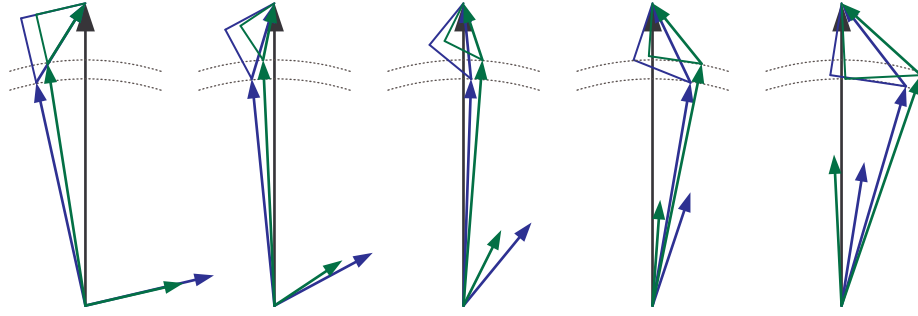


Figure 3.5: Superimposed phasor diagrams of two machines, from no-load to full-load, having back EMFs of 0.75 pu (blue) and 0.80 pu (green), both with  $R : X_S = 1 : 1$ .

The influence of the field excitation and synchronous impedance on these relationships is now briefly investigated. Like the theory above, the supply voltage ( $V$ ), back EMF ( $E_0$ ) and synchronous impedance ( $Z_S$ ) are assumed to remain constant with varying loads.

### 3.1.4 Influence of field excitation

By increasing the field excitation, more flux is established in the airgap and hence a higher back EMF is induced in the stator winding. With reference to fig. 3.4, an increased  $E_0$  for a constant  $V$  results in a smaller voltdrop between  $\vec{V}$  and  $\vec{E}_0$ . Therefore the  $IZ_S$  triangle is smaller and less current is drawn. This is illustrated in figure 3.5 where the phasor diagrams of two machines, from no-load to full-load, are superimposed for comparison. Both machines comprise the same synchronous impedances ( $R : X_S = 1 : 1$ ) however the first machine has a back EMF of  $E_0 = 0.75$  pu whilst the second has  $E_0 = 0.80$  pu. For the corresponding vector labels and loading annotations, refer to fig. 3.3. The response to the increased back EMF is clear and is briefly discussed.

On no-load, the respective  $IZ_S$  triangles are similarly oriented, resulting in equal power factor angles. The different magnitudes of  $IZ_S$  result in large, but unequal currents. As the machines are loaded, the shrinking  $IZ_S$  triangles result in current minima and the power factor angles start to diverge. Towards full-load, despite the diverging power factors, the geometry of the enlarging  $IZ_S$  triangles result in almost equal currents. And finally at full-load, with the demonstration values used, a condition of equal currents results; one with a leading power factor. The swing of  $\vec{E}_0$  about  $\vec{V}$  from no-load to full-load is approximately symmetrical.

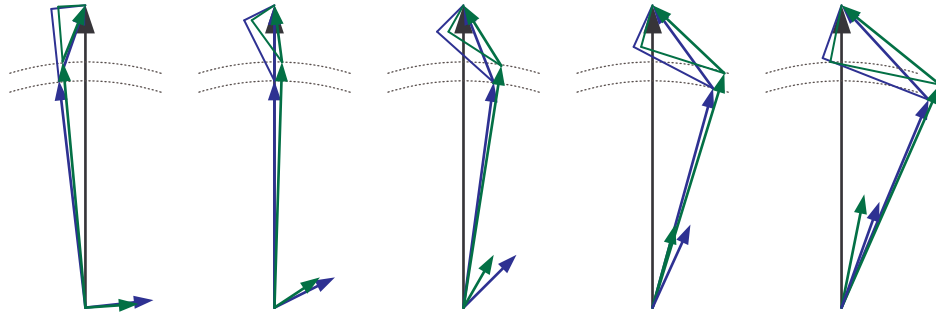


Figure 3.6: Superimposed phasor diagrams of two machines, from no-load to full-load, having back EMFs of 0.75 pu (blue) and 0.80 pu (green), both with  $R : X_S = 1 : 2$ .

The stator current and power factor can be controlled by the field excitation within the machine. Having a larger  $E_0$  results in a smaller voltdrop across  $\vec{I}Z_S$  and hence a lower current. A larger  $E_0$  also results in the tangential  $\vec{I}Z_S$  to the locus of  $E_0$  approaching horizontal and hence a unity (or even leading) power factor.

### 3.1.5 Influence of synchronous impedance

The synchronous impedance may be considered constant if any temperature variations (affecting the winding resistance) and saturation effects (affecting the synchronous reactance) are ignored; a fair assumption for synchronous machines operating under normal conditions.

In comparison with a machine having the same back EMF, a larger  $Z_S$  implies a lower current drawn. Comparing machines with unequal impedance ratios, the power factors would be different. Figure 3.6 shows the superimposed phasor diagrams of two machines with different back EMFs, but with the same synchronous impedances ( $R : X_S = 1 : 2$ ). Comparing figures 3.5 and 3.6 the effects of the field excitation and synchronous impedance are both evident.

Although the magnitudes of  $\vec{V}$  and  $\vec{E}_0$  are equal to those in fig. 3.5 resulting in the same magnitudes of  $\vec{I}Z_S$ , due to the larger  $Z_S$ , the magnitude of the currents are smaller. On no-load, since the  $\vec{I}Z_S$  triangles are no longer isosceles, the shorter resistive base ( $\vec{I}R$ ) lies almost horizontal, resulting in power factors of close to zero. Again, the different sized triangles having the same orientation results in equal power factors but unequal currents. As the machines are loaded, the  $\vec{I}Z_S$  triangles shrink to minima, as before. Since  $X_S \gg R$ , the difference in the back EMFs has an almost

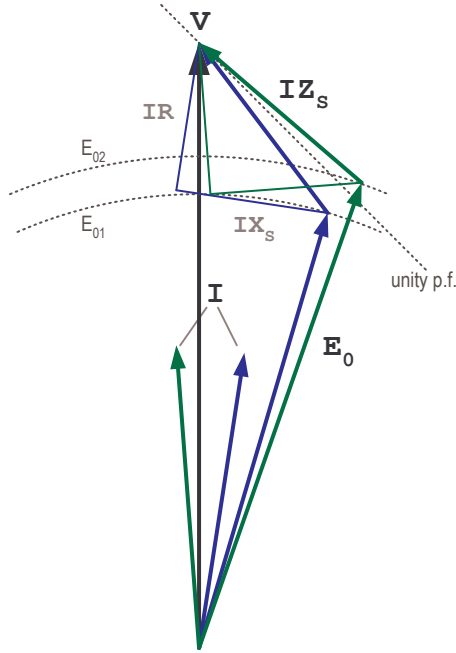


Figure 3.7: Superimposed phasor diagram illustrating the influence of the field excitation on the power factor. Note the lagging (blue) and leading (green) power factors.

negligible effect on the  $\vec{IR}$  vectors and hence only slight differences in currents and power factors result. The swing of  $\vec{E}_0$  about  $\vec{V}$  is no longer symmetrical and is clearly due to the shape of the  $IZ_S$  triangles.

### 3.1.6 Point of unity power factor

Referring to the phasor diagrams in figures 3.5 and 3.6, with the right combination of back EMF and synchronous impedance, it is possible to have a resultant leading power factor. The unity power factor threshold is a line of gradient  $-\frac{X_S}{R}$  through the apex of  $\vec{V}$ , as illustrated in figure 3.7. If  $\vec{IZ}_S$  lies along this *unity power factor* line,  $\vec{IR}$  is vertical, resulting in a power factor of unity. To achieve this, a back EMF sufficiently high enough is required such that this line intersects the  $E_0$  locus. Operation beyond (to the right of) this line would result in a leading power factor.

For a machine with a given synchronous impedance, the power factor can thus be controlled via the field excitation [21]. Whilst on load, the power factor can be changed from lagging to leading by increasing the field excitation, inducing a larger back EMF ( $E_0$ ). In fig. 3.7, both machines are at full-load. By increasing the field

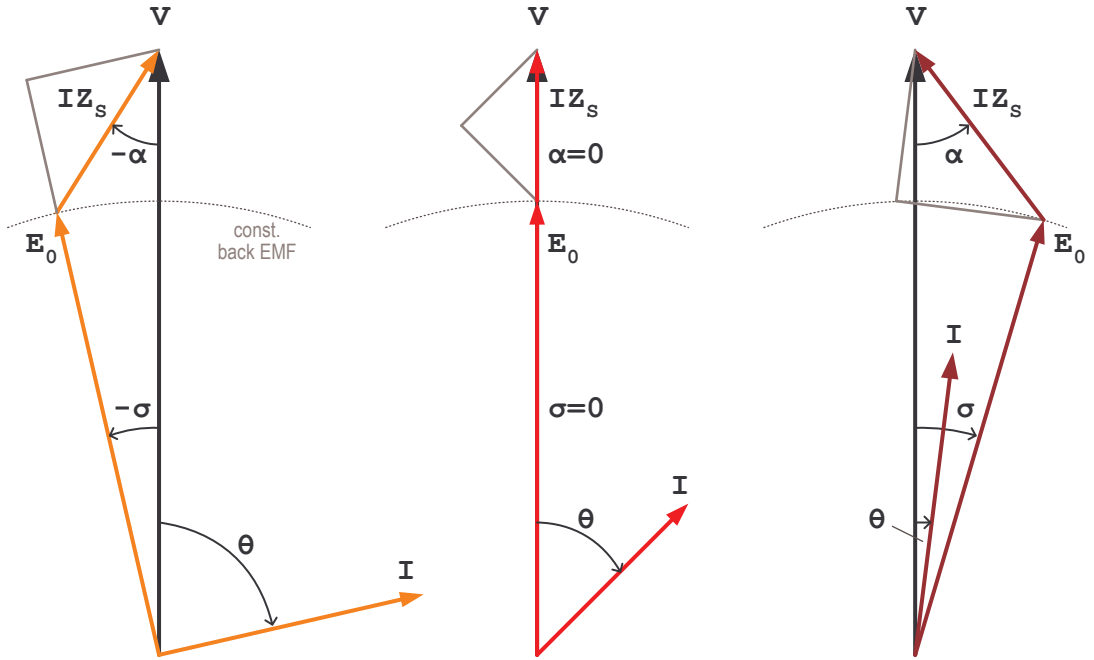


Figure 3.8: Phasor diagrams of distinguishing points corresponding to: no-load (orange), minimum current (red), and heavy load (brown).

excitation from a back EMF of  $E_{01}$  to  $E_{02}$ , the power factor switches from lagging to leading. For the same reasons, large synchronous turbo generators can function as on-line condensers.

### 3.1.7 Distinguishing points of operation

To summarise, three characteristic regions are clear in the motoring operation of synchronous machines. From no-load, as the load increases, a leading RRA ( $\sigma < 0$ ) reduces towards zero, the stator current decreases slightly, and the power factor improves. At some load when  $\sigma = 0$  (when  $\vec{E}_0$  aligns with  $\vec{V}$ ), a current minimum is reached and a power factor of  $pf = \cos(\angle Z_S)$  results. As the machine is loaded further, a lagging RRA ( $\sigma > 0$ ) increases, the current rises, and the power factor continues to improve. If the locus of  $E_0$  intersects the impedance slope, a point of unity power factor will be reached, and beyond this the power factor is leading.

By introducing a new angle  $\alpha$  between  $\vec{V}$  and  $I\vec{Z}_S$  the trigonometry of the phasor diagrams is greatly simplified. Figure 3.8 shows the relationship between  $\alpha$  and  $\sigma$  for the three regions described. Since  $\alpha$  and  $\sigma$  are both interior angles of triangle

$V - \hat{O} - E_0$ , they sum to  $180^\circ$ .

At no-load,  $-\alpha$  is such that  $\vec{E}_0$  is exactly inline with  $\vec{IX}_S$  and perpendicular to  $\vec{IR}$ . At minimum current,  $\alpha = 0$  such that  $\vec{E}_0$  is inline with  $\vec{V}$ . For unity power factor,  $\alpha = \angle Z_S$  such that  $\vec{IZ}_S$  lies along the unity power factor line, making  $\vec{IR}$  vertical.

## 3.2 Modelling Equations

As described earlier, the prototype machine comprises two stages coupled together. The unequal load-sharing implies that either the stages are unidentical (electrically and or magnetically), or some imbalance has arisen from their coupling together. It is anticipated that the difference between the two stages can be determined by examining their individual powers.

The electrical power drawn per phase by each stage is given by:

$$P = VI \cos \theta$$

The power supplied depends on the load being driven and can be expressed at any specific load in terms of the current drawn by  $I|_{load}$  and the associated power factor by  $pf|_{load}$ . By determining the relationships between the current versus load and power factor versus load, the power versus load relationship can be found, as per 3.2. Because the amount of *load* is difficult to measure and not explicitly required, another variable is chosen to quantify the loading, namely the RRA  $\sigma$ .

$$\begin{aligned} P|_{load} &= V (I|_{load}) (pf|_{load}) \\ P(\sigma) &= V I(\sigma) pf(\sigma) \end{aligned} \quad (3.2)$$

Once the equivalent circuit parameters of the prototype machine have been evaluated, the two characteristic relationships described can be plotted for each stage of the motor. However, further insight into these two relationships is required.

In order to plot current versus RRA, the relationship between  $I$  and  $\sigma$  must be derived. Likewise, to plot the power factor versus RRA,  $\cos \theta$  in terms of  $\sigma$  is needed. And, to plot the current versus power factor, the relationship between  $I$  and  $\cos \theta$  is required.

$$\theta = \angle Z_S - \alpha \quad (3.3)$$

From 3.3,  $\theta$  can be determined from  $\alpha$ ; an interior angle of the triangle shown in figure 3.9.

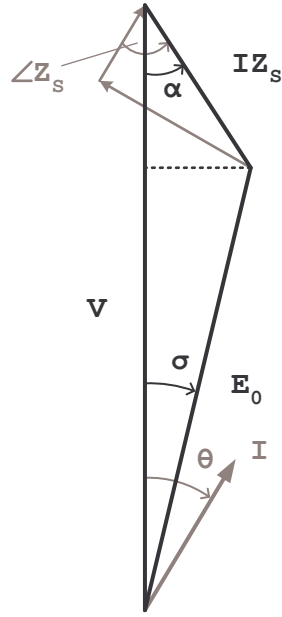


Figure 3.9: Cosine rule triangle used to determine the current versus RRA  $\sigma$  relationship.

### 3.2.1 Current and RRA relationship

The phasor diagram of operation is in essence the triangle<sup>2</sup> shown in fig. 3.9. By the cosine rule:

$$(IZ_S)^2 = E_0^2 + V^2 - 2E_0V \cos \sigma$$

$$I^2 = \frac{E_0^2 + V^2 - 2E_0V \cos \sigma}{Z_S^2}$$

Assuming  $E_0$  and  $V$  remain constant, the equation is of the form  $1 - \cos \sigma$ , which for a limited range of  $\sigma$  (say  $-\frac{\pi}{4} \leq \sigma \leq \frac{\pi}{4}$ ) looks like a positive parabola with a minimum of 1, symmetrical about the  $I$ -axis.

For motoring operation, only the positive solution is considered and hence the current is given by:

$$I(\sigma) = \frac{\sqrt{E_0^2 + V^2 - 2E_0V \cos \sigma}}{Z_S} \quad (3.4)$$

<sup>2</sup>Each side of the dark triangle corresponds to the respective vectors in fig. 3.2.

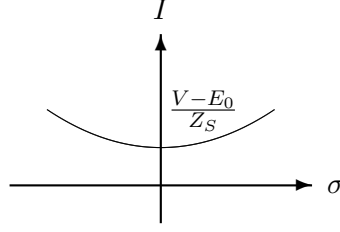


Figure 3.10: General form of current versus RRA  $\sigma$  relationship.

Substituting the double angle formula  $\cos \sigma = 1 - 2 \sin^2\left(\frac{\sigma}{2}\right)$  into 3.4:

$$\begin{aligned}
 I &= \frac{\sqrt{E_0^2 + V^2 - 2E_0V \left[1 - 2 \sin^2\left(\frac{\sigma}{2}\right)\right]}}{Z_S} \\
 &= \frac{E_0^2 + V^2 - 2E_0V + 4E_0V \sin^2\left(\frac{\sigma}{2}\right)}{Z_S}
 \end{aligned}$$

For  $\sigma$  small,  $\sin \sigma \approx \sigma$  and hence:

$$\begin{aligned}
 I &\approx \frac{\sqrt{E_0^2 + V^2 - 2E_0V + 4E_0V \left(\frac{\sigma}{2}\right)^2}}{Z_S} \\
 &\approx \frac{\sqrt{(V - E_0)^2 + E_0V \sigma^2}}{Z_S} \tag{3.5}
 \end{aligned}$$

which is parabolic as expected, symmetrical about the positive  $I$ -axis, and takes on the form as illustrated in figure 3.10. The magnitude of the current is the voltdrop across  $I\vec{Z}_S$  and is dependent on the magnitude of the supply voltage, back EMF and synchronous impedance.

$$|I_{min}| = \frac{V - E_0}{Z_S}$$

From 3.5, minimum current results when  $\sigma = 0$ . As shown in fig. 3.8, at this position,  $\vec{E}_0$  and  $\vec{V}$  are inline resulting in a minimum voltdrop across  $I\vec{Z}_S$ . When  $\sigma$  is leading or lagging, the current is larger.

Comparing figures 3.11 and 3.12 it is seen that, owing to the larger  $|Z_S|$ , the current drawn is less for the same rotor reference angles.

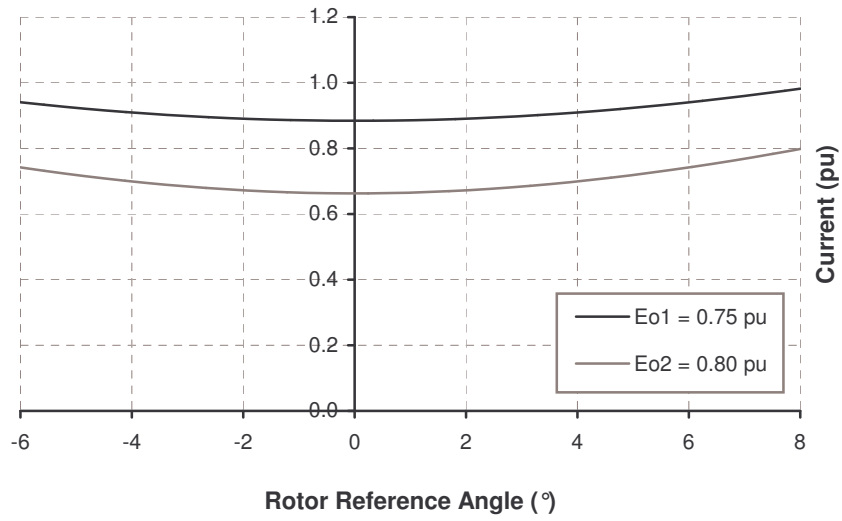


Figure 3.11: Current versus RRA  $\sigma$  for two machines having back EMFs of 0.75 pu and 0.80 pu, both with  $R : X_S = 1 : 1$ .

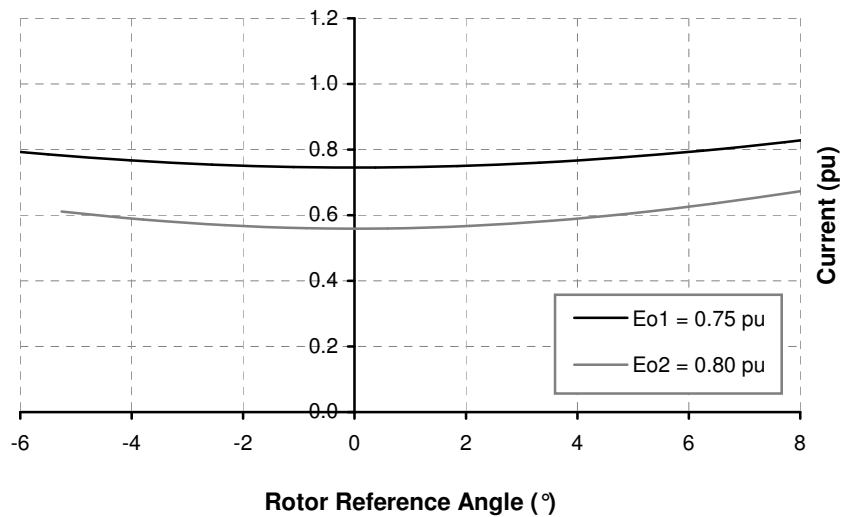


Figure 3.12: Current versus RRA  $\sigma$  for two machines having back EMFs of 0.75 pu and 0.80 pu, both with  $R : X_S = 1 : 2$ .

### 3.2.2 Power Factor and RRA relationship

Referring to fig. 3.9, the power factor is given by:

$$pf = \cos \theta = \cos(\angle Z_S - \alpha) \quad (3.6)$$

Expanding,  $\angle Z_S$  remains fixed and  $\alpha$  is related to  $\sigma$  by:

$$\begin{aligned} \tan \alpha &= \frac{E_0 \sin \sigma}{V - E_0 \cos \sigma} \\ \therefore \alpha &= \arctan\left(\frac{E_0 \sin \sigma}{V - E_0 \cos \sigma}\right) \end{aligned} \quad (3.7)$$

Hence the power factor is given by:

$$pf(\sigma) = \cos \left[ \angle Z_S - \arctan\left(\frac{E_0 \sin \sigma}{V - E_0 \cos \sigma}\right) \right] \quad (3.8)$$

Substituting the double angle formula  $\cos \sigma = 1 - 2 \sin^2\left(\frac{\sigma}{2}\right)$  into 3.7:

$$\begin{aligned} \alpha &= \arctan \left[ \frac{E_0 \sin \sigma}{V - E_0 \left(1 - 2 \sin^2 \frac{\sigma}{2}\right)} \right] \\ &= \arctan \left[ \frac{E_0 \sin \sigma}{V - E_0 + 2E_0 \sin^2 \frac{\sigma}{2}} \right] \end{aligned}$$

and for  $\sigma$  small,

$$\begin{aligned} \alpha &\approx \arctan \left[ \frac{E_0 \sigma}{V - E_0 + 2E_0 \left(\frac{\sigma}{2}\right)^2} \right] \\ &= \arctan \left[ \frac{E_0 \sigma}{V - E_0 \left(1 - \frac{\sigma^2}{2}\right)} \right] \end{aligned}$$

Assuming that  $\sigma \ll 1$  and therefore  $\left(1 - \frac{\sigma^2}{2}\right) \approx 1$  :

$$\begin{aligned} \alpha &\approx \arctan\left(\frac{E_0 \sigma}{V - E_0}\right) \\ pf &\approx \cos \left[ \angle Z_S - \arctan\left(\frac{E_0 \sigma}{V - E_0}\right) \right] \end{aligned} \quad (3.9)$$

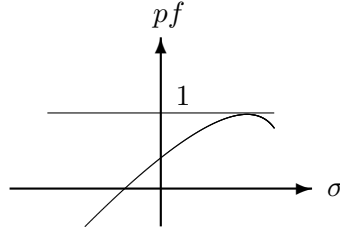


Figure 3.13: General form of power factor versus RRA  $\sigma$  relationship.

The *cos* and *arctan* functions can be expressed in terms of their Taylor series which yields an approximate relationship between *pf* and  $\sigma$  from 3.9.

In terms of the Taylor series,

$$\alpha = \arctan(x) \approx x - \frac{x^3}{3} + \frac{x^5}{5} - \dots$$

$$\text{where : } x = \frac{E_0 \sigma}{V - E_0}$$

Similarly,

$$\cos \theta \approx 1 - \frac{\theta^2}{2} + \frac{\theta^4}{24} - \dots$$

$$\text{where : } \theta = \angle Z_S - \alpha$$

The resultant 4<sup>th</sup> order polynomial for the *pf* is therefore given by:

$$pf \approx 1 - \frac{\left(\angle Z_S - \frac{E_0 \sigma}{V - E_0}\right)^2}{2} + \frac{\left(\angle Z_S - \frac{E_0 \sigma}{V - E_0}\right)^4}{24} - \dots$$

Clearly, the 2<sup>nd</sup> order term dominates that of the 4<sup>th</sup> order one and hence the power factor can be approximated by 3.10; a parabolic curve with a maximum, as illustrated in figure 3.13.

$$pf \approx 1 - \frac{\left(\angle Z_S - \frac{E_0 \sigma}{V - E_0}\right)^2}{2} \quad (3.10)$$

From 3.10, the maximum power factor obtainable is unity when the terms enclosed within brackets sum to zero. However, the corresponding  $\sigma$  required to achieve this may be out of the range of interest. To determine  $\sigma$  that yields unity power factor, the first derivative is taken, equated to zero and solved:

$$\frac{d\text{pf}}{d\sigma} = -\left(\angle Z_S - \frac{E_0 \sigma}{V - E_0}\right) \frac{E_0}{V - E_0}$$

$$\sigma|_{\text{unity pf}} = \left(\frac{V - E_0}{E_0}\right) \angle Z_S$$

This shows that for an under-excited machine, unity power factor will only be reached for a lagging RRA.

From 3.6 the power factor at which minimum current occurs, when  $\sigma = 0$  (implying  $\alpha = 0$ ) is given by:

$$\text{pf}|_o = \cos(\angle Z_S - \alpha)$$

$$\text{pf}|_o = \cos(\angle Z_S)$$

$$\text{pf}|_o \approx 1 - \frac{(\angle Z_S)^2}{2}$$

From figures 3.14 and 3.15, the power factors at  $\sigma = 0$  differ for the two machines; although the back EMF itself has little influence, the impedance ratio (hence  $\angle Z_S$ ) plays a significant role.

The equations above are derived from the electrical phasor diagrams only and thus have no dependence on the direction of rotation of the machine. This implies that the machine should work equally well in either direction - as one would expect.

### 3.2.3 Current and Power Factor relationship

The drawback of using  $\sigma$  to relate the loading is that it requires an intrusive mechanical measurement to obtain the relative rotor position. Since the power factor is approximately proportional to load, the current can be plotted against the power factor from simple measurements. If  $Z_S$  and  $E_0$  remain constant, since  $\theta$  is proportional to  $\sigma$ , the corresponding RRAs can be determined from the power factor measurements by 3.11. Therefore, from this single graph, a plot of power versus load can be derived using a simple measurement technique.

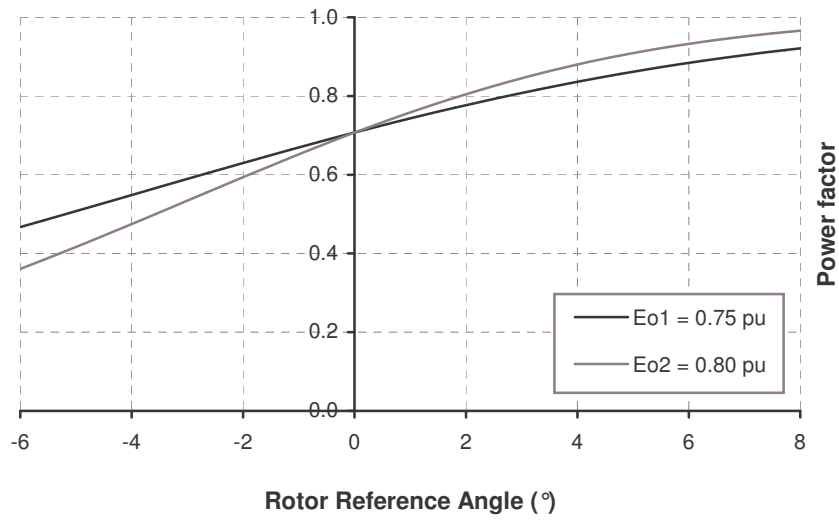


Figure 3.14: Power factor versus RRA  $\sigma$  for two machines having back EMFs of 0.75 pu and 0.80 pu, both with  $R : X_S = 1 : 1$ .

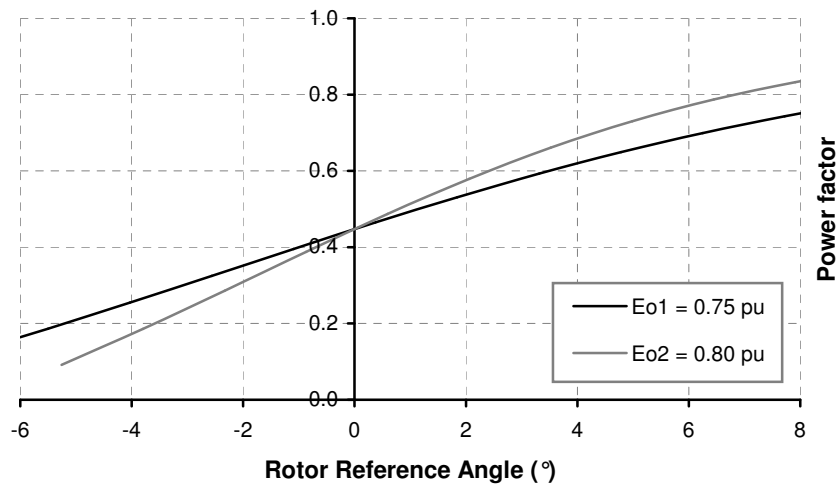


Figure 3.15: Power factor versus RRA  $\sigma$  for two machines having back EMFs of 0.75 pu and 0.80 pu, both with  $R : X_S = 1 : 2$ .

From fig. 3.9, using the sine rule:

$$\frac{IZ_S}{\sin \sigma} = \frac{E_0}{\sin \alpha}$$

$$\sigma = \arcsin\left(\frac{IZ_S \sin \alpha}{E_0}\right)$$

$$\text{where : } \alpha = \angle Z_S - \theta$$

Although  $\alpha$  may swing between  $\pm\frac{\pi}{4}$ ,  $\sigma$  is typically small:

$$\therefore \sigma \approx \frac{IZ_S \sin \alpha}{E_0} \quad (3.11)$$

In essence, the current versus power factor relationship is the current versus RRA plotted against the power factor versus RRA (i.e. equation 3.4 against 3.8) and is independent of the RRA.

From fig. 3.9, using the cosine rule:

$$E_0^2 = V^2 + I^2 Z_S^2 - 2V I Z_S \cos \alpha$$

$$\text{where : } \alpha = \angle Z_S - \theta$$

$$I = \frac{V \cos \alpha \pm \sqrt{E_0^2 - V^2 \sin^2 \alpha}}{Z_S} \quad (3.12)$$

The *sin* and *cos* functions can be expressed in terms of their Taylor series which yields an approximate expression of  $I$  in terms of  $\alpha$ .

$$\sin \alpha \approx \alpha - \frac{\alpha^3}{6} + \dots$$

$$\therefore \sin^2 \alpha \approx \alpha^2 - \frac{\alpha^4}{3} + \frac{\alpha^6}{36} \dots$$

Substituting the double angle formula  $\cos \alpha = 1 - \sin^2\left(\frac{\alpha}{2}\right)$ :

$$\cos \alpha = 1 - \frac{\alpha^2}{2} + \frac{\alpha^4}{6} - \frac{\alpha^6}{72} + \dots$$

For  $\alpha \leq 1$  radian, limiting the above polynomial to the  $2^{nd}$  order provides a reasonably good approximation. Substituting into 3.12 gives:

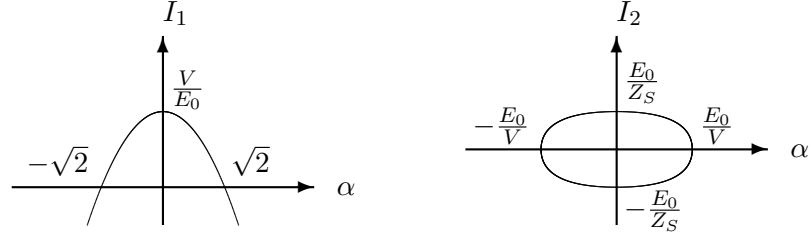


Figure 3.16: Components of current versus RRA  $\sigma$ : (a) parabola, (b) ellipse.

$$I \approx \frac{V\left(1 - \frac{\alpha^2}{2}\right) \pm \sqrt{E_0^2 - V^2 \alpha^2}}{Z_S} \quad (3.13)$$

To illustrate the general form of 3.13, the function is split into its two components:

$$I_1 = \frac{V}{Z_S} \left(1 - \frac{\alpha^2}{2}\right)$$

$$I_2 = \pm \frac{1}{Z_S} \sqrt{E_0^2 - V^2 \alpha^2}$$

$$\text{where : } I = I_1 + I_2$$

The first component can be re-written as:

$$I_1 = -\frac{V}{Z_S} \left(\frac{\alpha^2}{2} + 1\right)$$

which is a parabola with a maximum, as illustrated in figure 3.16(a).

The second component can be re-written as:

$$I_2 = \pm \frac{\sqrt{E_0^2 - V^2 \alpha^2}}{Z_S}$$

$$\left(\frac{Z_S^2}{E_0^2}\right) I_2^2 + \left(\frac{V^2}{E_0^2}\right) \alpha^2 = 1$$

which is an ellipse centred about the origin as illustrated in figure 3.16(b).

To illustrate 3.13, the two graphs are added together to produce figure 3.17. At  $\alpha = 0$ , the centre of the ellipse is shifted up to the parabola's maximum. As  $\alpha \rightarrow \pm 1$ , the concave bottom-half of the ellipse is flattened by the convex parabola, whilst the convex top-half of the ellipse is exaggerated; resulting in an oval shape.

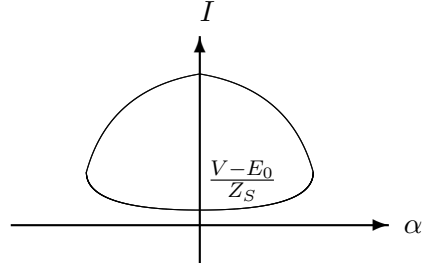


Figure 3.17: Resultant oval-shaped ellipse representing the current versus  $\alpha$  function.

The two solutions of 3.13 are the top-half and bottom-half of the resultant ellipse, corresponding to the sign of  $I_2$  respectively.

Finally, to illustrate the general form of the current versus power factor relationship, the curve is transformed from a horizontal axis of  $\alpha$  to one of  $pf$ . These two variables are related to one another by:

$$\begin{aligned}\alpha &= \angle Z_S - \theta & (3.14) \\ \alpha &= \angle Z_S - \arccos(\cos \theta) \\ \alpha &= \angle Z_S - \arccos(pf)\end{aligned}$$

The  $\arccos$  function can be expressed in terms of its Taylor series,

$$\arccos(pf) = \frac{\pi}{2} - pf - \frac{pf^3}{6} - \dots$$

but it only converges for  $pf \ll 1$  and hence is sufficient for when  $0 \leq pf \leq 0.5$ , giving:

$$\begin{aligned}\alpha &\approx \angle Z_S - \left(\frac{\pi}{2} - pf\right) \\ \therefore pf &\approx \alpha - \angle Z_S + \frac{\pi}{2}\end{aligned}$$

For  $pf \approx 1$ , 3.14 can be written as:

$$\alpha = \angle Z_S - \arcsin(\sin \theta)$$

The trigonometric identity  $\sin^2 \theta + \cos^2 \theta = 1$  can be used to find  $\sin \theta$ , given by:

$$\begin{aligned}\sin \theta &= \sqrt{1 - \cos^2 \theta} \\ \sin \theta &= \sqrt{1 - pf^2}\end{aligned}$$

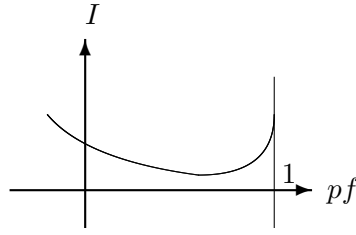


Figure 3.18: General form of current versus power factor relationship.

Expressing the *arcsin* function in terms of its Taylor series,

$$\arcsin(x) = x + \frac{x^3}{6} + \dots$$

where  $x = \sin \theta$  and will converge for  $pf \approx 1$ . Hence,

$$\alpha \approx \angle Z_S - \left( \sqrt{1 - pf^2} \right)$$

$$\therefore pf \approx \sqrt{1 - (\angle Z_S - \alpha)}$$

which gives good correlation when  $0.8 \leq pf \leq 1$ . As expected, unity power factor is achieved when  $\alpha = \angle Z_S$ . For power factors outside the range of the two approximations presented, a linear interpolation between both functions would probably suffice.

For small values of  $pf$ , the relationship to  $\alpha$  is linear, resulting in fig. 3.17 being shifted along the positive  $pf$ -axis. For large values of power factor the relationship is quadratic, resulting in the points ( $pf \approx 1$ ) being compressed together. Since the smaller solution of 3.12 is the one of interest, the general form of the current versus power factor relationship is illustrated in figure 3.18.

There are two interesting characteristics to note with this relationship. Firstly, the current minimum is clear but the corresponding power factor is not as evident. To accurately determine the minimum current and corresponding power factor,  $\sigma = 0$  would be substituted into the appropriate equations derived. Secondly, a vertical asymptote exists at unity power factor such that as the power factor improves towards unity, the current drawn rises rapidly. With reference to fig. 3.13, if unity power factor is reached and the machine is further loaded, the power factor begins to lead and decrease again. Consequently, the current continues to rise rapidly and the resulting plot would curve back on itself, scribing the top-half of the ellipse depicted fig. 3.17.

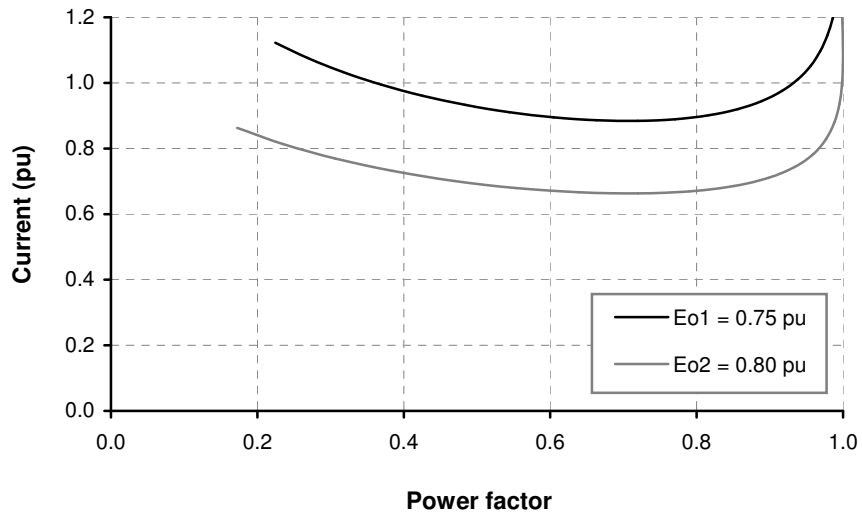


Figure 3.19: Current versus RRA  $\sigma$  relationship for two machines having back EMFs of 0.75 pu and 0.80 pu, both with  $R : X_S = 1 : 1$ .

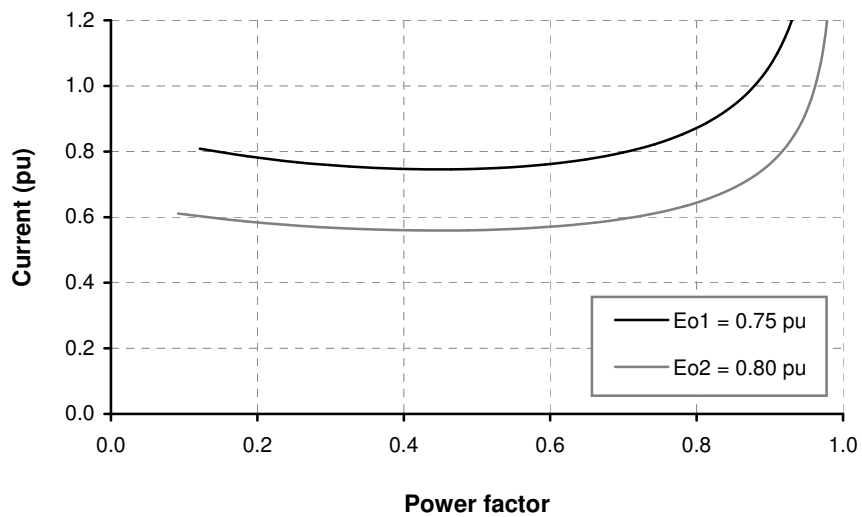


Figure 3.20: Current versus RRA  $\sigma$  relationship for two machines having back EMFs of 0.75 pu and 0.80 pu, both with  $R : X_S = 1 : 2$ .

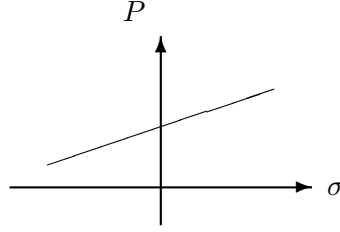


Figure 3.21: General form of power versus RRA  $\sigma$  relationship.

From figures 3.19 and 3.20, the graphs clearly illustrate the current minima and rapid current rise towards unity power factor. Note that the power factor at minimum current is the same power factor at  $\sigma = 0$  from the previous pair of graphs.

### 3.2.4 Power and RRA relationship

From 3.15, with the two load-dependent functions derived, the relationship between the power and RRA can be illustrated. From fig. 2.12, a linear relationship between the power drawn and the load driven is anticipated.

$$P(\sigma) = V I(\sigma) pf(\sigma) \quad (3.15)$$

Substituting equations 3.4 and 3.8 for  $I(\sigma)$  and  $pf(\sigma)$  respectively would give an explicit relationship of the power versus RRA  $\sigma$ .

For illustration purposes with  $V$  remaining constant, substituting the approximate functions 3.5 and 3.10 derived and considering for  $\sigma$  small gives:

$$P \approx \left[ \frac{V E_0 \angle Z_S}{Z_S} \right] \sigma + \left[ V \frac{(V - E_0)}{Z_S} \left( 1 - \frac{\angle Z_S^2}{2} \right) \right] \quad (3.16)$$

which is a straight line as per figure 3.21. From figures 3.22 and 3.23, since the Back EMF has influenced the previous relationships derived, it is not surprising that its effects are again clearly evident.

The  $P$ -intercept, when  $\sigma = 0$ , is the power given by:

$$P = V \left( \frac{V - E_0}{Z_S} \right) \left( 1 - \frac{\angle Z_S^2}{2} \right)$$

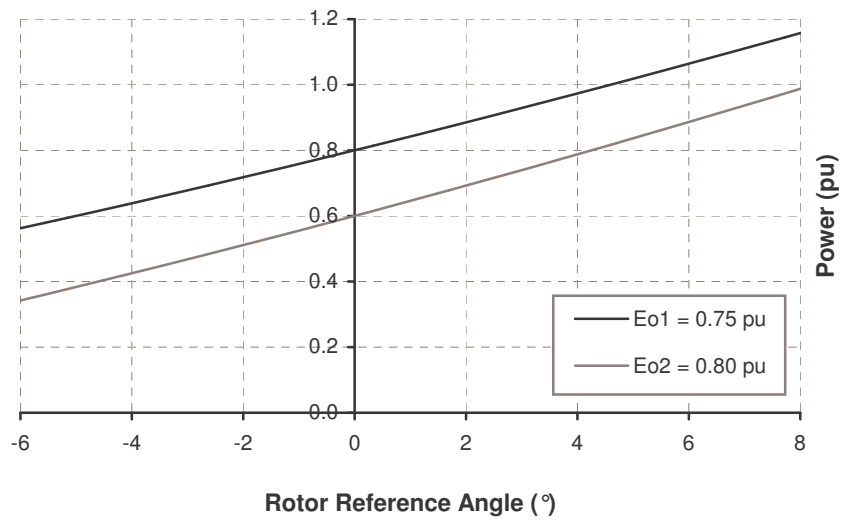


Figure 3.22: Power versus RRA  $\sigma$  relationship for two machines having back EMFs of 0.75 pu and 0.80 pu, both with  $R : X_S = 1 : 1$ .

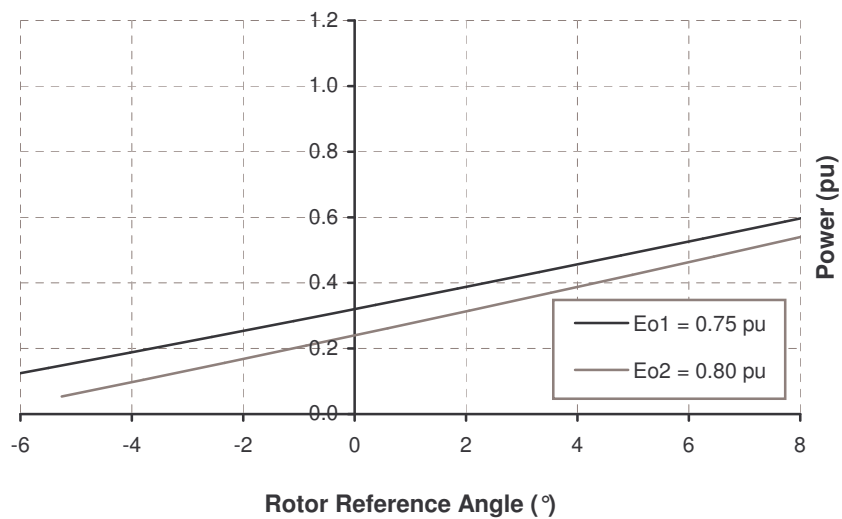


Figure 3.23: Power versus RRA  $\sigma$  relationship for two machines having back EMFs of 0.75 pu and 0.80 pu, both with  $R : X_S = 1 : 2$ .

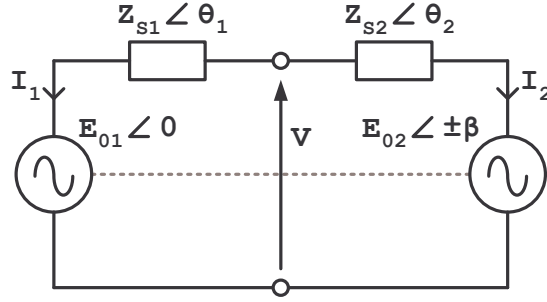


Figure 3.24: Equivalent circuit of double-stage machine with parallel stages.

At this point  $\vec{E}_0$  and  $\vec{V}$  are inline and hence, as before:

$$\left( \frac{V - E_0}{Z_S} \right) = I$$

$$\left( 1 - \frac{\angle Z_S^2}{2} \right) \approx \cos \angle Z_S$$

$$\therefore P = VI \cos \angle Z_S$$

With the individual stage models now complete, the machine model is expanded to include the multiple coupling of individual stages.

### 3.3 Model Expansion for Multi-stage Machines

A multi-stage machine is one comprising several stages coupled together via a common shaft. In the ideal case, each stage would be:

- supplied with the same voltage,
- have equal stator winding impedances,
- have equal back EMFs.

Assuming a constant flux through the machine (refer to fig. 2.8), the stator windings of each stage would link with a common flux, resulting in equal back EMFs being induced. This assumes that the leakage reactances of each stage would also be the same, which implies equal airgaps. All the windings would then be connected in parallel. With aligned rotor poles, the common flux would result in equal back EMFs, in phase with one another.

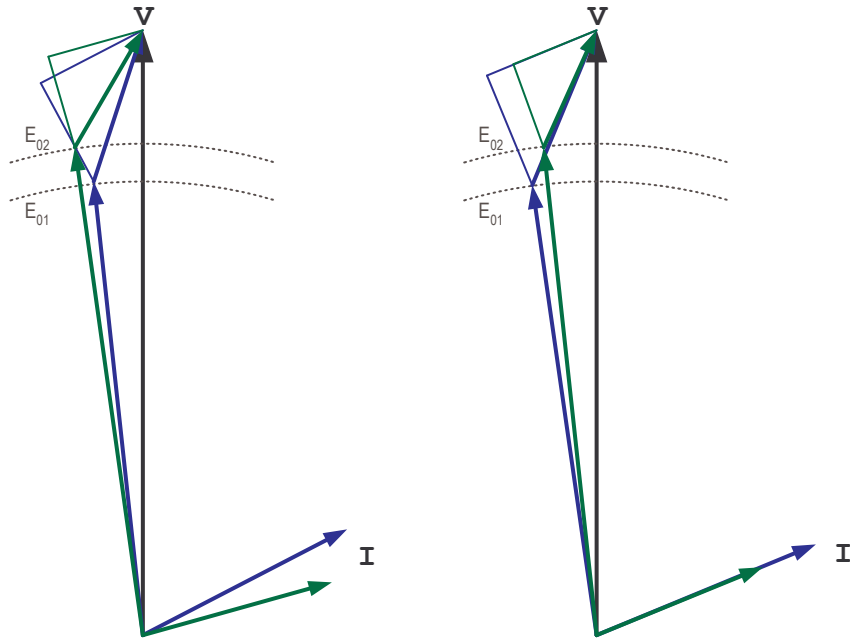


Figure 3.25: Multi-stage phasor diagrams for motoring in the CW and CCW directions respectively.

However, if the prototype machine was ideal, this research would not be necessary; by stacking the additional stator and rotor sections onto the common shaft, the electric or magnetic coupling has somehow become unbalanced. Thus, the multistage model needs to account for the idealities listed above. Assuming that the prototype machine is anything but ideal, the model developed assumes that the winding impedances are different, and that the back EMFs are unequal (due to differing airgaps) and slightly out of phase (due to misaligned rotor disks or stator cores).

To achieve an overall model for the prototype machine, the two respective models for each stage are combined. Since both stages share common flux paths (albeit with possible differing fluxes), the respective models are linked together by the relative position of their back EMFs. This is due to the rotors of each stage being fixed to the common shaft, where any mechanical misalignment between the rotors and hence back EMFs remains constant under all conditions.

In coupling the two stages together, both stage windings are parallel-connected and supplied with voltage  $V$ , but have independent synchronous impedances  $Z_{S1}$  and  $Z_{S2}$ . The back EMFs  $E_{01}$  and  $E_{02}$  are unequal and slightly misaligned by  $\beta$ , as illustrated in the equivalent circuit of figure 3.24. The misalignment could be due either to misaligned rotors (assuming stators are inline), misaligned stators (assuming rotors are inline), or a combination of both.

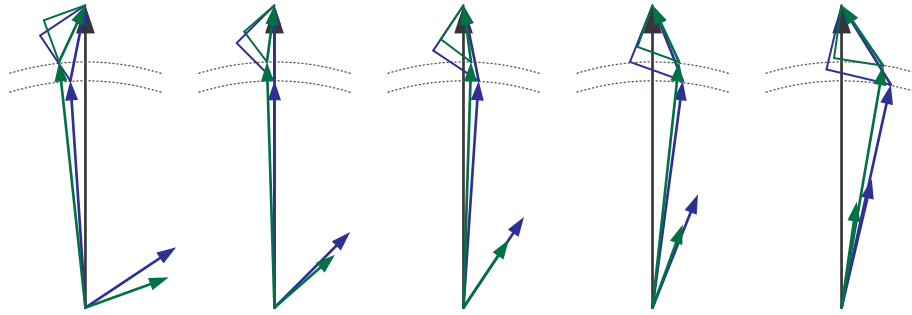


Figure 3.26: Animated phasor diagrams for motoring in the CW direction with *Stage2* (green) leading *Stage1* (blue), from no-load to full-load.

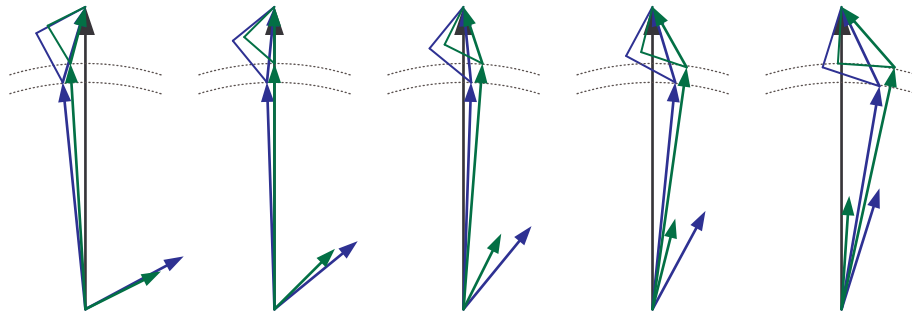


Figure 3.27: Animated phasor diagrams for motoring in the CCW direction with *Stage2* (green) lagging *Stage1* (blue), from no-load to full-load.

The corresponding phasor diagrams in figure 3.25 hint towards the possible source of the underlying problem. Since the back EMFs of each stage are misaligned, one back EMF vector leads or lags the other, dependent on the direction of rotation. To illustrate, if the rotor pole of *Stage1* (corresponding to  $E_{01}$ ) is mechanically misaligned by  $5^\circ$  with the pole of *Stage2* ( $E_{02}$ ), then when rotating in one direction,  $E_{01}$  will lead  $E_{02}$  by  $5^\circ$ , and whilst rotating in the opposite direction, will lag by  $5^\circ$ . The phasor diagrams of a multi-stage machine therefore become dependent on the direction of rotation.

Figures 3.26 and 3.27 clearly show the effect of the misalignment for clockwise and counter-clockwise rotation respectively. Of particular interest are the power factors resulting from the orientation of the  $Z_S$  triangles.

The adaption of the equations developed in the preceding sections for a multi-stage machine is straightforward. Using *Stage1* as a reference, in one direction *Stage2* leads by  $\beta$  and in the other direction *Stage2* lags by  $\beta$ . Therefore, to expand the

current versus RRA model defined by 3.4 for a multi-stage machine, the *Stage1* current would take on 3.4, whilst *Stage2* would have an angle of  $\beta$  included as an offset to  $\sigma$ , to give 3.17.

$$I(\sigma) = \frac{\sqrt{E_0^2 + V^2 - 2E_0V \cos(\sigma - \beta)}}{Z_S} \quad (3.17)$$

Since the current versus RRA model is now dependent on the direction of rotation, two plots are required to represent the model. Figures 3.28 and 3.29 result from introducing a misalignment into the demonstration machine, for comparison with fig. 3.11. In both figures, the reference *Stage1* retains its current minimum at  $\sigma = 0$ , as per fig. 3.11. Depending on the direction of rotation, the minimum of *Stage2* shifts either to the left or right of the  $I$ -axis.

Similarly, since the power factor versus RRA model defined by 3.8 is dependent on the RRA and hence misalignment, it is adapted to include this by:

$$pf(\sigma) = \cos\left(\angle Z_S - \arctan\left[\frac{E_0 \sin(\sigma - \beta)}{V - E_0 \cos(\sigma - \beta)}\right]\right) \quad (3.18)$$

Now also dependent on the direction of rotation, two plots are required to represent the power factor versus RRA model.

Figures 3.30 and 3.31 are presented for comparison with fig. 3.14. In both figures, *Stage1* cuts the  $\sigma = 0$  axis at the same point, as per figure 3.14. The difference in power factors at  $\sigma = 0$  due to the left and right shift of *Stage2*, is clearly shown. As a result, points of equal power factor are located on the left and right sides of the  $pf$ -axis respectively.

Because the current versus power factor model indirectly defined by 3.12 is independent of the RRA, the misalignment has no impact. Hence, plotting the current versus power factor relationship on the same set of axes allows for easy comparison of the individual stages, independent of any misalignment or direction of rotation. Figure 3.32 is obtained for both clockwise and counter-clockwise rotation and remains the same as fig. 3.19 on which it is based.

With the multi-stage relationships of current versus RRA and power factor versus RRA defined, the power versus RRA is determined from the product of the two functions together, and scaled by the constant supply voltage. This gives models for the power consumed by each stage of a multi-stage machine.

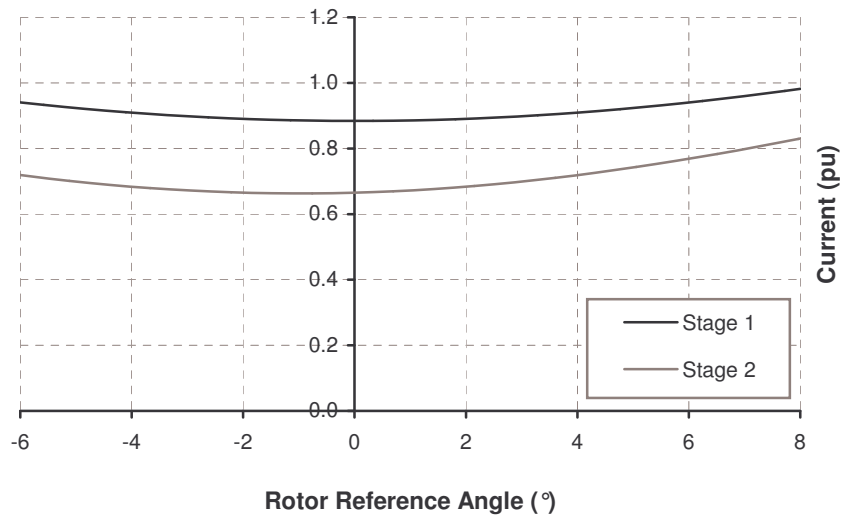


Figure 3.28: Current versus RRA  $\sigma$  for CW rotation. Note that the *Stage2* minimum leads that of *Stage1*.

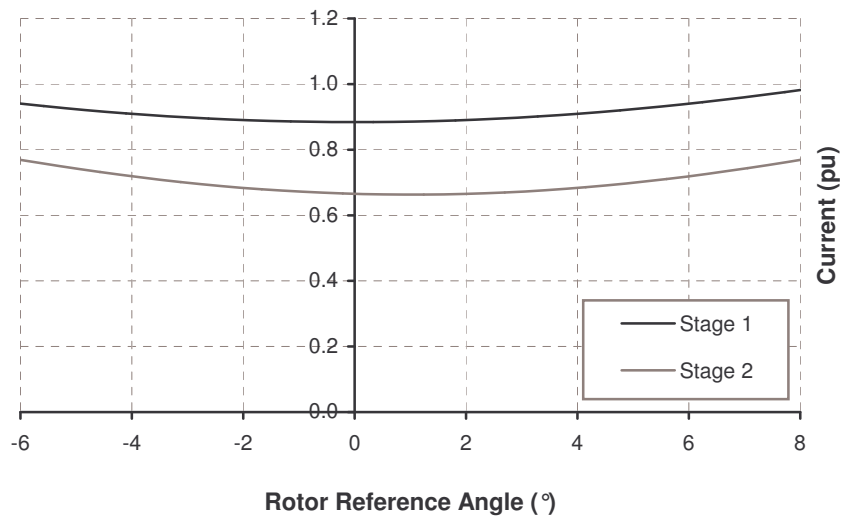


Figure 3.29: Current versus RRA  $\sigma$  for CCW rotation. Note that the *Stage2* minimum lags that of *Stage1*.

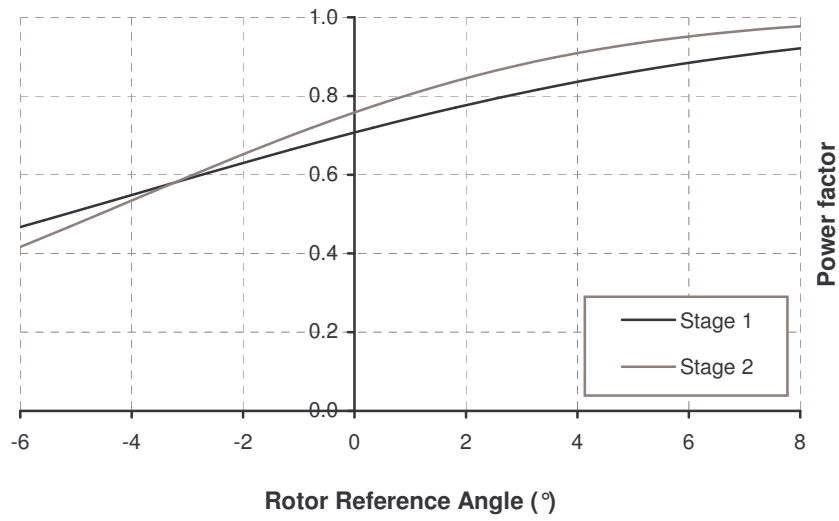


Figure 3.30: Power factor versus RRA  $\sigma$  for CW rotation. Note the equal  $pf$  point in the  $-\sigma$  quadrant.

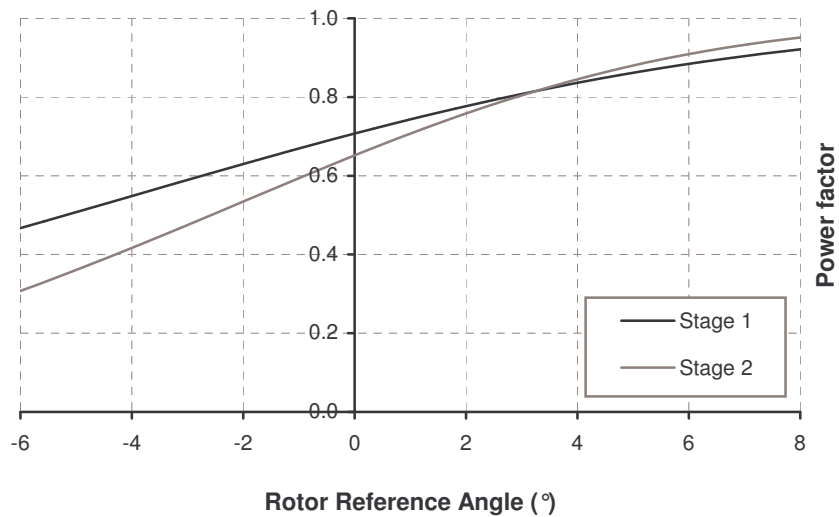


Figure 3.31: Power factor versus RRA  $\sigma$  for CCW rotation. Note the equal  $pf$  point in the  $+\sigma$  quadrant.

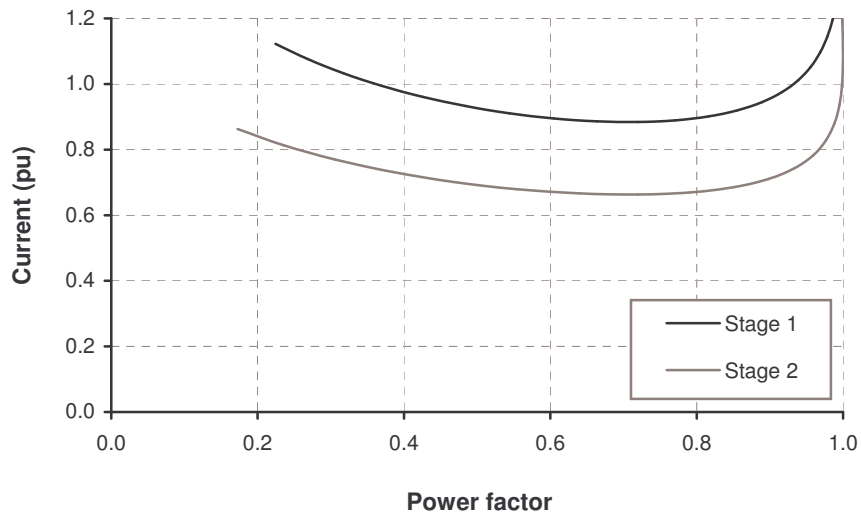


Figure 3.32: Current versus power factor; independent of any misalignment and direction of rotation.

By comparing figures 3.33 and 3.34, the unequal powers drawn is clearly due to the unequal Back EMFs and misalignment between the two stages. Consequently, the link between the unequal load-sharing and the direction of rotation is confirmed.

The following chapter presents methods to determine the various equivalent circuit parameters used in the models derived. From the completed models, graphs of the theoretical performance are plotted. These are then compared with actual measurements taken from the prototype for verification and refinement.

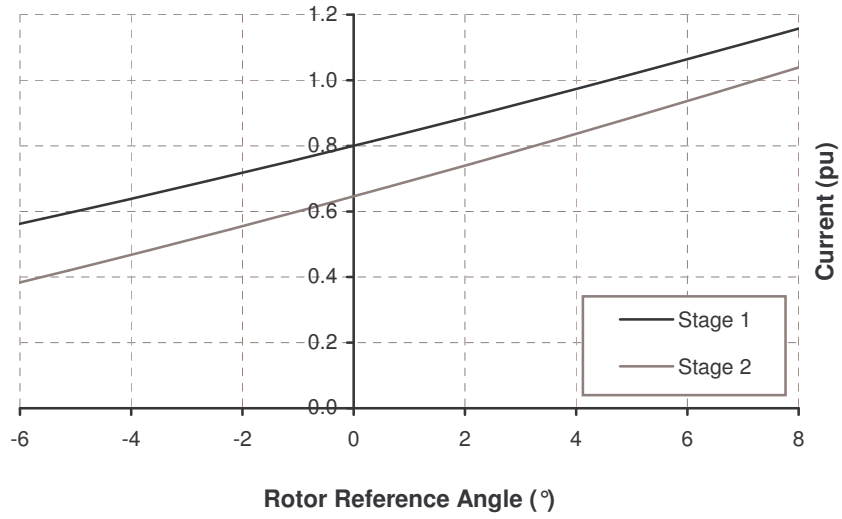


Figure 3.33: Power versus RRA  $\sigma$  for CW rotation from no-load to full-load.

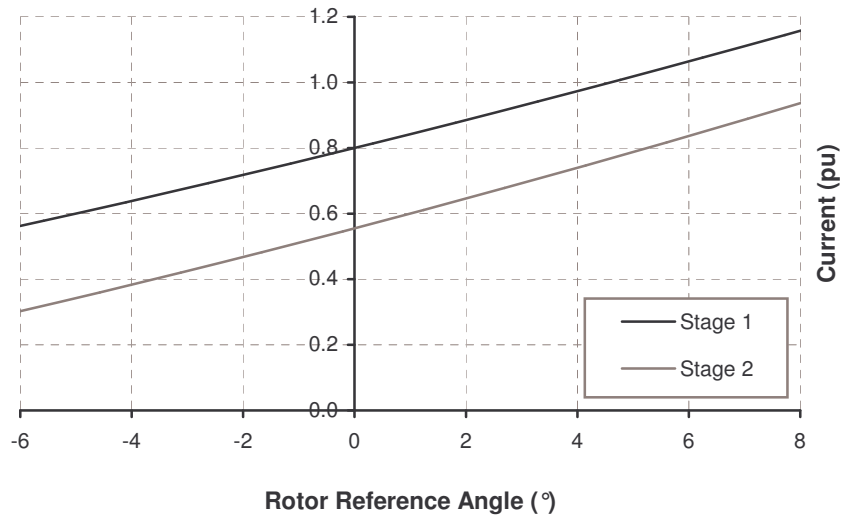


Figure 3.34: Power versus RRA  $\sigma$  for CCW rotation from no-load to full-load.

## Chapter 4

# Modelling of Prototype Machine

This chapter begins by determining the equivalent circuit parameters of the prototype machine using various methods and tests, each described in turn. The corresponding values are substituted into the characteristic equations derived in the preceding chapter, to complete the multi-stage models. Finally, the prototype models are presented and reviewed.

### 4.1 Quantization of Parameters

The equivalent circuit in fig. 3.1 comprises four fundamental components whose values have been assumed to remain constant. A closer look reveals that each component is very much dependent on the operating conditions. The winding resistance is a function of temperature and hence of the current drawn. The armature-reaction component of the synchronous reactance is a function of load whilst the leakage component is determined by the reluctance of the magnetic circuit. Since the back EMF induced by the permanent magnet field is temperature sensitive, any rise in operating temperature would temporarily demagnetize the magnets and retard the back EMF.

In trying to alleviate the inherent complexity of this 'simple' model, some constraints are imposed to reduce the inter-dependence of variables. It is assumed that, throughout the testing, the operating temperature has reached steady-state i.e. that the winding resistance and permanent magnet MMF remain constant.

Determining the equivalent circuit parameters from motor tests is somewhat difficult. In motoring operation, the individual stages are coupled by two components: the common supply voltage and the misalignment of their back EMFs. Furthermore,

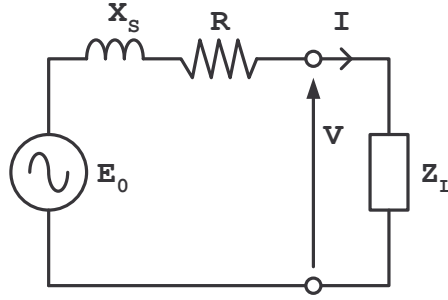


Figure 4.1: The steady-state per-phase equivalent circuit of a synchronous generator.

measurement of the back EMFs and load angle whilst in operation is unpractical. Although it is not impossible to derive the various equivalent circuit parameters from motoring tests, running the machine as a generator is far simpler.

#### 4.1.1 Generator operation

By operating the prototype machine as a generator with the parallel stator windings disconnected, the individual stages are electrically decoupled from one another. The equivalent circuit of each stage in turn can be determined from relatively simple tests, whilst the unused stages remain open-circuited. The details and serial numbers of all the instruments used for the respective tests are listed in table 3 of the appendix.

The steady-state per-phase equivalent circuit for a synchronous generator is given in figure 4.1. The winding resistance  $R$  is determined from straightforward measurement. The magnitude of the back EMF  $E_0$  is given by the open-circuit voltage when the electrical load is disconnected. The synchronous reactance  $X_S$  is determined from the KVL phasor sum around the circuit, with a known load  $Z_L$  connected.

From tests on each stage individually, both stages generate and deliver similar amounts of power as illustrated in figure 4.2, thus confirming that the source of the unequal load-sharing is inherent in the coupling of the two stages.

#### 4.1.2 Winding resistance

The stator of each stage of the prototype machine comprises a three-phase, star-connected winding. Due to a lack of foresight during the prototype's construction,

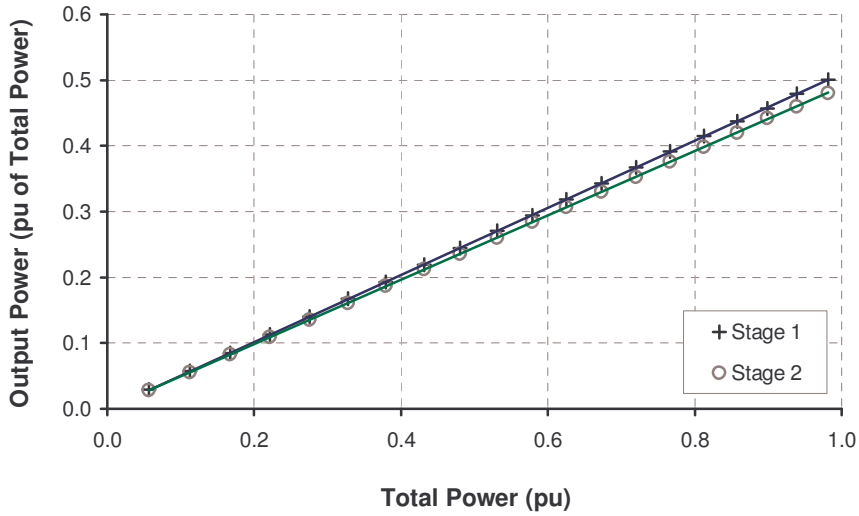


Figure 4.2: Power generated by each stage versus total rated power.

the neutral points were buried deep within the core, making them completely inaccessible. For each stage, resistive measurements were taken between adjacent lines and averaged.

Since the winding resistance is a function of temperature, the resistance measurements were taken once the steady-state operating temperature had been reached. This was achieved by running the machine at full-load until sufficiently warm and then performing the resistance measurement with a suitable Ohmic meter. This measurement is thus the winding resistance typical for continuous full-load operation; one of the assumptions behind the modelling equations.

From the procedure described, resistances of  $R_1 = R_2 = 0.97 \Omega$  were determined for the stator windings of each stage. The steady-state temperature reached is about  $65^\circ\text{C}$ .

### 4.1.3 Characterisation of back EMF

Until now, the back EMF presented has been assumed to remain constant. Since the field excitation in the prototype machine is provided by the permanent magnets mounted on the rotors, any change in the magnets' MMF will ultimately result in a corresponding change in the back EMFs induced. The MMF produced is a function of the magnet's temperature, described by its B-H curve, as per figure 4.3. An increase in temperature results in a temporary demagnetization of the magnet that weakens its MMF i.e. it appears as a form of *field weakening*. Since the reluctance of

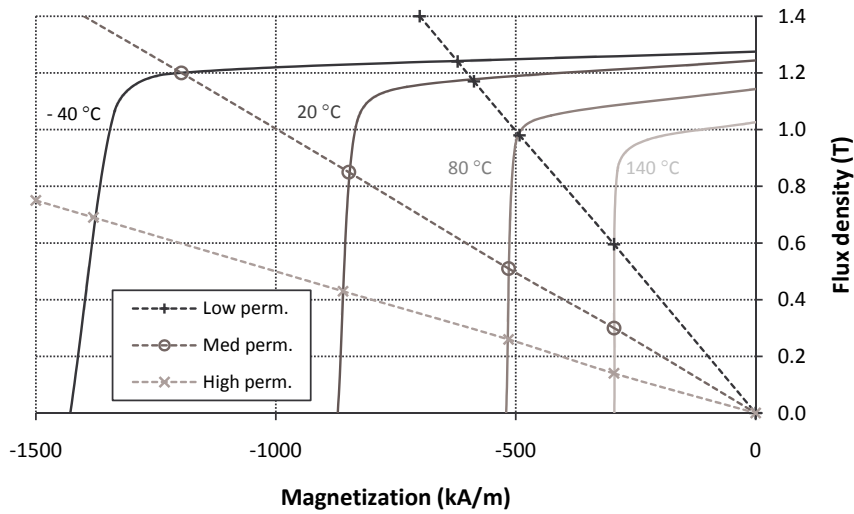


Figure 4.3: Magnet B-H temperature curves with different points of operation marked for comparison. Refer to figure 4.4.

the magnetic circuit remains the same, the resultant flux linkage across the airgap is proportionally reduced. Subsequently, the back EMF induced in the winding decreases with a rise in magnet temperature - a fundamental characteristic to the modelling of the machine.

A magnet temperature rise may result due to convective or conductive heating. In a permanent magnet machine, since the speed of operation is synchronous, the use of laminated steel in the rotor construction (onto which the magnets are mounted) is not generally necessary. Very often rotors are machined from steel billet, such as the prototype. The underlying reason is that due to the zero slip frequency, no eddy currents would be induced. In theory, assuming a generalised machine, the rotor would remain relatively cool with the only heating being due to possible convection across the airgap from the copper and iron losses of the stator.

In practice, stator harmonics due to the non-sinusoidal flux distribution in the airgap, result in eddy currents being induced in the rotor backiron. In a non-salient machine with wide parallel-sided slots such as the prototype, a zig-zag leakage flux may establish itself in the airgap, linking the stator teeth with the rotor magnets and backiron. The phenomenon intensifies towards the inner diameter where in the prototype, the slot width ( $5\text{ mm}$ ) is substantially wider than the tooth width ( $2\text{ mm}$ ), and where the spacing between adjacent magnets is narrowest ( $16\text{ mm}$ ). As the rotor turns, the zig-zag fluxes 'hop' from tooth to tooth, enjoying the low reluctance path, and generating substantial eddy current losses. Consequently, the resulting

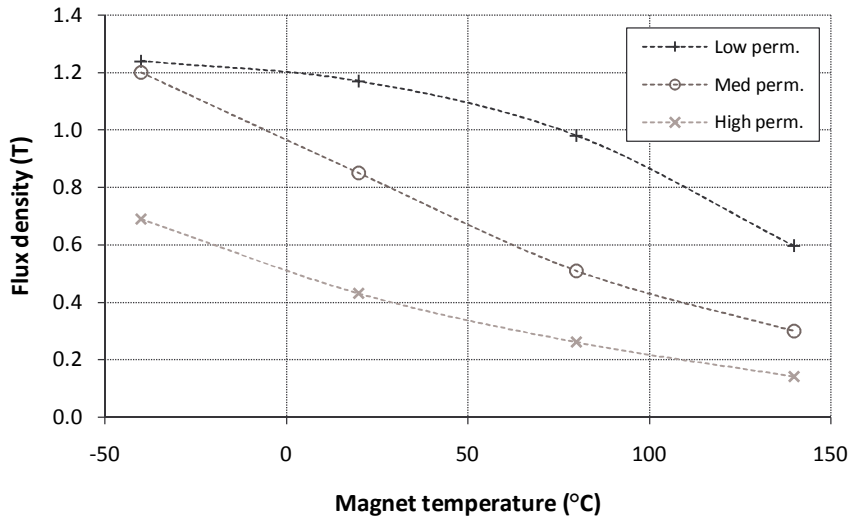


Figure 4.4: Temperature demagnetization profiles for the corresponding permeance lines.

significant temperature rise of the rotor backiron conducts heat directly into the magnets mounted flush against it.

Depending on the operating point on the B-H curve, a temperature rise may result in either a concave or convex relationship with the remnant flux density, and hence back EMF. Considering figure 4.4, when operating on the knee point (Med perm.), the influence is close to linear. When below (High perm.) or above (Low perm.) the knee, the response has either a negative or positive roll-off respectively. The design of permanent magnet machines requires special attention to this operating point. The prototype machine was originally designed with a  $2\text{ mm}$  airgap and an operating point high above the knee. After experiencing difficulty in maintaining the desired airgap between the stator and rotor sections, the gap was increased to approximately  $4\text{ mm}$ , although not consistent around the machine. As a result, the actual operating point is unknown but insight is obtained from the shape of the back EMF versus temperature plot.

By measuring the back EMFs induced (i.e. the open-circuit voltages) at different temperatures, this relationship is easily plotted. Heating of the rotors and hence magnets, can be achieved by either convection from the stator (whilst temporarily driving some heavy load) or by an external heat source. Due to the undesired zig-zag flux inherent in the prototype's design, the rotors heated naturally, even under no-load conditions, making the experimental procedure uncannily straightforward; the generator was driven with no-load applied, allowing the rotors and permanent magnets to warm. As the temperatures rose, the back EMFs were periodically recorded,

together with the corresponding rotor temperatures. This process continued until the steady-state operating temperature was reached.

Since direct temperature measurements could not be taken whilst the machine was in operation, a rather elaborate method was initially devised. Coloured temperature strips were pasted onto the rotor and magnet surfaces, as seen in figure 4 of the appendix. It was anticipated that, with the aid of a stroboscope at synchronous frequency, the temperature colours could be read off whilst the machine was running. However, poor illumination of the strip by the stroboscope made the colours indistinguishable. Combined with increments of  $5^{\circ}C$ , this method proved far too inaccurate and inconsistent to gain any repeatable measurements.

The subsequent method employed involved stopping the machine periodically, applying temperature probes and recording measurements. Once stopped, three thermocouples were quickly inserted into small holes bored  $20\text{ mm}$  deep into each backiron, directly behind one permanent magnet per rotor, as shown in figure 5 in the appendix. Once the temperatures had stabilized and were recorded, the probes were removed and the machine was run again. Despite being a time consuming technique, the measurements recorded were accurate to within  $1^{\circ}C$ . Although the short stationary time allowed the rotors an opportunity to cool, due to the poor heat dissipation properties of the flat uniform rotors, the temperature decrease noted was negligible. Because the two outer rotors have a larger area on their outer surfaces from which to radiate heat, whilst running or when stationary, it is not surprising that the inner rotor was always significantly warmer. Measurements from the two end-rotors correlated well with one another whilst the inner rotor was warmer by nearly  $20^{\circ}C$ .

The back EMF versus temperature measurements recorded in table 9 in the appendix are illustrated in figure 4.5. After running the machine for an extended period of time (well over an hour), the temperature rise of the rotors reached a steady-state temperature of approximately  $60^{\circ}C$ . This in turn corresponds to the lowest back EMFs of  $E_{01} = 93.5\text{ V}$  and  $E_{02} = 90.6\text{ V}$  being induced in the respective windings, even under full-load conditions. Since the heating of the rotors occurs naturally whether loaded or not, these back EMF values are used in the models under all load conditions. The slight difference in back EMFs are attributed to the unequal airgaps that exist between each of the two stages.

Comparing the shape of the curves in fig. 4.5 with those in fig. 4.4 suggests that the permeance line along which the prototype machine operates is almost linear, possibly lying somewhere between the **Med Perm.** and **Low Perm.** lines.

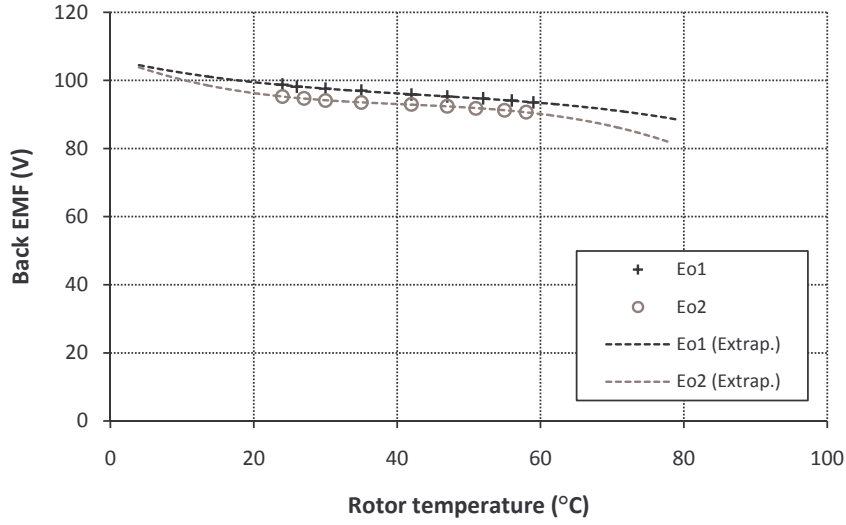


Figure 4.5: Plotted back EMF measurements against increasing rotor temperatures.

#### 4.1.4 Measuring the Rotor Reference Angle (RRA)

Due to the synchronous nature, although the angle between  $\vec{E}_0$  and  $\vec{V}$  changes with load, both phasors continue to rotate at synchronous speed. The angular displacement between the vectors is determined from the ratio of the time delay between them passing a common point, and the period of one cycle; this method could not be used in a machine with a non-zero slip frequency. From the literature, two similar methods for real-time measurement of the load angle are presented [22], [23].

Because  $E_0$  is produced by the permanent magnets on the rotor backiron, the angular position of  $\vec{E}_0$  is along the quadrature-axis of a pole pair. To determine the absolute angle between  $\vec{V}$  and  $\vec{E}_0$ , the delay between the positive-sloped, zero-crossing point of the voltage waveform ( $90^\circ$  ahead of  $\vec{V}$ ) and the direct-axis of one pole pair ( $90^\circ$  ahead of  $\vec{E}_0$ ) can be timed using an oscilloscope. The  $d$ -axis of a pole pair is marked on the prototype machine with a strip of reflective tape and an optical pickup is used as a pulse generator, whilst the voltage zero-crossing point is used to trigger the oscilloscope. For machines where the position of the  $d$ -axis cannot be established, an alternative method is to mark any point on the rotor with reflective tape and time the delay as before. The relative angles determined are then converted to absolute angles by a post-measurement calibration process: by recording the relative angle when minimum current is drawn (i.e. when  $\vec{E}_0$  is known to be inline with  $\vec{V}$  at  $\sigma = 0$ ) this angle can be used to offset the measured angles to their absolute values.

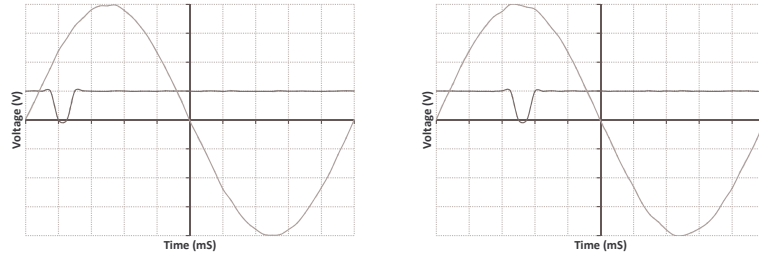


Figure 4.6: Phase voltage and tacho pulse output waveforms when unloaded and loaded respectively, with the oscilloscope being triggered by the phase voltage.

$$\sigma = \frac{360^\circ \times \Delta T}{20\,000} \quad (4.1)$$

Equation 4.1 above relates the time difference  $\Delta T$  (measured in  $\mu s$ ) between the voltage trace and rotor position, to the relative angular displacement between  $\vec{E}_0$  and  $\vec{V}$ , and hence the RRA  $\sigma$ . Since one mechanical revolution at 750 r.p.m. would take 80  $ms$ , one electrical cycle (four pole pairs) would span 20  $ms$ . The oscilloscope used had a maximum resolution of 4  $\mu s$  which therefore introduced some quantization errors. Although noticeable in the resulting synchronous impedances determined, the accuracy is sufficient for modelling purposes. This method proved to be very reliable and repeatable.

#### 4.1.5 Determining the synchronous reactance

The leakage component of the synchronous reactance is governed by the reluctance of the magnetic circuit. Typically for salient pole machines, because the airgaps along the  $d$ -axis and  $q$ -axis are not equal, the leakage inductance becomes a function of rotor position. Since the prototype machine has surface-mounted magnets (considered to have a permeability of free space) and thus a constant airgap, the leakage path remains constant. In theory, the leakage reactance could be quantified by removing the permanent magnets and determining the reluctance of the remaining magnetic circuit. From experience gained during the construction of the prototype, removing the magnets from the rotor backiron would prove impossible. Due to the large airgap in the prototype, saturation effects may be ignored, and hence the armature reaction component can be considered to remain constant. The only feasible method of determining the synchronous reactance is from test and measurement.

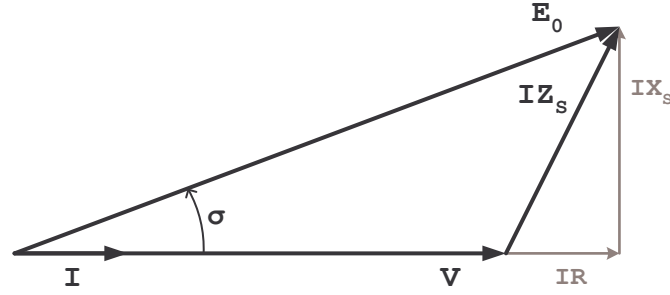


Figure 4.7: Phasor diagram of generator under unity power factor load.

From the equivalent circuit illustrated in fig. 4.1, by applying a unity power factor load, the phasor diagram reduces to a right-angled triangle as per figure 4.7; drawn with  $\vec{V}$  on the base to aid visualization. The pure resistive load results in the stator current being in phase with the supply voltage i.e. unity power factor, irrespective of the RRA  $\sigma$  or load - the prime benefit of testing the machine as a generator.

From the right-angled triangle, the synchronous reactance  $X_S$  can be determined from the reactive voltdrop across  $IX_S$  by Pythagoras's theorem given in 4.2. Because the resistance  $R$  is temperature dependent, the voltdrop across the stator winding  $IR$  does not remain constant and thus introduces too much error.

$$X_S = \frac{\sqrt{E_0^2 - (V + IR)^2}}{I} \quad (4.2)$$

A better method independent of temperature, is to determine  $X_S$  from the sine rule in the right-angled triangle of fig. 4.7, as given in 4.3. For small  $\sigma$ , the small angle approximation can be made to give a simpler expression as in 4.4.

$$\frac{IX_S}{\sin \sigma} = \frac{E_0}{\sin \frac{\pi}{2}}$$

$$X_S = \frac{E_0}{I} \sin \sigma \quad (4.3)$$

$$\text{or } X_S \approx \frac{E_0}{I} \sigma \quad (4.4)$$

With the back EMF already determined, only the load current and the RRA need be measured. Since the function is independent of temperature, this method proves to be very repeatable.

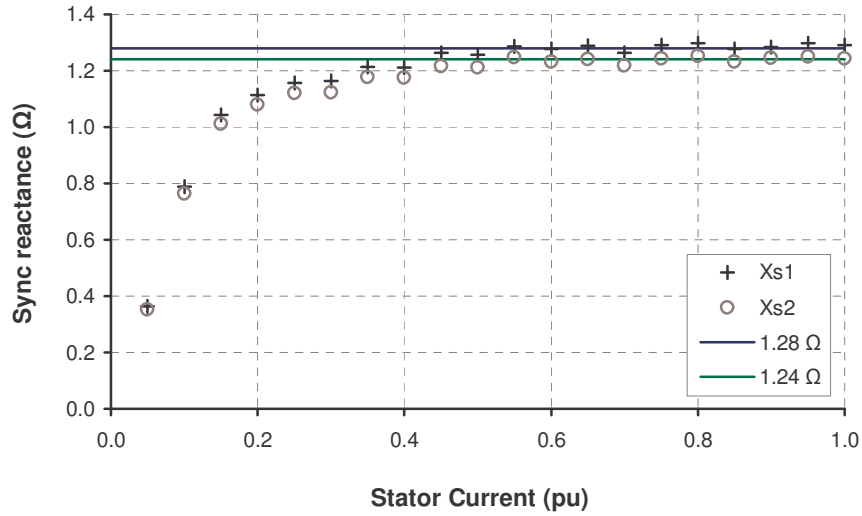


Figure 4.8: Synchronous reactances for each stage plotted against load current.

Equation 4.4 implies that for a constant  $X_S$ , the magnitudes of the RRA and load current must be equal. Measurements of the back EMF, load current and RRA were recorded, as listed in table 10 in the appendix. From these, the synchronous reactances for each stage were determined, as plotted in figure 4.8.

Ignoring the initial points, the synchronous reactance clearly remains constant once the generator is sufficiently loaded. On light load, the small current produces a negligible armature reaction, therefore the synchronous reactance is dominated by the leakage component. Since the actual leakage inductance was not determined, this presumption cannot be verified.

Taking mean lines through the loaded synchronous reactance values (0.5 pu and above) gives constants of  $X_{S1} = 1.28 \Omega$  and  $X_{S2} = 1.24 \Omega$  respectively. Thus the synchronous impedance values used in the modelling equations assume that the machine is significantly loaded. The ripple may be due to the quantization error of the time periods recorded and used to determine the RRA; limited by the bandwidth of the oscilloscope, as discussed.

The equivalent circuit parameters for each stage have now been quantified. The effect of the unequal back EMFs is clearly evident on the synchronous reactances.

### 4.1.6 Measuring the misalignment

The misalignment between the back EMFs can be determined by measuring the phase displacement between the open-circuit voltages of each winding. Using an oscilloscope, the time period between the zero-crossing points of the two waveforms is translated into a mechanical misalignment by 4.1.

From the time measured between the two traces,  $E_{02}$  lags  $E_{01}$  by approximately  $\beta = 0.8^\circ$  (electrical) when rotating clockwise. When rotating counter-clockwise,  $E_{02}$  leads  $E_{01}$  by the same angle. This corresponds to a misalignment of approximately  $0.2^\circ$  (mechanical). For machines comprising additional stages, the model can be expanded by coupling the additional back EMFs and their misalignment with a common reference point, for example the shaft.

Since the accuracy of this measurement is limited by the bandwidth of the oscilloscope, an additional method is employed. Because the difference between the RRAs resulting in current minimums for each stage is also due and equal to the misalignment, by recording the rotor positions at the corresponding current minimums, the misalignment can be calculated. This method proves to be accurate and is used to confirm the misalignment measured above.

## 4.2 Completed Prototype Machine Model

The equivalent circuits for each stage are coupled together via their parallel-connected windings and the common shaft, as illustrated in figure 4.9. The corresponding winding resistances and synchronous reactances are lumped together to form the synchronous impedances  $Z_{S1} = 1.614 \angle 53.1^\circ \Omega$  and  $Z_{S2} = 1.574 \angle 52.0^\circ \Omega$  respectively. The back EMFs are  $E_{01} = 93.5 V$  and  $E_{02} = 90.6 V$  and are misaligned by  $\beta = \pm 0.8^\circ$ , depending on the direction of rotation. The supply voltage to both stages is  $V = 180 V$ .

The model assumes that the machine is operating from a constant supply voltage, that the back EMFs and synchronous reactances remain constant, and that the temperatures of the stator windings and permanent magnets have reached steady-state.

Clearly, the operation of the machine is sensitive to the direction of rotation, as postulated. The main difference between the equivalent circuits of each stage is

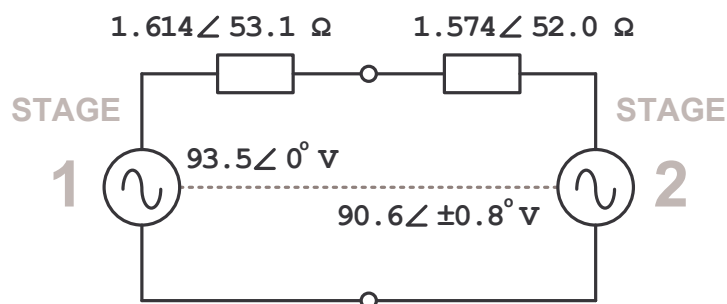


Figure 4.9: Equivalent circuit of the prototype double-stage machine. Note the misalignment between the back EMFs results in *Stage2* lagging/leading *Stage1* by  $+/- 0.8^\circ$  for CW and CCW rotation respectively.

predominately due to the unequal back EMFs; the small mechanical misalignment having a lesser effect.

### 4.3 Model Predictions for Motoring Operation

From the multi-stage equivalent circuit, the derived models for the prototype machine are now presented.

#### 4.3.1 Current versus power factor

Running each stage individually as a motor, the current and power factor relationships are plotted in figure 4.10. By evaluating each stage separately (with the other stage unconnected), the stage current versus power factor models allow easy comparison, independent of the direction of rotation and of any misalignment. This graph is later verified against corresponding measurements to confirm the model parameters.

Clearly noticeable is the discrepancy in currents drawn between the two stages. This is attributed to the difference in voltdrops across the synchronous impedances: although the supply voltages remain constant the back EMFs are unequal. Because the synchronous impedances of both stages are almost equal, the shape of the curves are quite similar.

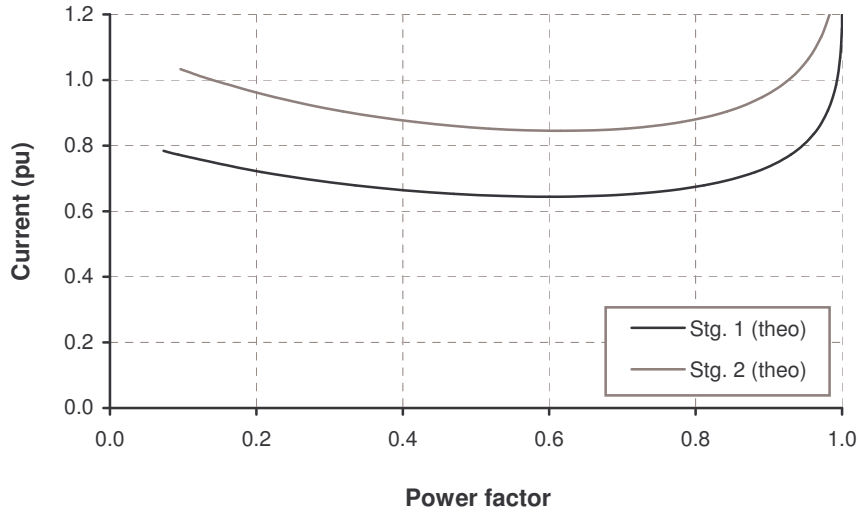


Figure 4.10: Prototype models of current versus power factor for stages running individually; independent of the direction of rotation.

At no-load, due to the poor power factor, the currents drawn are relatively high; comparable to full-load. As the machines<sup>1</sup> are loaded<sup>2</sup>, the power factors improve, resulting in decreasing currents until minima are reached ( $I_1 \approx 0.8$  pu and  $I_2 \approx 0.6$  pu respectively) at a lagging power factor of  $pf_1 = pf_2 \approx 0.6$ . Further loading improves the power factor, and the currents start to rise. At full-load, the effect of the slight difference between synchronous impedances is noticeable: although both stages draw equal rated current at full-load, *Stage1* does so at unity power factor whilst *Stage2* lags slightly. Overloading the machine would result in a leading power factor for *Stage1* and unity power factor for *Stage2*.

### 4.3.2 Power factor versus RRA

Although the power factor is not directly proportional to load, figure 4.11 shows that for loads between no-load and minimum current, as a first approximation, a linear relationship exists; as proposed in Chapter 3.

From the individual stage models in fig. 4.11, at no-load, both stages have similarly poor power factors at clearly different RRAs. As the load increases, the power factors improve and intercept the  $\sigma = 0$  axis at  $pf_1 = pf_2 \approx 0.6$ . This is in agreement with fig. 4.10 where, corresponding to this power factor, minimum currents are drawn.

<sup>1</sup>Each stage being evaluated individually with the other unconnected.

<sup>2</sup>The terms *no-load* and *full-load* are used loosely. Although not plotted directly against load, the power factor is a function of load.

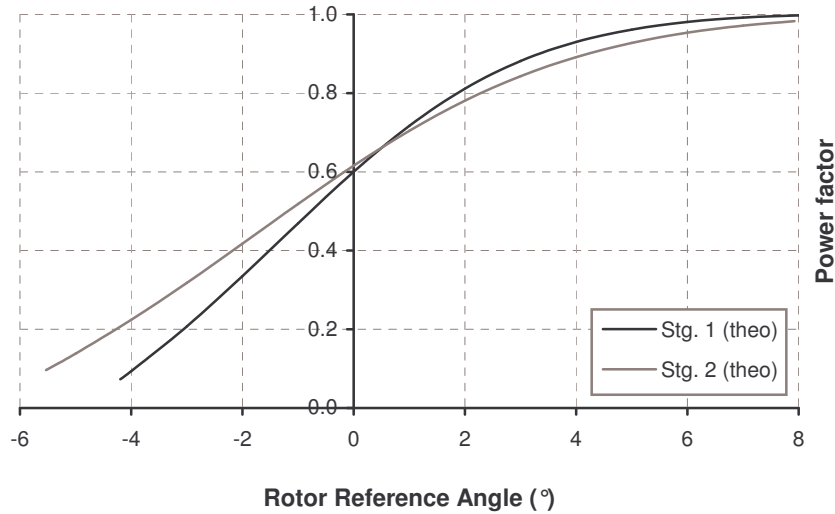


Figure 4.11: Prototype models of power factor versus RRA  $\sigma$  for stages running individually; independent of the direction of rotation.

Further loading results in power factors close to unity at similar RRAs. On light loads ( $-\sigma$  quadrant), the power factor of *Stage1* is generally poorer than *Stage2*, whilst under heavy loads ( $+\sigma$  quadrant), the opposite is evident.

In a multi-stage machine, since  $E_{01}$  and  $E_{02}$  are physically coupled together, when drawn as vectors on the same set of axes, the angular displacement between them is fixed. With  $\vec{E}_{01}$  as a reference,  $\vec{E}_{02}$  would lead or lag  $\vec{E}_{01}$  depending on the direction of rotation. Consequently, introducing the misalignment into the multi-stage model results in a horizontal shift of the *Stage2* curves, relative to those of *Stage1*.

Rotating in the clockwise direction,  $E_{02}$  lags  $E_{01}$  by approximately  $0.8^\circ$ . As a result, the curve of *Stage2* is shifted to the right, as per figure 4.12, whilst the curve of *Stage1* remains in the same position as before. Consequently, a point of equal power factors of  $pf_1 = pf_2 \approx 0.35$  in the  $-\sigma$  quadrant is reached under light loads. At  $\sigma = 0$ , whilst *Stage1* draws a minimum current, *Stage2* has a power factor of  $pf_2 \approx 0.55$ . On heavy loads, the power factor of *Stage1* is clearly better than that of *Stage2*. In general, from no-load to full-load, the power factors of both stages track each other quite well.

For counter-clockwise rotation, the curve of *Stage2* is shifted left, as per figure 4.13. Under light loads, substantially different power factors result for the same RRAs. At  $\sigma = 0$  when *Stage1* draws minimum current, *Stage2* has a power factor of  $pf_2 \approx 0.70$ . The left-shift of the *Stage2* curve results in a point of equal power factors of  $pf_1 = pf_2 \approx 0.85$  in the  $+\sigma$  quadrant. Under heavy loads, both power factors

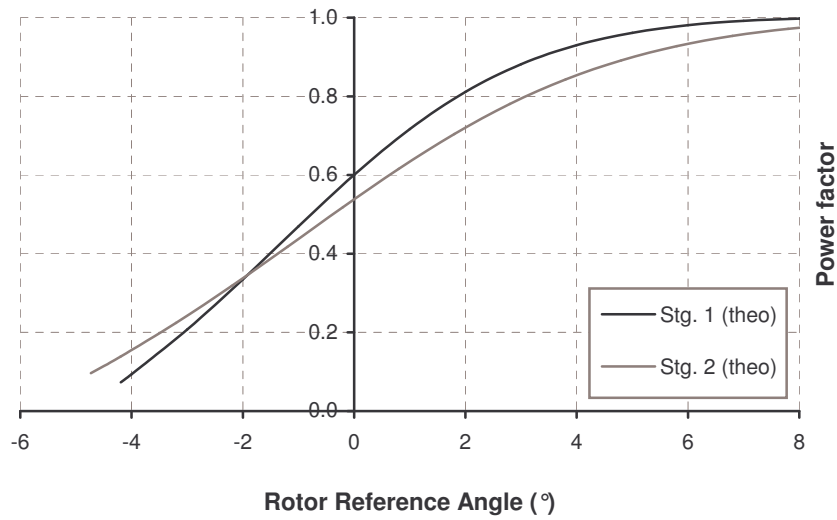


Figure 4.12: Prototype multi-stage model of power factor versus RRA  $\sigma$  for rotation in the CW direction. Note the shift of *Stage2* to the right and hence the equal *pf* point in the  $-\sigma$  quadrant.

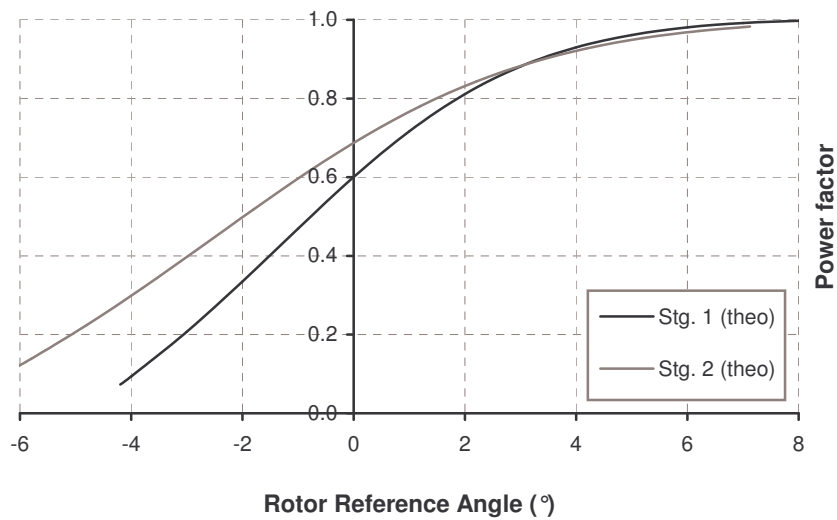


Figure 4.13: Prototype multi-stage model of power factor versus RRA  $\sigma$  for rotation in the CCW direction. Note the shift of *Stage2* to the left and hence the equal *pf* point in the  $+\sigma$  quadrant.

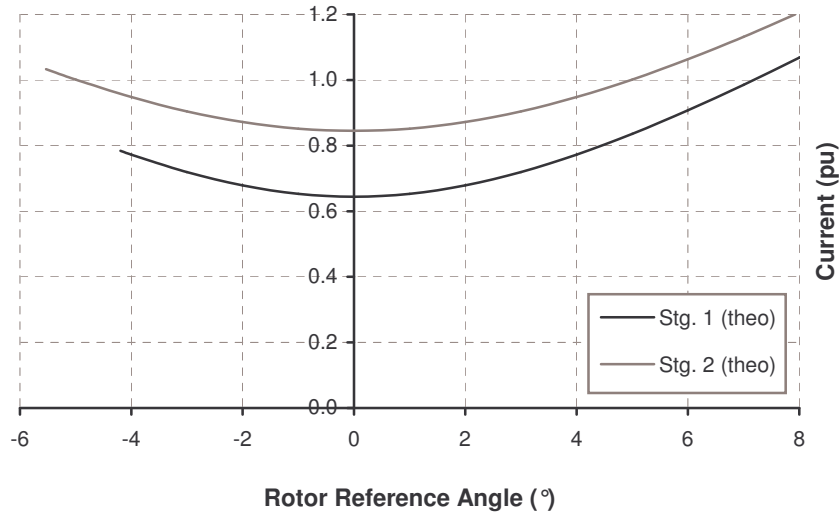


Figure 4.14: Prototype models of current versus RRA  $\sigma$  for stages running individually; independent of the direction of rotation.

converge together and towards unity. From no-load, the power factors steadily converge until full-load, where both curves can be considered identical.

### 4.3.3 Current versus RRA

Figure 4.14 shows that the currents in both stages do not vary significantly over the full load range; the currents drawn at no-load being comparable to those under heavy load. From the individual stage models in fig. 4.14, current minima occur when  $\sigma = 0$ ; as anticipated.

From figure 4.15, for clockwise rotation *Stage2* is shifted to the right, as before. *Stage1* draws a minimum current of  $I_1 \approx 0.6$  pu at  $\sigma = 0$  and, although not clearly visible, *Stage2* reaches a minimum current of  $I_2 \approx 0.8$  pu at roughly  $\sigma = +1^\circ$ . Subsequently, this would imply a misalignment of about  $1^\circ$  between *Stage1* and *Stage2*.

From figure 4.16, for counter-clockwise rotation *Stage2* is shifted left. *Stage2* reaches minimum current at approximately  $\sigma = -1^\circ$ , implying the same misalignment but opposite rotation. In both cases, the curves have similar shapes, owing to their close synchronous impedance values.

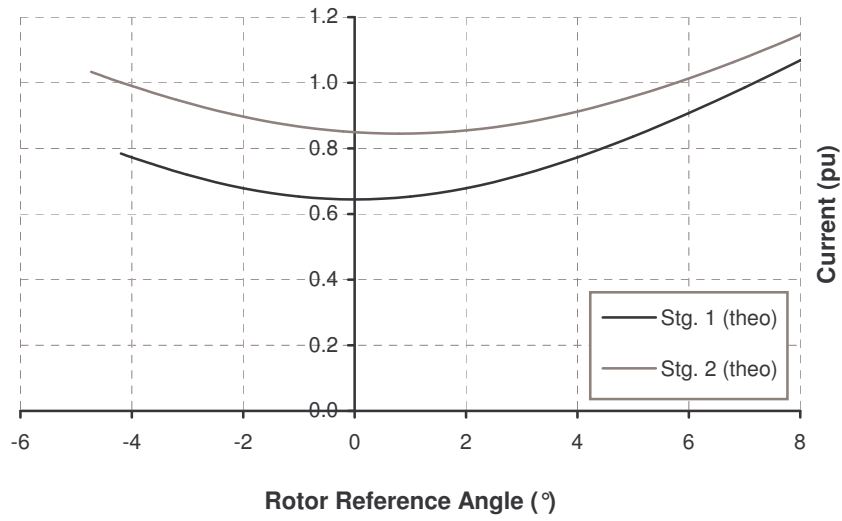


Figure 4.15: Prototype multi-stage model of current versus RRA  $\sigma$  for rotation in the CW direction. Note the current minimum of *Stage2* lagging by  $\sigma \approx +1^{\circ}$ .

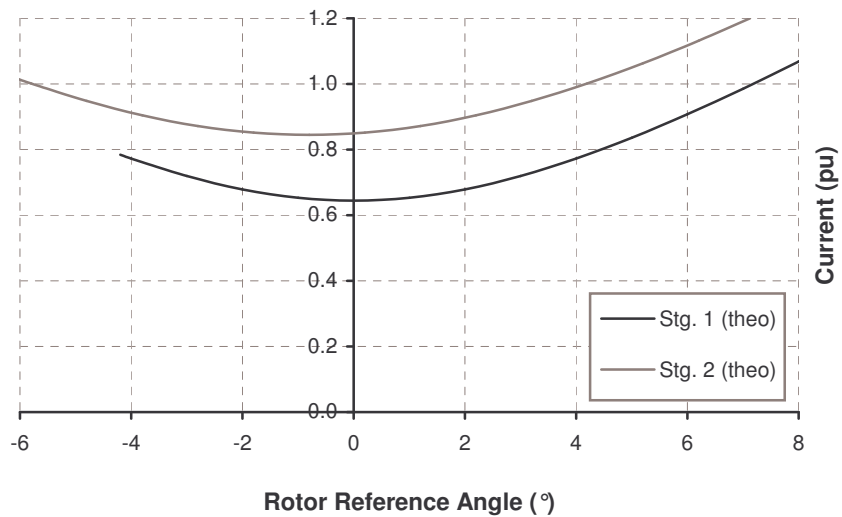


Figure 4.16: Prototype multi-stage model of current versus RRA  $\sigma$  for rotation in the CCW direction. Note the current minimum of *Stage2* leading by  $\sigma \approx -1^{\circ}$ .

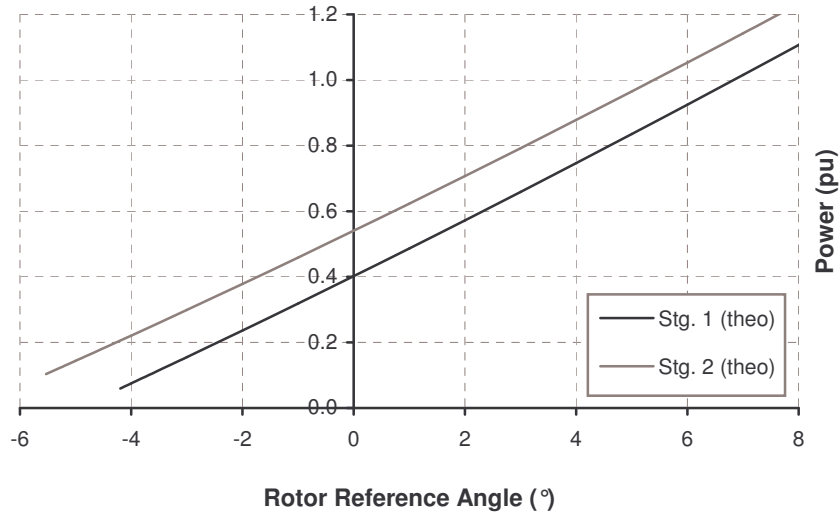


Figure 4.17: Prototype models of power versus RRA  $\sigma$  for stages running individually; independent of the direction of rotation.

#### 4.3.4 Power versus RRA

Figure 4.17 confirms the linear relationship between the power consumed and the RRA. The models in fig. 4.17 show that *Stage2* consistently consumes more power than *Stage1* across the full load range. This is attributed to the lower back EMF of *Stage2* resulting in more current being drawn than in *Stage1*; both stages having roughly the same power factors.

Figure 4.18 shows the power drawn by the prototype for clockwise rotation. The decrease in power consumed by *Stage2* is clearly evident, resulting in better load-sharing across the full load range. For counter-clockwise rotation, figure 4.19 shows that the power consumed by *Stage2* increases, resulting in poorer load-sharing. In both directions, *Stage2* dominates; the difference in power being dependent on the direction of rotation - as identified in the problem statement. From both graphs, the prototype machine is better suited for motoring in the clockwise direction.

The completed multistage models are in agreement with the anomalies identified. In the next chapter, the models are verified and refined with measurement data.

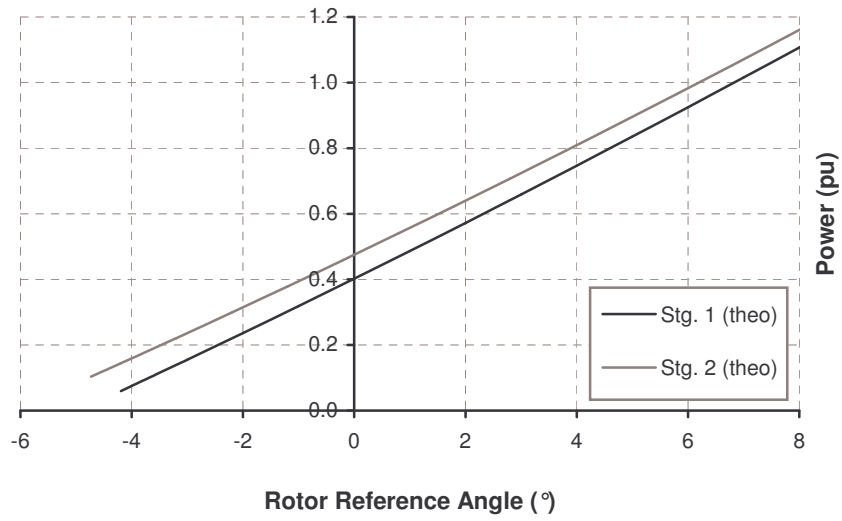


Figure 4.18: Prototype multi-stage model of power versus RRA  $\sigma$  for rotation in the CW direction. Note the decreased power contribution by *Stage2*.

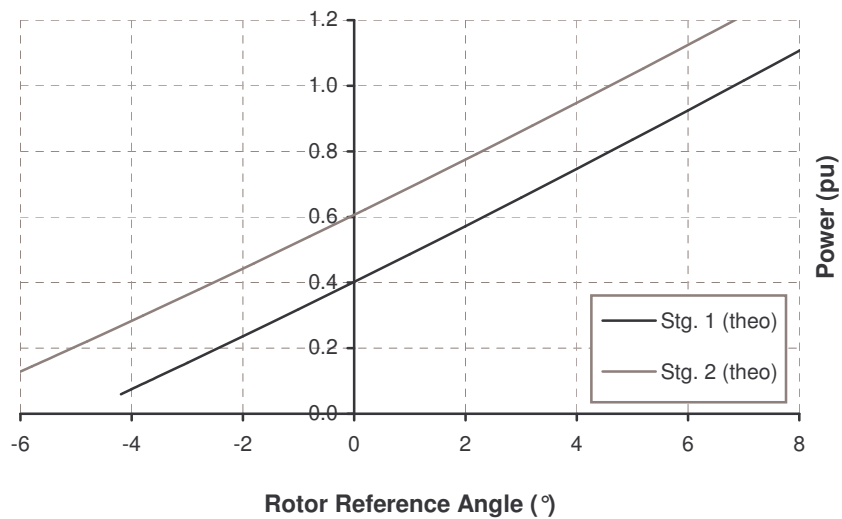


Figure 4.19: Prototype multi-stage model of power versus RRA  $\sigma$  for rotation in the CCW direction. Note the increased power contribution by *Stage2*.

## Chapter 5

# Testing and Results

This chapter presents the tests conducted, the experimental setups<sup>1</sup> used to perform them, their results, and their comparison with the models.

### 5.1 Introduction to Testing

Two sets of tests were performed. The first set was used to determine the machine's equivalent circuit parameters for modelling purposes, in particular, the synchronous reactance. The method employed is discussed in detail in section 4.1.5; the experimental setup used being presented in the following section.

The second set was used to verify the models by running the prototype machine as a motor under various loads. The stages were run individually as separate machines to validate their models. The coupled stages were run to verify the multi-stage machine models, in both the clockwise and counter-clockwise directions. The experimental setup used for these tests is also described in the following section.

### 5.2 Experimental Setup

The first tests were conducted on the machine operating as a generator, whilst the second tests were conducted under motoring conditions. The specifications and serial numbers of all the equipment used can be found in the appendix in tables 4 and 6 respectively.

---

<sup>1</sup>In the figures, solid links between system blocks represent electrical connection paths whilst dashed lines show mechanical coupling.

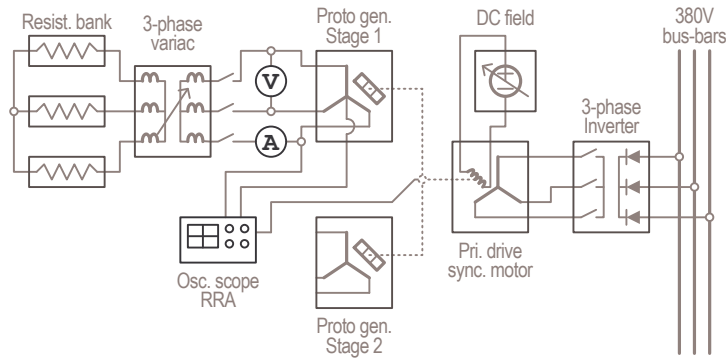


Figure 5.1: Experimental setup for generator-based tests; shown for the individual testing of *Stage 1*.

The choice of instrumentation is briefly motivated. The specifications and serial numbers of the instruments used in the two setups are listed respectively in tables 5 and 7 in the appendix. Whilst running as a generator, since the voltage induced is relatively sinusoidal, readings from the older analogue instruments correlated well with the newer digital ones. However, when running as a motor, since the harmonic content in the current waveform was quite substantial, a noticeable difference between the RMS measurements from both instruments was evident. The analogue instruments naturally filter out all but the fundamental  $50\text{ Hz}$  component. The digital instruments calculate a total harmonic reading, which although more accurate, gives poor correlation with the models; the models assume a generalised machine and consider the fundamental  $50\text{ Hz}$  component only. Consequently, the measurements from the analogue instruments correlate far better with the models derived.

Concerning safety, the inherent beauty of the analogue, dial-gauge type instruments is that one can get a rapid appreciation of the measurement (current, voltage, etc) simply by glancing at the position of the needle relative to the scale without having to process the actual readings; unlike a digital readout where one needs to interpret the display. This is advantageous when risking heavy loads, short circuits, etc.

### 5.2.1 Prototype machine operating as a generator

The equivalent circuit parameters were determined from a generator driving a unity power factor load; the experimental setup is illustrated in figure 5.1. The load was in the form of a resistor bank connected to the output of the prototype machine via a variac. This test could be undertaken by connecting separate loads to each stage and loading them together, or by loading each stage individually with the other unconnected. Either way, the results are the same. Since the load was adjusted

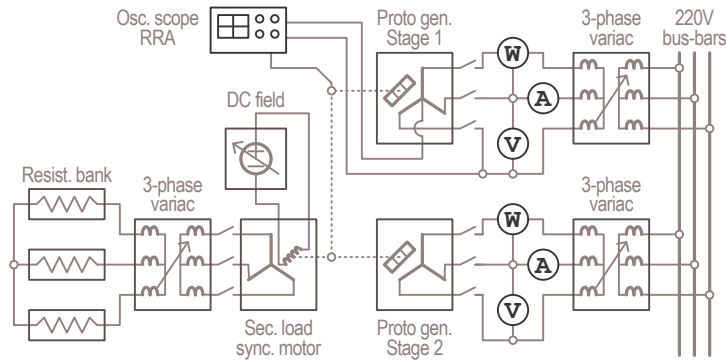


Figure 5.2: Experimental setup used for motoring tests; shown with both stages connected via variacs to emulate an infinite bus-bar supply.

by the variac, finer control and loading could be achieved. A benefit of testing the stages individually is that a smaller driving motor is required.

It must be noted that the variac comprises an internal reactance such that the load seen by the generator is not purely resistive. This reactance however is significantly smaller than the resistive load and hence the power factor is considered to be unity.

The measurements recorded comprised the line voltage, line current and RRA, as listed in table 10 in the appendix. Since the load applied was unity, no power or power factor measurements were necessary. A three-phase breaker was connected in series between the generator and the load, with the voltmeter connected onto the generator's output terminals. The back EMF was measured by momentarily disconnecting the load and measuring the open-circuit voltage of the generator. This assumes that there is no demagnetization of the back EMF under load - a bold assumption that proved to be acceptable. The RRA was measured using the approach described in section 4.1.4. The power produced by the generator is given by  $P = VI$ .

### 5.2.2 Prototype machine operating as a motor

The measurements used for the model verification and refinement were taken from the prototype machine running as a motor under various loads; the experimental setup is illustrated in figure 5.2. The prototype was coupled to a synchronous generator and in turn to a resistor bank, via a three-phase variac. The load was then controlled by adjusting the generator's field excitation. By increasing the field, a heavier mechanical load was seen by the prototype. The three-phase variac connected in series to the resistor bank was to allow for finer load control; if required.

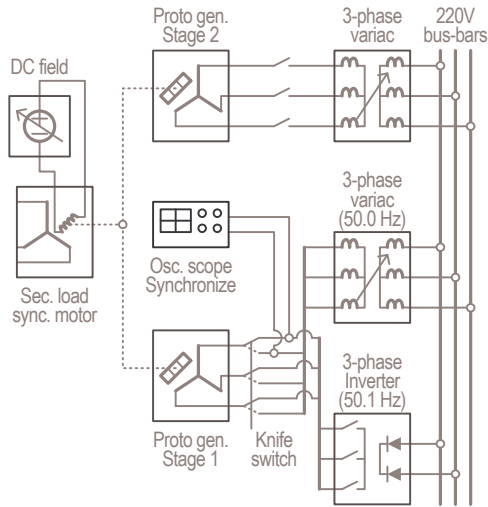


Figure 5.3: Experimental setup used to run-up the prototype machine at start; shown with an inverter supplying *Stage1* via a knife switch.

Each stage of the prototype machine was connected via a circuit breaker to a three-phase variac on the mains supply. The use of the variac on the supply side was to maintain a constant supply voltage of  $180\text{ V}$ ; to emulate infinite bus-bars during load tests.

Being a synchronous machine, the prototype could not be switched directly onto the  $50\text{ Hz}$  mains supply at start. A starting mechanism was implemented by running up the motor via an inverter; once full-speed had been reached, the motor was switched across onto the mains. Only one stage was used to start the machine, using a three-phase knife switch to select the supply source: either mains via variac, or three-phase inverter; as illustrated in figure 5.3. The serial numbers of the additional equipment used are listed in table 8 of the appendix. The inverter had a programmed ramp that would run up the machine on no-load, to a synchronous frequency of  $50.1\text{ Hz}$ . The small difference in supply frequencies allowed the two supply voltages to slowly align in phase with one another. A 2-channel oscilloscope was used as a synchroscope, with one trace monitoring the three-phase supply voltage and the other the inverter's output. Once the two waveforms were in phase, the machine was switched over onto the mains with a rapid flick of the knife switch. Once the torque transients had dampened and the machine had stabilized on the mains, the second stage was energized by closing its circuit breaker. This method, albeit crude and requiring practice, worked relatively well. If the two supplies were not sufficiently in phase, the machine would stall. Once the machine was running from the mains, with either stage supplied individually or both together, the load tests commenced.

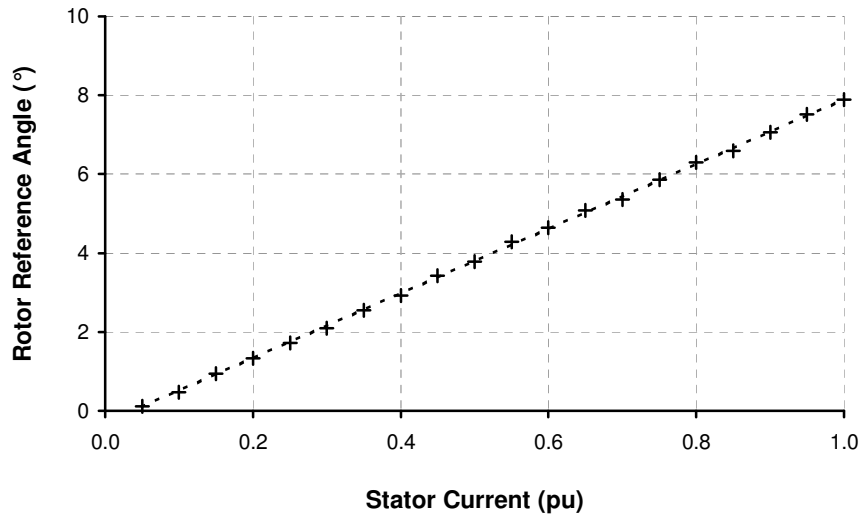


Figure 5.4: Plotted RRA versus load current measurements proving their linear relationship.

The measurements taken included the line voltages, line currents and three-phase powers drawn by each stage. The power was measured using the two-wattmeter method and was used to determine the power factor. Using the method described, the corresponding RRAs were recorded under the various loads.

## 5.3 Verification of Models

The respective models and measurement data are plotted<sup>2</sup> together for correlation and verification purposes.

### 5.3.1 Synchronous reactance

The presumption that the synchronous reactance remains constant over the full load range as per 4.4, assuming that the back EMF does not vary, is verified first. The prototype was operated as a generator and loaded from open-circuit to rated current. The corresponding RRAs were recorded for increasing load currents and are plotted in figure 5.4. The graph clearly shows a linear relationship which confirms that the synchronous reactance remains constant under all loads and that the back EMF does not vary significantly.

<sup>2</sup>Models are shown by continuous greyscale lines, measurement points by discrete markers, and trends by solid colour lines. Where appropriate, the curve fitting equations are published.

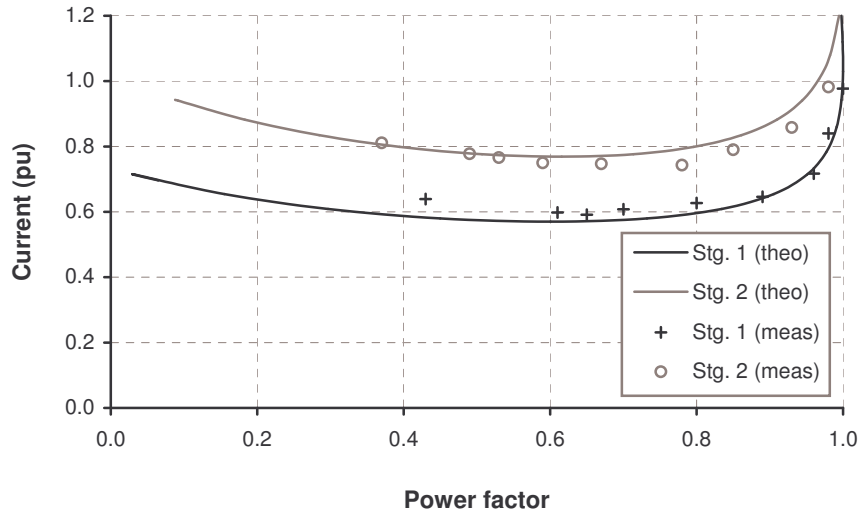


Figure 5.5: Prototype models of current versus power factor for stages running individually, correlating with measurements from tests in the CCW direction.

### 5.3.2 Individual stage models

Each stage of the machine is run individually as a motor and measurements are recorded for increasing loads; the recorded data is listed in tables 11 and 12 in the appendix. Without any intrusive measurements, the models' current versus power factor relationship for each stage is correlated against the measurement data.

Each stage is sequentially tested, with the other left open-circuited. The impact of the uncoupled stage as seen by the one under test is a slight increase in rotational inertia. Since the two stages are decoupled from one another, the individual test results are independent of the direction of rotation. For verification purposes, the two stages are run (arbitrarily) in the counter-clockwise direction. During the tests, the no-load back EMF is recorded between the loading points and used in the models.

From figure 5.5, the theoretical models represent the measurement data relatively well. Examining the curve of *Stage1*, the model fits the higher power factor data points better than the lower ones; evidently, a slight upward shift of the curve will result in closer correlation with all the points. Examining *Stage2*, a slight downward shift of the curve will fit the points better. A vertical shift of the curve is synonymous with a larger or lesser current being drawn. Since the supply voltage to the machine is maintained constant during all tests, only the magnitudes of the synchronous impedance and back EMF are responsible for the resultant current. Furthermore, since the synchronous impedance itself is a function of the back EMF, it becomes

apparent that all theoretical models and measurements are highly sensitive to the magnitude of the back EMF.

### 5.3.3 Model refinement

Accurately measuring the back EMF whilst on load, without an intrusive technique, is somewhat difficult. It was assumed that the back EMF would remain constant under various loads and thus the no-load value would suffice for modelling purposes. Consequently, the corresponding models, although representative of the measured data (as in fig. 5.5), never fit perfectly through the plotted points. Thus, the initial assumption of an invariant back EMF needs revision.

It was initially assumed that the permanent magnet MMF would not demagnetize under load and therefore the back EMF induced in the stator windings would remain constant. The underlying assumption ignores the leakage flux or at least assumes it to be constant. However, as the armature reaction MMF increases, opposing that of the constant field, some flux escapes via the leakage path, resulting in a slightly reduced ( $\approx 1\%$ ) back EMF. Consequently, the no-load back EMF measurements recorded between load points are marginally higher than those under load, and are sufficient for approximation models only; justifying the initial assumption made. For tight correlation between the models and measurement data points, accurate back EMF values are mandatory.

Since the back EMF measurements were recorded at no-load, to save the entire test data from being scrapped, a post-experimental method to accurately determine the back EMFs under load was required. The simplest solution was an iterative process whereby the back EMF and synchronous impedance parameters were fine-tuned until tight correlation between the models and data points was achieved. Once this was completed, the refined models replicate the measurement data almost exactly, allowing the mathematical analysis of the problem to be conducted - as is the purpose of the model.

For each set of tests conducted, the following refinement procedure was followed. The models were first determined from the no-load back EMF values and plotted together with the measurement data. The back EMF and synchronous impedance parameters were then fine-tuned iteratively until the models accurately fitted the measurement data points.

## 5.4 Load Testing of Prototype Multi-stage Machine

Using the procedure outlined above, load tests were conducted on the prototype multi-stage machine for rotation in both the clockwise and counter-clockwise directions. From the measured data recorded in tables 13 and 14 in the appendix, the models were refined until good correlation was achieved, and subsequently used in the mathematical analysis to follow.

The first set of tests conducted is used to verify the multi-stage models. As described, this is easiest done with the current versus power factor relationship. Once the model parameters have been refined, further load tests are conducted for correlation of both the current versus RRA and power factor versus RRA models with the measurement data. Subsequently, the power versus RRA models are then plotted with the identified unbalanced load-sharing measurements, and the correlation between both is used to determine the success of this investigation.

### 5.4.1 Verification of multi-stage models

Using the measured no-load back EMFs and synchronous impedances determined in the previous chapter, the resultant unrefined models of current versus power factor and measurement data are plotted together in figures 5.6 and 5.7 respectively for clockwise and counter-clockwise rotation.

The independence from the direction of rotation and misalignment is evident due to the little difference between the two graphs. Correlation between the models and the measured points is fairly good; in both graphs, the models under-cut the lower power factor points and over-estimate the higher ones. Evident from the graphs, to achieve a better fit, the models need to be pivotted slightly clockwise about their minima points. This is further discussed in this chapter. Also evident is the slight downward shift in position of the *Stage2* curve in the second graph compared to that in the first; as a result of a  $0.6 V$  increase in back EMF due to temperature.

### 5.4.2 Refinement of multi-stage models

The following set of tests conducted is used to compare both the current versus RRA, and power factor versus RRA models with the measured data. In addition to the measurements taken in the previous tests, the RRA is also recorded at the corresponding loads. These measurements are recorded in tables 15 and 16 in the

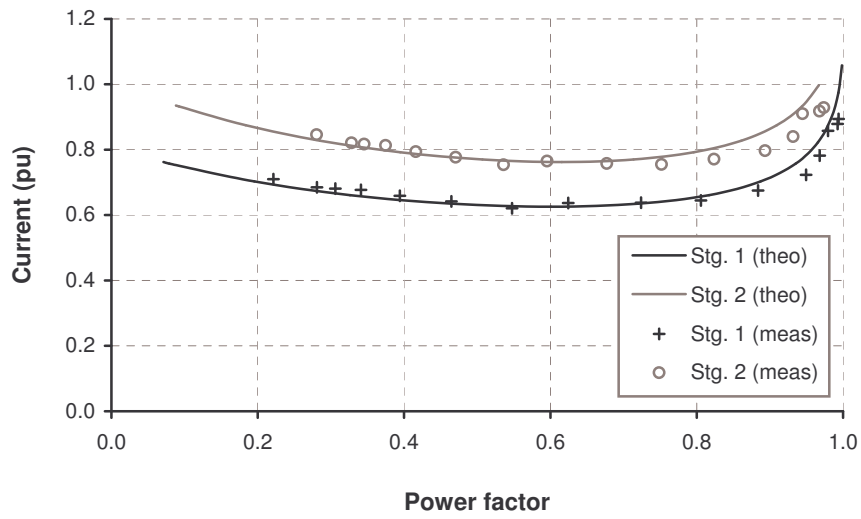


Figure 5.6: Prototype models of current versus power factor verified with measurements for CW rotation.

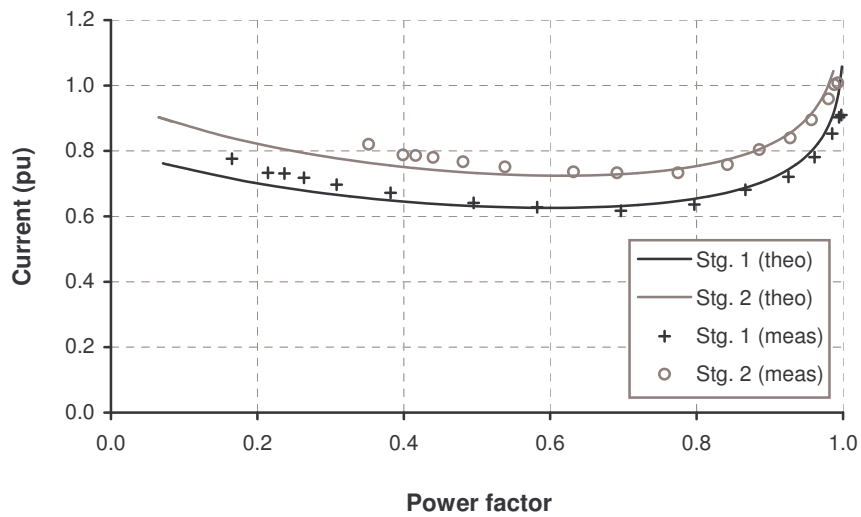


Figure 5.7: Prototype models of current versus power factor verified with measurements for CCW rotation.

appendix. To establish accurate models, the back EMF and synchronous impedance parameters are fine-tuned first. This is done by using the current and power factor measurements recorded to calibrate the models; the refined model parameters are tabled in 5.1 and 5.2. Figures 5.8 and 5.9 illustrate the results of the refined models in correlation with measurements for clockwise and counter-clockwise rotation respectively. By visual inspection, the power factors of both stages are  $pf_1 = pf_2 \approx 0.60$  when minimum currents are drawn.

The two graphs show good correlation of the refined models with the measured data points. Comparing the parameter values in tables 5.1 and 5.2 with those in the equivalent circuit of figure 4.9, only a marginal adjustment has taken place; well within measurement error. By comparing figures 5.6 with 5.8, the slight clockwise pivot of the latter graph to tightly fit the data points may be observed. This is achieved by fine-tuning the impedance angle; adjusting it has a pivoting effect about the current minimum point. The small reduction in impedance angle results in a slight clockwise pivot.

Table 5.1: Refined equivalent circuit parameters used for the CW rotation models.

<b>Stage 1</b>		<b>Stage 2</b>	
$V_1$	103.9 V	$V_2$	103.9 V
$E_{01}$	92.5 V	$E_{02}$	89.9 V
$ Z_{S1} $	1.78 $\Omega$	$ Z_{S2} $	1.73 $\Omega$
$\angle Z_{S1}$	46.0°	$\angle Z_{S2}$	45.0°

Table 5.2: Refined equivalent circuit parameters used for the CCW rotation models.

<b>Stage 1</b>		<b>Stage 2</b>	
$V_1$	103.9 V	$V_2$	103.9 V
$E_{01}$	92.5 V	$E_{02}$	90.3 V
$ Z_{S1} $	1.64 $\Omega$	$ Z_{S2} $	1.60 $\Omega$
$\angle Z_{S1}$	46.0°	$\angle Z_{S2}$	45.0°

Using the refined model parameters, the models of the current versus RRA and power factor versus RRA relationships are plotted.

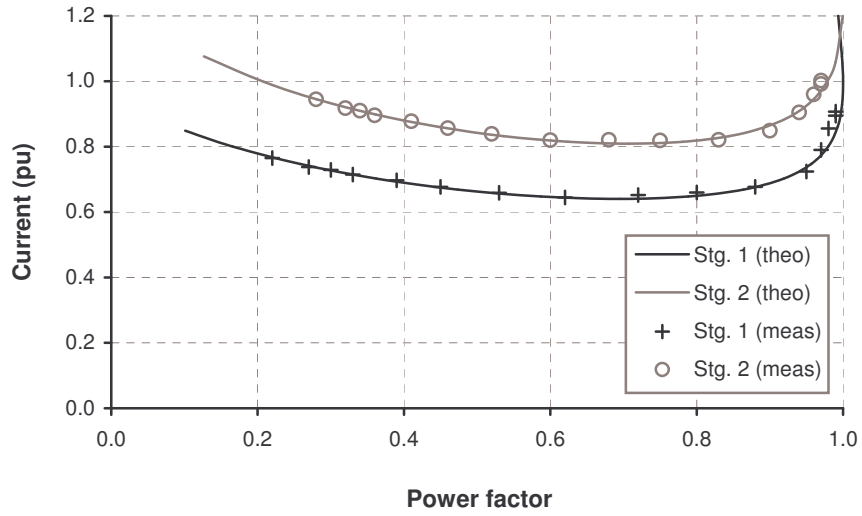


Figure 5.8: Refined prototype models of current versus power factor in correlation with measurements for CW rotation.

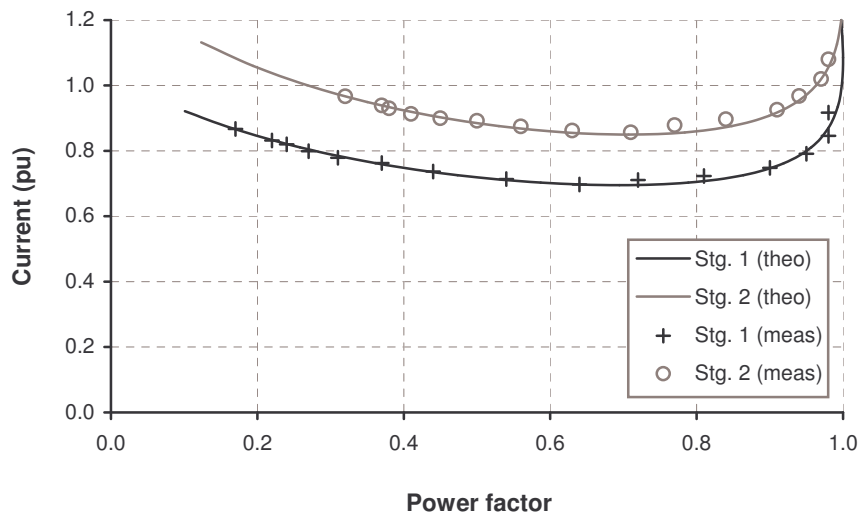


Figure 5.9: Refined prototype models of current versus power factor in correlation with measurements for CCW rotation.

### 5.4.3 Current versus load measurements

As described in section 4.1.4, the RRA is a relative measurement between the back EMF ( $\vec{E}_0$ ) and the supply voltage ( $\vec{V}$ ). To determine an absolute value of  $\sigma$ , a calibration procedure is required. Since at no-load,  $\sigma$  would be a negative maximum, the relative RRA recorded could be used as an offset to subsequent measurements. In the prototype, bearing friction and windage losses appear as a small mechanical load making true *no-load* operation unobtainable. Hence the offset angle from no-load would be prone to significant error.

A better method of calibrating the relative angle to an absolute RRA of  $\sigma$  is to make use of the measured current versus RRA data points. From Chapter 3, when  $\vec{V}$  and  $\vec{E}_0$  are inline at  $\sigma = 0$ , the current drawn is a minimum. Thus the rotor position at this point can be used as an offset to determine the corresponding RRA. The measurements recorded at various rotor positions are then mapped onto an RRA axis via this offset.

From figure 5.10 the current in *Stage1* reaches a minimum before that in *Stage2* when rotating in the clockwise direction i.e. *Stage2* lags *Stage1*. The difference in angle between the minima is due to the misalignment. From the curve fitting equations of the data points, the exact current minima and  $\sigma = 0$  rotor position angles are determined. These are then used as offsets to map the data points onto an *RRA*-axis.

As discussed in Chapter 3, the current versus field angle relationship can be approximated by a quadratic function. The discrete data points are made continuous by curve-fitting a second order polynomial<sup>3</sup>. For quadratic equations of the form  $y = ax^2 + bx + c$ , the x-root of the minimum is given by  $x_{min} = \frac{-b}{2a}$  and the minimum itself is calculated from resubstitution. Therefore the rotor position offset corresponding to a field angle of zero is given by  $x_{min}$ .

Table 5.3 lists the current minima and their corresponding rotor positions determined from the measured data in fig. 5.10. By visual inspection, the values given in the table agree with the fitted curves. Also calculated in the table is the angular difference between the minima equal to the misalignment between  $E_{01}$  and  $E_{02}$ .

The rotor positions are used as offsets to map the measured data to a plot of current versus RRA. Since the position of the current minimum for each stage is used as the reference, once mapped, the two minima sit inline with one another at  $\sigma = 0$ .

---

<sup>3</sup>The corresponding curve-fitting equations are listed in the respective figures.

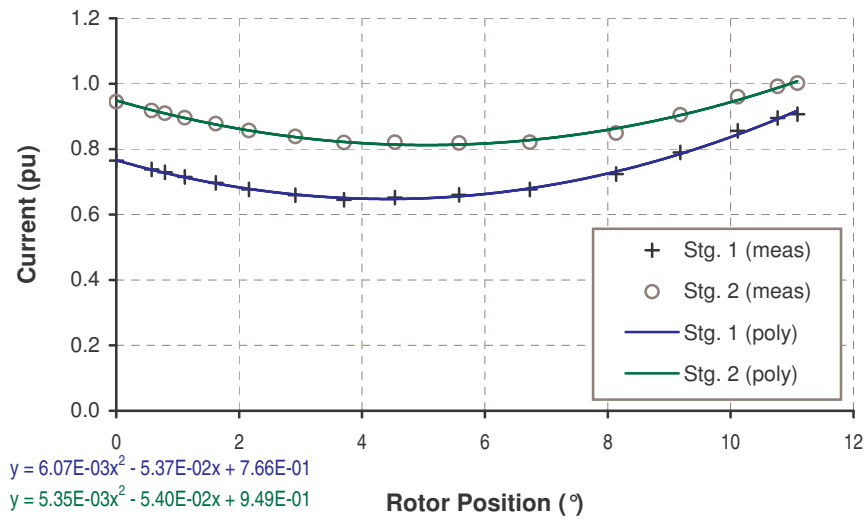


Figure 5.10: Measured currents at corresponding rotor positions, from no-load to full-load, for CW rotation. The current minima are used to determine the rotor position offset from the RRA at  $\sigma = 0$ .

Table 5.3: Rotor position offsets determined from the current minima measured for CW rotation.

Stage 1		Stage 2	
$I_{min}$	0.65 pu	$I_{min}$	0.81 pu
@ rotor pos.	4.42°	@ rotor pos.	5.05°
Angular misalignment = +0.63°			

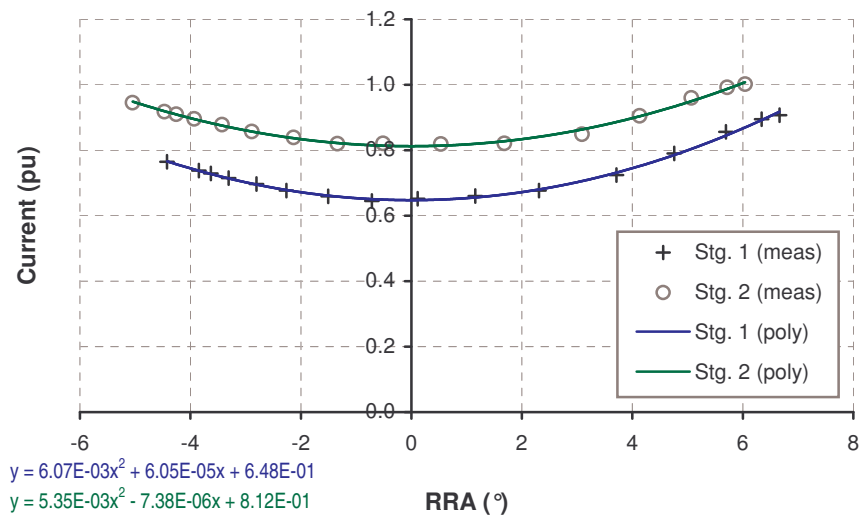


Figure 5.11: Measured currents mapped onto individual RRA axes, corresponding from no-load to full-load, for CW rotation.

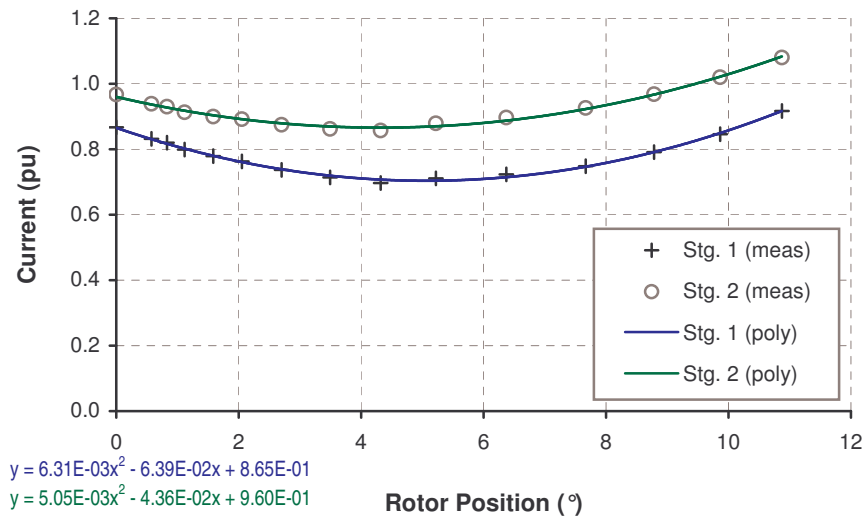


Figure 5.12: Measured currents at corresponding rotor positions, from no-load to full-load, for CCW rotation. The current minima are used to determine the rotor position offset from the RRA at  $\sigma = 0$ .

Table 5.4: Rotor position offsets determined from the current minima measured for CCW rotation.

Stage 1		Stage 2	
$I_{min}$	0.70 pu	$I_{min}$	0.87 pu
@ rotor pos.	5.06°	@ rotor pos.	4.32°
Angular misalignment = -0.74°			

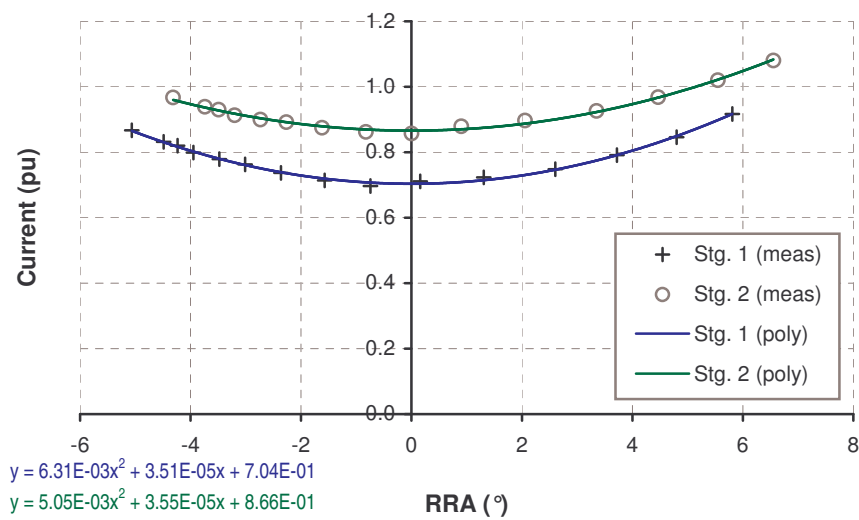


Figure 5.13: Measured currents mapped onto individual RRA axes, corresponding from no-load to full-load, for CCW rotation.

Figure 5.11 shows the mapped data onto a RRA axis. The same graphs would result if the stages were tested as individual motors since the misalignment in the rotor position no longer exists.

From figure 5.12, the current in *Stage2* reaches a minimum before that in *Stage1* when rotating counter-clockwise i.e. *Stage2* leads *Stage1*. From the curve fitting equations, the current minima and their corresponding rotor positions are listed in table 5.4, as well as the misalignment. The mapped current versus RRA plot is given in Figure 5.13.

These current versus RRA plots share a common *RRA*-axis, as if the stages were run individually as motors; independent of the misalignment. By reintroducing the misalignment, the curves are shifted to represent a multi-stage machine.

#### 5.4.4 Rotor misalignment

From the current minima positions in tables 5.3 and 5.4, the misalignment between the back EMFs of *Stage1* and *Stage2* is calculated from the difference in rotor position angles; the sign resulting from the direction of rotation. Using the position of *Stage1* as a reference, for clockwise rotation *Stage2* lags by  $+0.63^\circ$  whilst for counter-clockwise rotation, *Stage2* leads by  $-0.74^\circ$ . The magnitudes of the calculated misalignments correlate well with the  $0.8^\circ$  measured in section 4.1.6 and with one another, with the error between them of less than 0.05% over an electrical cycle. Since these values are calculated from the curve-fitted data points, the accuracy depends on the measurement error of the data itself and the rounding of the equation coefficients. Despite this, this method proves itself to be more accurate than the misalignment measurement carried out in Chapter 4.

By reintroducing the misalignment, the curves are shifted appropriately to represent a multi-stage machine. The misalignment is reintroduced into the current versus RRA plots by holding *Stage1* at  $\sigma = 0$  and shifting *Stage2* by the misalignment either left or right, depending on the direction of rotation. For clockwise rotation, *Stage2* in fig. 5.11 is shifted by  $+0.63^\circ$  producing figure 5.14. The same result is achieved by mapping both curves in fig. 5.10 onto the *RRA*-axis using the *Stage1* clockwise rotor position offset in table 5.3.

From the curve fitting equations given in fig. 5.14, the current minima and their corresponding RRAs are listed in table 5.5. In figure 5.15, the model curves are overlaid on the measured data, and show good correlation.

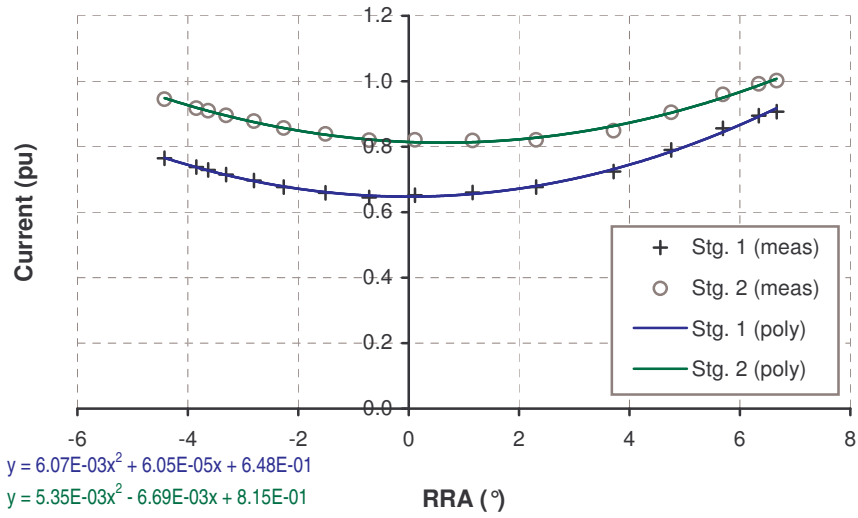


Figure 5.14: Measured currents mapped onto a common  $RRA$ -axis, from no-load to full-load, for CW rotation.

Table 5.5: Current minima and corresponding RRAs for CW rotation.

Stage 1		Stage 2	
$I_{min}$	0.65 pu	$I_{min}$	0.81 pu
@ field ang.	$0.00^\circ$	@ field ang.	$+0.63^\circ$

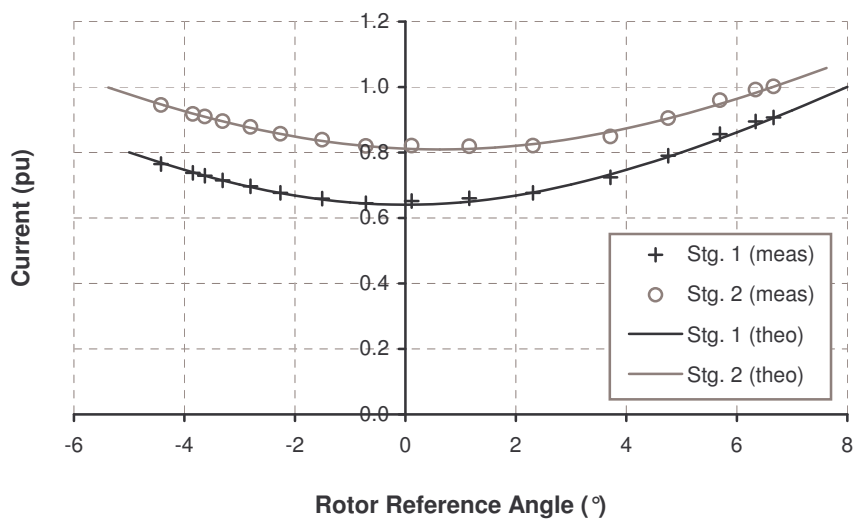


Figure 5.15: Prototype model of currents versus  $RRA \sigma$  in correlation with mapped measurements, from no-load to full-load, for CW rotation.

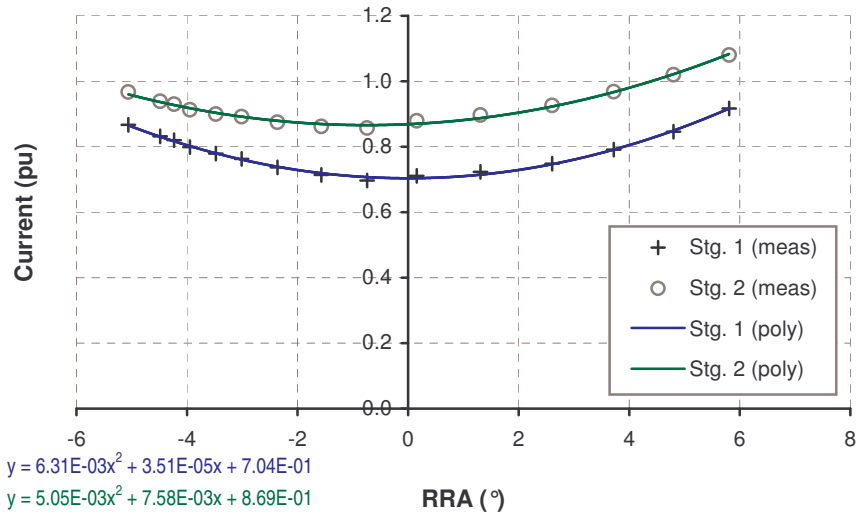


Figure 5.16: Measured currents mapped onto a common  $RRA$ -axis, from no-load to full-load, for CCW rotation.

Table 5.6: Current minima and their corresponding RRAs for CCW rotation.

Stage 1		Stage 2	
$I_{min}$	0.70 pu	$I_{min}$	0.87 pu
@ field ang.	$0.00^\circ$	@ field ang.	$-0.75^\circ$

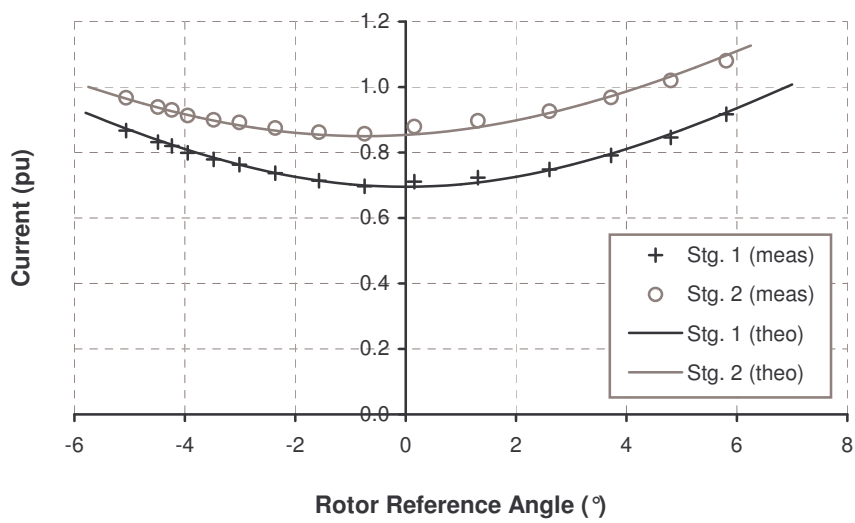


Figure 5.17: Prototype model of currents versus RRA  $\sigma$  in correlation with mapped measurements, from no-load to full-load, for CCW rotation.

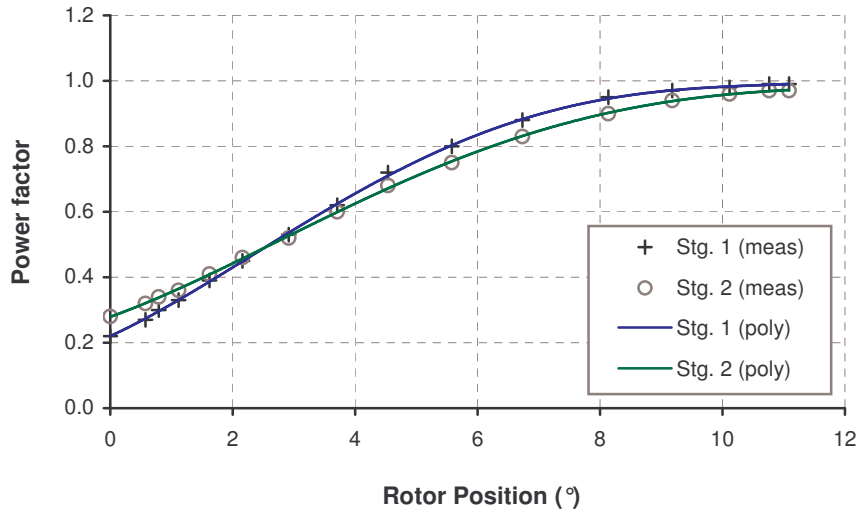


Figure 5.18: Measured power factors at corresponding rotor positions, from no-load to full-load, for CW rotation.

For rotation in the counter-clockwise direction, the curve of *Stage2* in fig. 5.13 is shifted by  $-0.74^\circ$  to the left, producing figure 5.16. Table 5.6 gives the current minima and their corresponding RRAs, obtained from the curve fitting equations. The model curves correlate well with the measured data, as shown in figure 5.17.

#### 5.4.5 Power factor versus load measurements

During the load tests, the corresponding power factors were recorded together with the currents and the rotor positions, and are plotted in figures 5.18 and 5.19 for clockwise and counter-clockwise rotation respectively. Unlike the current, there is no special condition between the power factor and the RRA that can be used to calibrate the rotor position. Since the power factors were recorded at the same rotor positions as the currents, the power factors are mapped onto the *RRA*-axis via the same offsets calculated in tables 5.3 and 5.4.

For clockwise rotation, both curves of fig. 5.18 are mapped onto an *RRA*-axis via the rotor position offset of *Stage1* in table 5.3 (i.e.  $-4.42^\circ$  left) to produce figure 5.20. Fourth-order polynomials are used to make the discrete points continuous, as shown.

From fig. 5.20, a point of equal power factor is reached in the left quadrant. Solving for the intersection point from the polynomials is somewhat difficult. Since the curves are relatively straight at the point of interest, linear interpolation between

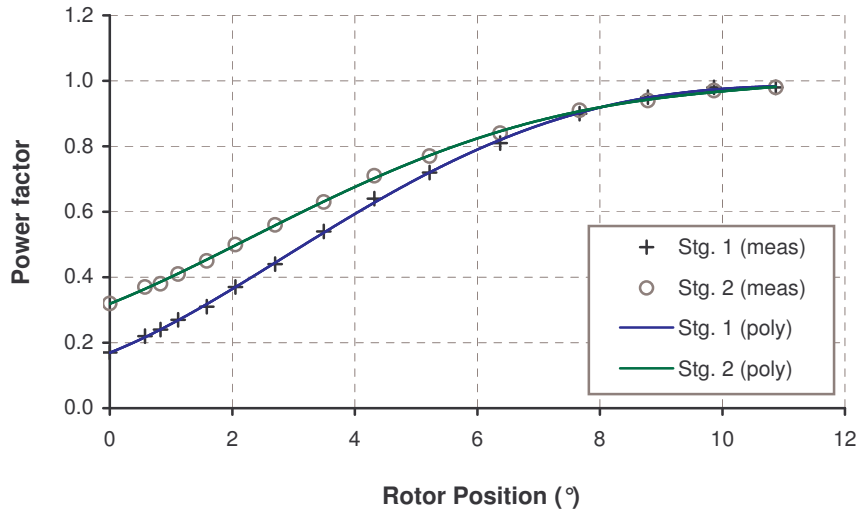


Figure 5.19: Measured power factors at corresponding rotor positions, from no-load to full-load, for CCW rotation.

the adjacent data points is sufficient, as shown in figure 6 in the appendix. The intersection point and the corresponding power factor is given in table 5.7.

When minimum current is drawn by *Stage1*, the power factors corresponding to  $\sigma = 0$  are given by the y-intercept of the curve fitting equations: 0.70 and 0.66 for *Stage1* and *Stage2* respectively. Comparison with the overlaid models as shown in figure 5.21 shows that good correlation has been achieved.

For counter-clockwise rotation, both curves in 5.19 are mapped onto a *RRA*-axis via the rotor position offset of *Stage1* in table 5.4 (i.e.  $-5.06^\circ$  left) to give figure 5.22.

From fig. 5.22, a point of intersection exists in the right quadrant. A second order quadratic equation can be used to interpolate between the adjacent points as shown in figure 7 in the appendix. The point of equal power factors is given in table 5.8.

When *Stage1* draws minimum current, the power factors corresponding to  $\sigma = 0$  are given by the y-intercept of the curve fitting equations: 0.70 and 0.76 for *Stage1* and *Stage2* respectively. From figure 5.23, good correlation between the models and data points is clearly shown.

With the accurate models of current versus *RRA* and power factor versus *RRA*, the power versus *RRA* model can now be evaluated.

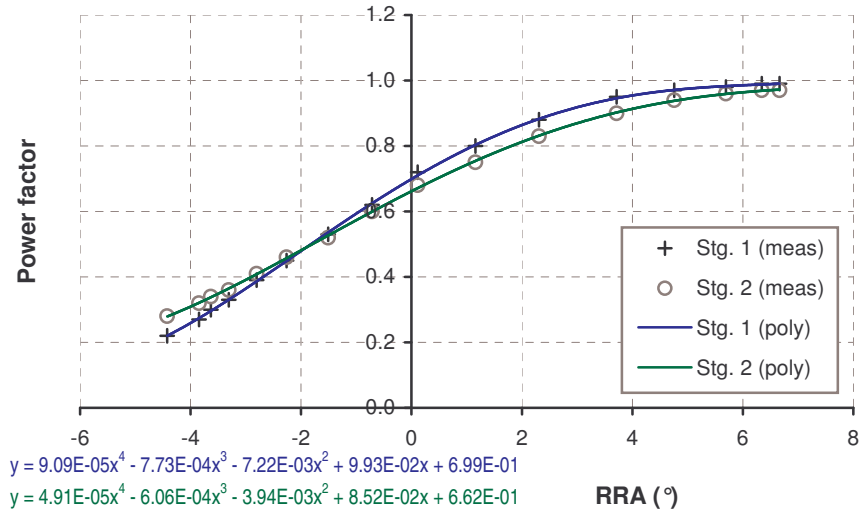


Figure 5.20: Measured power factors mapped onto a common  $RRA$ -axis, from no-load to full-load, for CW rotation.

Table 5.7: Points of equal power factor for CW rotation.

Stage 1 and Stage 2	
equal $pf$	0.51 @ $RRA$ $-1.75^\circ$

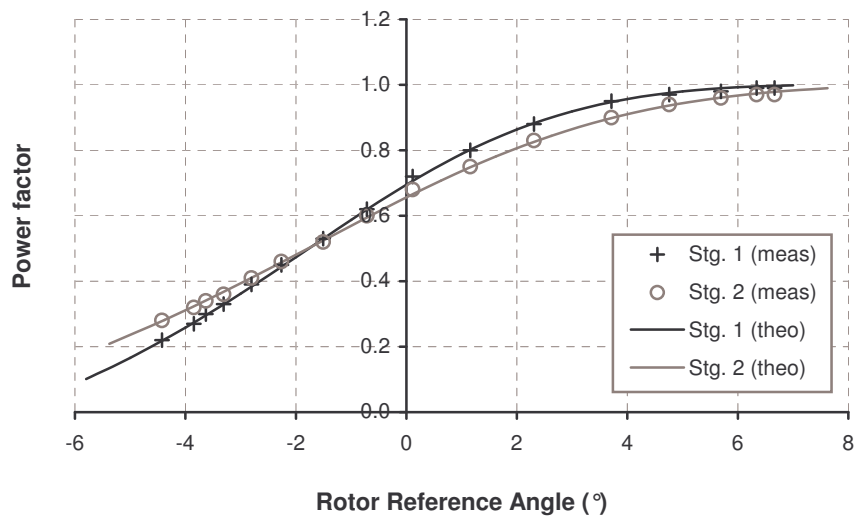


Figure 5.21: Prototype model of power factor versus  $RRA$   $\sigma$ , in correlation with mapped measurements, from no-load to full-load, for CW rotation.

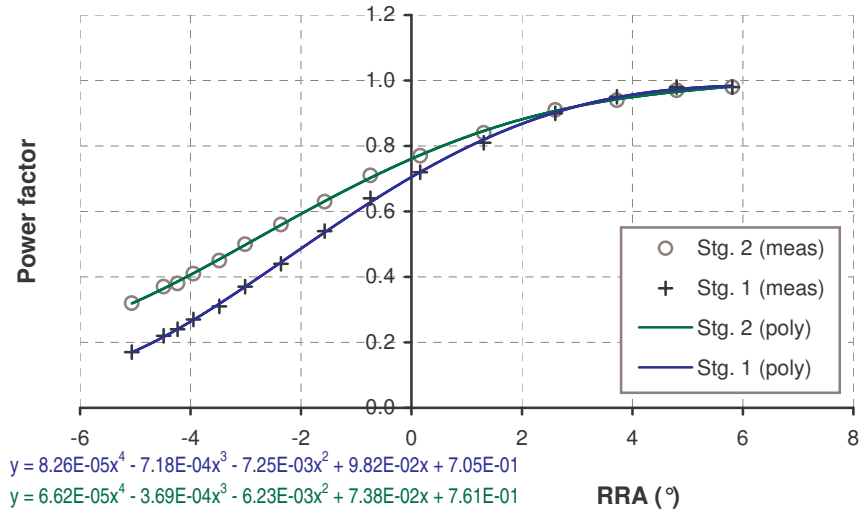


Figure 5.22: Measured power factors mapped onto a common  $RRA$ -axis, from no-load to full-load, for CCW rotation.

Table 5.8: Point of equal power factor for CCW rotation.

Stage 1 and Stage 2		
equal $pf$	0.94	@ RRA +3.71°

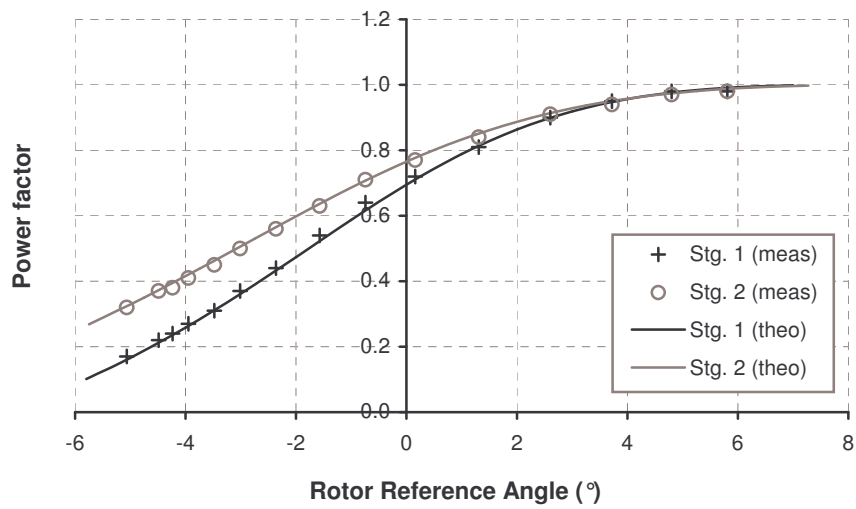


Figure 5.23: Prototype model of power factor versus  $RRA \sigma$ , in correlation with mapped measurements, from no-load to full-load, for CCW rotation.

### 5.4.6 Power versus load measurements

As described in section 3.2.4, the power is given by  $P(\sigma) = VI(\sigma)pf(\sigma)$ ; essentially the multiplication of a constant supply voltage, with the current versus RRA models and the power factor versus RRA models. During the load tests, the input powers were recorded, together with the other measurements, at each corresponding rotor position. The power measurements are mapped onto the *RRA*-axes via the corresponding *Stage1* rotor position offsets given in tables 5.3 and 5.4 respectively.

For rotation in the clockwise direction, the refined power model is given by the multiplication of figures 5.15 and 5.21 at the discrete load points, scaled by the constant supply voltage  $\left(\frac{180}{\sqrt{3}} V\right)$ , and normalised. The result, showing both the model curves and measurement points, is illustrated in figure 5.24.

For counter-clockwise rotation, the refined power model is derived from figures 5.17 and 5.23. Both the model curves and measurement points are plotted in figure 5.25.

In both figures, the models correlate well with the measurements, hence supporting the theory presented, relationships derived and assumptions made. As postulated in section 4.3.4, the direction sensitivity is clearly apparent. From fig. 5.24, the load-sharing between the stages improves for rotation in the clockwise direction. However, from fig. 5.25, the load-sharing becomes worse for counter-clockwise rotation.

To summarize: the equivalent circuit of the prototype multi-stage machine was determined in Chapter 4. Two key differences between the individual stage models are the back EMFs and synchronous impedances. Since the synchronous reactance is also dependent on the back EMF, the unequal magnitudes of the back EMFs has a significant impact on the individual models, with the misalignment between them playing a smaller part.

Since *Stage2* has a lower back EMF, with a common supply voltage, the current drawn is comparatively higher than that of *Stage1*. Furthermore, since both stages have similar power factors, *Stage2* always consumes more power.

The misalignment between the rotors causes the back EMF of one stage to lead or lag the other, depending on the direction of rotation, shifting the current and power factor curves respectively. As a result, the power contribution is dependent on the direction of rotation; as identified in the problem statement and confirmed by the final two graphs.

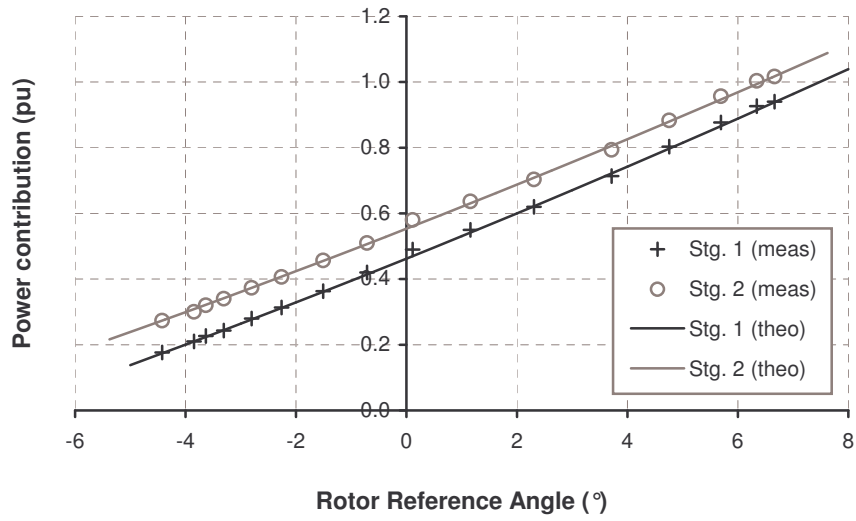


Figure 5.24: Prototype model of power versus RRA  $\sigma$ , in correlation with mapped measurements, from no-load to full-load, for CW rotation.

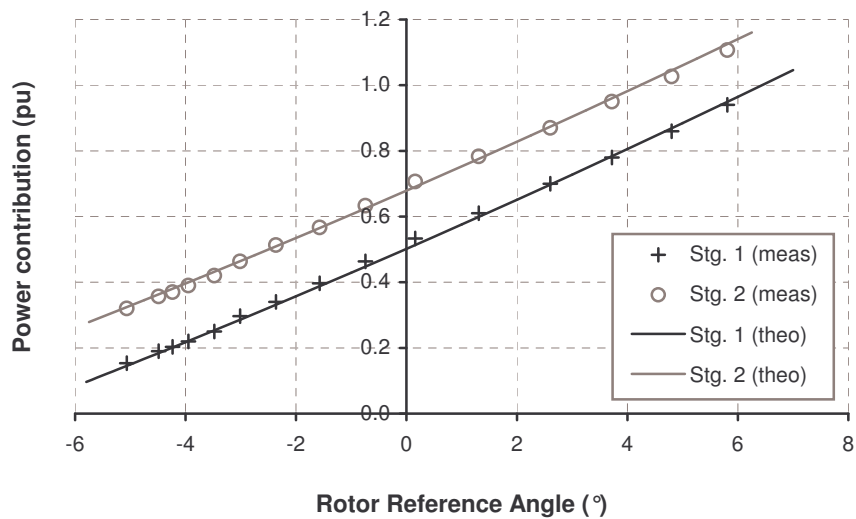


Figure 5.25: Prototype model of power versus RRA  $\sigma$ , in correlation with mapped measurements, from no-load to full-load, for CCW rotation.

## Chapter 6

# Review and Conclusion

### 6.1 Review of Project

This research was initiated after an unequal load-sharing anomaly was noticed during the testing of a prototype multi-stage machine. The power contribution from each stage was unequal and the discrepancy depended upon the direction of rotation. This resulted in one stage being overloaded; drawing a higher current and having a poorer efficiency - certainly not exploiting the benefits of the machine it was intended to be.

The research started with the identification of the problem. The appropriate synchronous machine theory was then reviewed. From the equivalent circuit and phasor diagram representations, the modeling equations were derived. The power consumed in each stage comprises three parts: a constant voltage, and two functions of load: current and power factor; where the load is represented by the rotor reference angle. With the relationships of the latter two functions investigated, performance predictions are then made for the individual stage models.

A spin-off from the research was a method of determining the synchronous reactance. Being dependent on external measurements only, it proved very reliable and repeatable. It required the measurement of the rotor reference angle (the angle between the supply voltage and back EMF), obtainable from a position-triggered tachometer. From various methods and generator tests, the synchronous impedance was determined and the equivalent circuits were derived.

Once the stage models were derived, the effect of stacking them together onto a common shaft was investigated. The stacked nature couples multiple stages together via

an electrical and mechanical link: the supply voltage (parallel-connected windings) and misalignment (fixed rotors on a common shaft). With the individual stages coupled together via these two links, the possibility for an unbalanced situation arises.

The research continued by coupling the respective equivalent circuit diagrams together, fixed by the supply voltage, and by the misalignment angle between the back EMFs. From the experimental data recorded, the measurements were used to verify and refine the models, until accurate correlation was achieved; key to the success of the modelling. From the comparison of the derived models with the power measurements that instigated this research, the cause of the problem has been established.

With the knowledge gained, considerations are given for the future design of axial-flux machines.

## 6.2 Conclusion

This research concludes that the cause of the unequal load-sharing in the prototype multi-stage machine is primarily due to the difference in back EMFs induced in each stator winding, as a result of the unequal airgaps that exist between the two stages. A secondary influence is the slight mechanical misalignment that exists between the two rotors, inducing back EMFs slightly out of phase, and hence making the power contribution of each stage direction sensitive. Simply stacking additional stator and rotor sections onto a common shaft, as proposed by the literature, proved naïve and resulted in complications which outweigh the benefits of such a topology. With the high power densities offered by multi-stage machines, they are suitable for restricted volume applications, and together with their high torque and low speed characteristics, may be the future drives of electric vehicles. With these opportunities for their use in mind, design considerations are given for their future development.

## 6.3 Future Work

Since the prototype was designed as a proof-of-concept machine, despite its drawbacks, its purpose has been successful. The improvements proposed are for the benefit of future designs and not for the rectification of the prototype.

### 6.3.1 Considerations for future variations of the prototype

Despite synchronous operation, the rotor backiron should be constructed from laminated steel. Due to the zig-zag flux causing eddy currents in the solid backiron, heating of the rotor disks resulted in a decrease in back EMF due to the temperature rise of the magnets. To minimize the zig-zag flux, semi-closed slots should be employed. The star connection point should be accessible and allow for reconfiguration into delta. By connecting the two stator sections in series, the voltage across each stator winding would balance, as a result of the common current. Although this may be a simple solution to the problem, the inherent benefits of parallel-connected, multiple stages are lost.

Since the unequal and misaligned back EMFs are the main cause of the problem, an immediate solution may include the following two considerations:

- By building into the rotor disks some kind of locking device (such as a taper-lock bushing) that would allow fine adjustment, any misalignment of the rotors or unequal airgaps could be rectified. By measuring the generator open-circuit voltages, once equal airgaps and alignments have been achieved, the rotor disks would then be rigidly clamped onto the shaft. This could be done prior to the final quality assurance step in a manufacturing process.
- By including in the machine's design a field winding in addition to the permanent magnets on the rotor, the magnitude of the back EMFs could be balanced with the aid of some power electronics, to actively boost the field MMF. Although this may require the use of slip rings, it is beneficial in a generator application where a constant terminal voltage is required.

### 6.3.2 Considerations for future developments

Because the solutions above may not be feasible or cost effective for mass produced machines, the choice of topology is reviewed to ascertain whether another configuration would result in lesser susceptibility to the problem.

Assuming that the prototype machine had identical magnets and equal reluctance paths, the flux through each pole would be constant. With two similar stator windings, the back EMFs induced would also be equal. The prototype inherited unequal airgaps from difficulties experienced during its construction, and consequently unequal reluctance paths. The effect of the difference in fluxes is briefly explored.

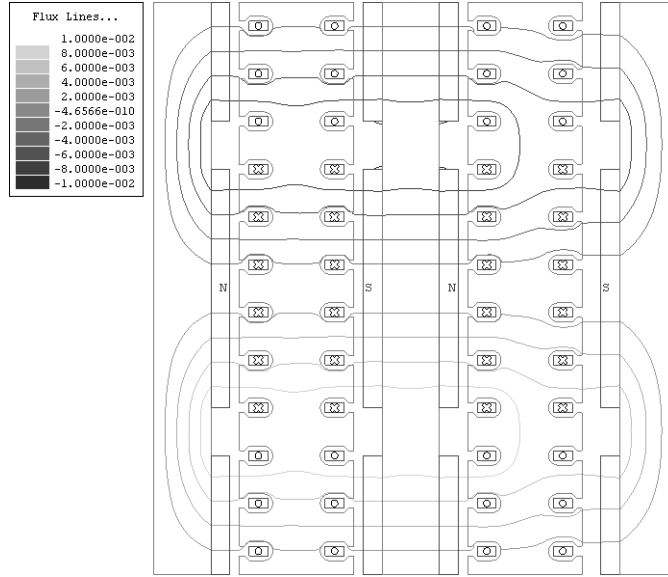


Figure 6.1: Axial flux path through machine with an extended right-most airgap.

Consider a machine with equal airgaps bar one, as per figure 6.1. In this demonstration model, the right-most airgap has been doubled in length.

From the plot, flux still enters the second stage but establishes an additional path through the stator core, parallel to the end-rotor backiron. If the stator winding comprises two series-connected coils distributed on both the left and right surfaces as indicated, then only the left coils would link with the total pole-flux, whilst the right coils would link with the balance. In this case, since the total flux in the coils is now less than that in the left hand stator winding, a reduced back EMF would be seen in the right stage.

With this topology, an unbalanced airgap has two impacts: firstly, the increased airgap presents a higher reluctance path and hence less flux is produced by the field; secondly, since the reluctance paths are no longer balanced, a parallel path now exists through the stator core. Although the total flux remains the same, the flux linkage in each coil is no longer equal, resulting in a further decrease in the back EMF induced.

Ideally a minimum number of coil groups is required to reduce the dependence on the multiple flux paths. In the demonstration model above, four coil groups (two on each side of both stages) link with the same pole-flux. As described, the flux seen by one of the groups may not be the same as that of the others. Putting all the coil groups of each stage... on one side would reduce the coil groups to two, but may present construction complications - hence the initial reason for splitting them in the first place. One idea is to introduce a high reluctance path in the circumferential

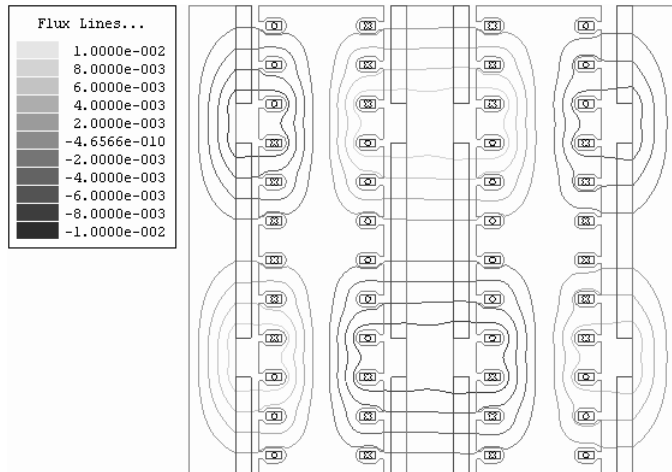


Figure 6.2: Transverse flux path through machine with an extended right-most airgap.

direction, either by using grain-oriented steel with the grain in the axial direction, or by making discrete teeth that would only allow flux to pass axially through to the end-rotor.

For single-stage machines it is clearly beneficial to have a single stator with a single set of coil groups sandwiched between two rotors. Coupling of two single-stage machines through some sort of mechanical drive-train in essence results in the same fundamental problem and is thus not advised.

Another topology that reduces the number of coil groups is to wind the coils toroidally around the stator core, as illustrated in figure 6.2. This demonstration model also has a larger right-most airgap but with toroidally-wound coils, the primary flux flows entirely through the stator winding. Although the increased airgap has resulted in a slight decrease in flux, all the coil groups in the second stator link with the same flux and hence the voltage drop is minimal.

Toroidally-wound machines have other benefits. Since the overhang is predominately determined by the axial thickness of the stator core and is generally less than in traditional axial-flux machines, higher efficiencies result. The trade-off is that the volume of material may be increased since the stator core width is now dependent on the core flux density. Although the core can still be made from coiled non-grain oriented steel, the equipment and process required to toroidally wind the coil groups makes this manufacturing process complex. An alternative method to install windings into slots may be with the use of folded coils as per figure 6.3, which

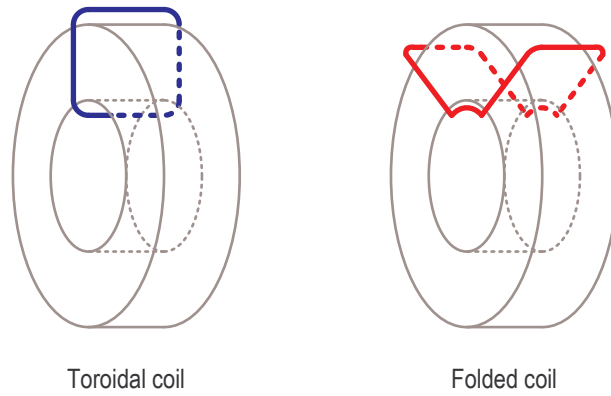


Figure 6.3: A toroidal flux path may be established from the use of (a) toroidal coils, (b) folded coils.

results in the same flux pattern but is significantly easier to wind than toroidal coils. The price though is a slight increase in overhang. Irrespectively, the design and evaluation of an equivalent-sized prototype would be a worthwhile exercise to further expand the knowledge-base of such machines.

Both topologies have their arguments behind their choice, all of which need consideration, based on their desired applications.

## References

- [1] F. Crescimbin F. Caricchi and O. Honorati. Modular Axial-Flux Permanent-Magnet Motor for Ship Propulsion Drives. *IEEE Transactions on Energy Conversion*, 14(3):673–679, September 1999.
- [2] F. Mezzetti F. Caricchi, F. Crescimbin and E. Santini. Multistage Axial-Flux PM Macine for Wheel Direct Drive. *IEEE Transactions on Industry Applications*, 32(4):882–888, July/August 1996.
- [3] J. Chan. Axial-Field Electrical Machines - Design and Applications. *IEEE Transactions on Energy Conversion*, EC-2(2):294–300, June 1987.
- [4] W. Leung and J. Chan. A new Design Approach for Axial-Field Electrical Machines. *IEEE Transactions on Power Apparatus and Systems*, PAS-99(4):1679–1685, July/August 1980.
- [5] D. Patterson and R. Spee. The Design and Development of an Axial Flux Permanent Magnet Brushless DC Motor for Wheel Drive in a Solar Powered Vehicle. *IEEE Transactions on Industry Applications*, 31(5):1054–1061, September/October 1995.
- [6] F. Profumo Z. Zhang and A. Tenconi. Analysis and Experimental Verification of Performance for an Axial Flux Permanent Magnet Brushless DC Motor with Powder Iron Metallurgy Cores. *IEEE Transactions on Magnetics*, 33(5):4194–4196, September 1997.
- [7] F. Crescimbin F. Caricchi and O. Honorati. Low-Cost Compact PM Machine for Adjustable-Speed Pump Application. *IEEE IAS*, 1:464–470, 1996.
- [8] P. Campbell. Principles of a Permanent Magnet Axial-Field DC Machine. *Proceedings of the IEE*, 121(12):1489–1494, December 1974.
- [9] V. Ramsden H. Lovatt and B. Mecrow. Design of an In-Wheel Motor for Solar-Powered Electric Vehicle. *IEE Proceedings - Electric Power Applications*, 145(5):402–408, September 1998.

- [10] N. Lombard and M. Kamper. Analysis and Performance of an Ironless Stator Axial Flux PM Machine. *IEEE Transactions on Energy Conversion*, 14(4):1051–1056, December 1999.
- [11] P. Campbell. The Magnetic Circuit of an Axial Field D.C. Electrical Machine. *IEEE Transactions on Magnetism*, Mag-11(5):1541–1543, September 1975.
- [12] R. Belmans R. Hanitsch and R. Stephan. Small Axial Flux Motor with Permanent Magnet Excitation and Etched Airgap Winding. *IEEE Transactions on Magnetism*, Vol. 30(2):592–594, March 1994.
- [13] P. Evans. Novel Disc-Motor Designs. *Proceedings of the IEE*, 125(5):416, May 1978.
- [14] F. Profumo Z. Zhang and A. Tenconi. Axial Flux Machines for Electric Vehicles. *Electric Machines and Power Systems Journal*, Vol. 24:883–896, May 1996.
- [15] F. Profumo C. Jensen and T. Lipo. A Low-Loss Permanent-Magnet Brushless DC Motor Utilizing Tape Wound Amorphous Iron. *IEEE Transactions on Industry Applications*, 28(3):646–651, May/June 1992.
- [16] E. Spooner and B. Chalmers. Torus’: A Slotless, Toroidal-Stator Permanent-Magnet Generator. *IEE Proceedings - B*, 139(6):497–506, November 1992.
- [17] A. van Zyl J. Braid and C. Landy. Design, Analysis and Development of a Multistage Axial-Flux Permanent Magnet Synchronous Machine. *IEEE Africon '02*, 2:675–680, October 2002.
- [18] J. Braid. Design and Development of a 20 W Axial Flux Machine with Printed Circuit Board Armature. *SAUPEC 2006*, 14(4):1051–1056, December 1999.
- [19] M. Say. *The Performance and Design of Alternating Current Machines*. Sir Isaac Pitman and Sons, London, 3rd edition edition, 1965.
- [20] A. Daniels. *Introduction to Electrical Machines*. The Macmillan Press Ltd, London, 1976.
- [21] T. Chan. Unity Power-Factor Controller for a Synchronous Motor. *IEEE Transactions on Industrial Electronics*, IE-34(3):325–330, August 1987.
- [22] T. Babu and D. O’Kelly. A Microprocessor-Based Load Angle Measurement System. *IEEE Transactions on Industrial Electronics*, IE-34(2):129–134, May 1987.
- [23] S. Ahson and M. Ali. A Microprocessor-Based Scheme for Torque-Angle and Speed Measurement. *IEEE Transactions on Industrial Electronics*, IE-34(2):135–138, May 1987.

# Appendix

## Prototype specifications and dimensions

Table 1: Specifications of prototype multi-stage machine.

<b>Parameter</b>	<b>Rating</b>
Power	5 kW
Speed	750 r.p.m.
Poles	8
Voltage	180 V
Current	10 A
Phases	3
Stages	2

Table 2: Dimensions of prototype multi-stage machine.

<b>Parameter</b>	<b>Dimension</b>
Outer diameter	245 mm
Inner diameter	142 mm
Airgap length	2 mm (revised to 4 mm)
Magnet thickness	5 mm
Rotor backiron	15 mm
Slots/pole/phase	2
Number of slots	48 per side
Conductors/slot	32
Slot width	5 mm parallel sided
Slot depth	15 mm
Magnet:Pole pitch	0.8

## Prototype pictures

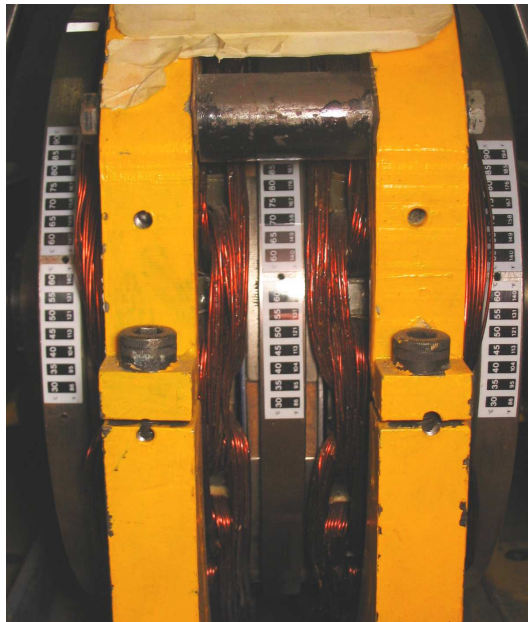


Figure 4: Coloured temperature strips on rotor backiron.



Figure 5: Holes in rotor backiron for insertion of temperature probes.

## Supporting graphs

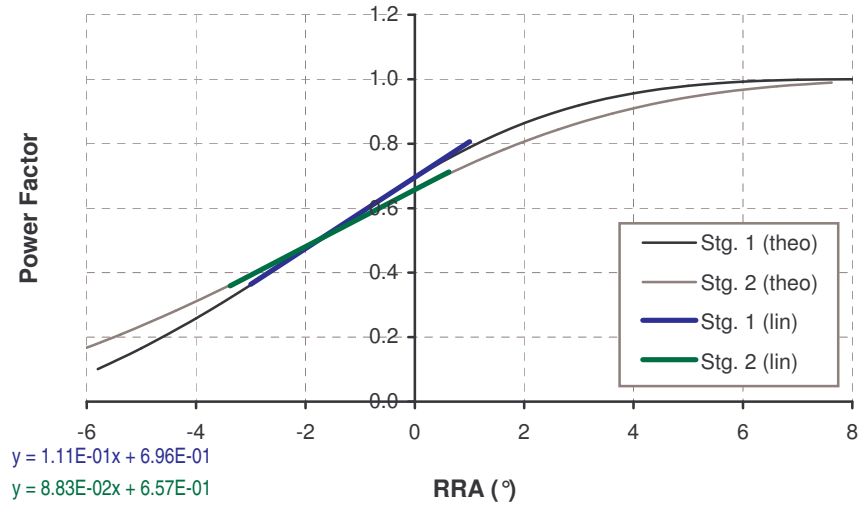


Figure 6: Power factor intersection point for CW rotation; by means of linear interpolation.

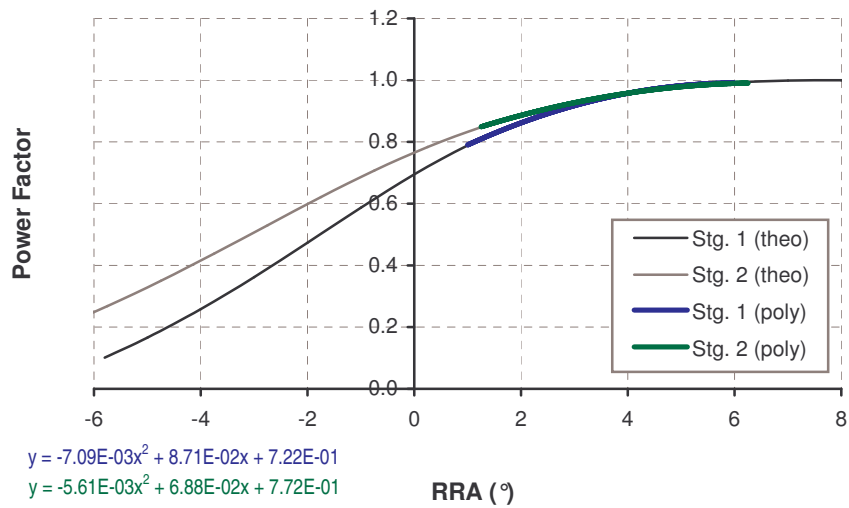


Figure 7: Power factor intersection point for CCW rotation; by means of quadratic interpolation.

## Instruments and equipment

### Parameter measurement instruments

Table 3: Instruments used to quantify the back EMF and winding resistance.

Measurement	Instrument	Serial number
Back EMF 1	Voltmeter, 300 V AC	3-22
Back EMF 2	Voltmeter, 300 V AC	3-23
Temperature	Tektronix thermocouple	MC 36
Resistance	Rhombic Ohmmeter	MC 302

### Generator experimental setup

Table 4: Principle equipment used in the generator experimental setup.

Apparatus	Type	Serial number
3-ph. inverter	45 kW, 380 V 3-phase	-
Sync. drive	25 HP slip-ring induc. mc.	-
DC field	220 V, 50 A variac	1-3
3-ph. variac	220 V, 50 A variac	2-1
Resistor bank	$3 \times 2$ kW, 220 V	1-2, 1-4, 2-3b

Table 5: Instruments used to record primary measurements during generator tests.

Measurement	Instrument	Type	Serial number
$V_L$	Voltmeter	300 V AC analogue	3-22
$A_L$	Ammeter	20 A AC analogue	2-47
$V_P$	Osc. scope	2 ms/div, 5 V/div	MC 403
$\sigma$	Tachometer	TTL Laser triggered	MC 405

## Motoring experimental setup

Table 6: Principle equipment used in motor experimental setup.

<b>Apparatus</b>	<b>Type</b>	<b>Serial number</b>
3-ph. variac	220 V, 10 A variac	4-3
3-ph. variac	220 V, 10 A variac	4-4
Sync. load	25 HP slip-ring induc. mc.	-
DC field	220 V, 50 A variac	1-3
3-ph. variac	220 V, 50 A variac	2-1
Resisor bank	$3 \times 2$ kW, 220 V	1-2, 1-4, 2-3b

Table 7: Instruments used to record primary measurements during motor tests.

<b>Measurement</b>	<b>Instrument</b>	<b>Type</b>	<b>Serial number</b>
$W_1$	Wattmeter	5 kW AC analogue	13-44
$W_2$	Wattmeter	5 kW AC analogue	13-45
$V_1$	Voltmeter	300 V AC analogue	3-22
$V_2$	Voltmeter	300 V AC analogue	3-23
$A_1$	Ammeter	20 A AC analogue	2-47
$A_2$	Ammeter	20 A AC analogue	2-48
$V_P$	Oscilloscope	2 ms/div, 5 V/div	MC 403
$\sigma$	Tachometer	TTL Laser triggered	MC 405

Table 8: Additional equipment used to perform inverter start.

<b>Apparatus</b>	<b>Type</b>	<b>Serial number</b>
3-ph. inverter	3.7 kW, 220 V 1-phase	-
Knife switch	$3 \times$ single phase 20 A	-
Synchro-scope	2 channel oscilloscope	MC 403

## Recorded experimental data

Table 9: Rotor backiron temperatures and corresponding back EMFs.

$E_{01-L}$ (V)	$E_{02-L}$ (V)	$T_1$ ( $^{\circ}\text{C}$ )	$T_2$ ( $^{\circ}\text{C}$ )
171	165	24	24
170	164	26	27
169	163	30	30
168	162	35	35
166	161	42	42
165	160	47	47
164	159	52	51
163	158	56	55
162	157	59	58

Table 10: Measurements recorded during generator tests, conducted at synchronous speed, for increasing load.

$I_L$ (A)	$E_{01-L}$ (V)	$E_{02-L}$ (V)	$\Delta$ ( $\mu\text{S}$ )
0.5	167	162	6
1.0	167	162	26
1.5	166	161	52
2.0	166	161	74
2.5	166	161	96
3.0	166	160	116
3.5	165	160	142
4.0	165	160	162
4.5	165	159	190
5.0	165	159	210
5.5	164	159	238
6.0	164	158	258
6.5	164	158	282
7.0	164	158	298
7.5	164	158	326
8.0	164	158	350
8.5	164	158	366
9.0	163	158	392
9.5	163	157	418
10.0	163	157	438

Table 11: Individual motoring tests, *Stage1*.

$I_1$ (A)	$P_1$ (kW)	$pf_1$	$E_{01-L}$ (V)
6.39	0.86	0.43	164
5.98	1.14	0.61	164
5.91	1.21	0.65	164
6.08	1.34	0.70	164
6.27	1.56	0.80	164
6.46	1.78	0.89	164
7.17	2.14	0.96	164
8.40	2.57	0.98	164
9.77	3.02	1.00	163

Table 12: Individual motoring tests, *Stage2*.

$I_2$ (A)	$P_2$ (kW)	$pf_2$	$E_{02-L}$ (V)
8.11	0.94	0.37	159
7.78	1.20	0.49	159
7.66	1.26	0.53	159
7.50	1.38	0.59	159
7.47	1.56	0.67	159
7.43	1.80	0.78	159
7.90	2.09	0.85	159
8.58	2.50	0.93	159
9.82	3.00	0.98	159

Table 13: Measurements recorded during motor tests with both stages connected in parallel, fed from a common 180 V supply, for increasing load. CW rotation.

$E_{01-L}$ (V)	$E_{02-L}$ (V)	$I_1$ (A)	$I_2$ (A)	$P_1$ (kW)	$P_2$ (kW)
163	158	7.10	8.46	0.49	0.74
163	158	6.85	8.21	0.60	0.84
163	158	6.81	8.17	0.65	0.88
163	158	6.77	8.13	0.72	0.95
163	158	6.59	7.94	0.81	1.03
163	158	6.42	7.77	0.93	1.14
163	157	6.21	7.54	1.06	1.26
162	157	6.37	7.65	1.24	1.42
162	157	6.38	7.58	1.44	1.60
162	157	6.45	7.55	1.62	1.77
162	157	6.75	7.71	1.86	1.98
162	157	7.23	7.97	2.14	2.22
162	157	7.82	8.40	2.36	2.44
162	157	8.58	9.10	2.62	2.68
162	157	8.79	9.18	2.72	2.77
161	156	8.94	9.29	2.77	2.82

Table 14: Measurements recorded during motoring tests with both stages connected in parallel, fed from a common 180 V supply, for increasing load. CCW rotation.

$E_{01-L}$ (V)	$E_{02-L}$ (V)	$I_1$ (A)	$I_2$ (A)	$P_1$ (kW)	$P_2$ (kW)
163	159	7.76	8.20	0.40	0.90
163	159	7.33	7.88	0.49	0.98
163	159	7.31	7.86	0.54	1.02
163	159	7.18	7.80	0.59	1.07
163	159	6.97	7.67	0.67	1.15
163	159	6.72	7.51	0.80	1.26
163	159	6.41	7.36	0.99	1.45
162	158	6.28	7.33	1.14	1.58
162	158	6.17	7.33	1.34	1.77
162	158	6.36	7.58	1.58	1.99
162	158	6.81	8.04	1.84	2.22
162	158	7.21	8.40	2.08	2.43
162	158	7.81	8.95	2.34	2.67
162	158	8.53	9.59	2.62	2.93
162	158	9.03	10.03	2.80	3.09
162	158	9.10	10.08	2.83	3.12

Table 15: Measurements recorded during motor tests with both stages connected in parallel, fed from a common 180 V supply, for increasing load. CW rotation.

$E_{01}$ (V)	$E_{02}$ (V)	$I_1$ (A)	$I_2$ (A)	$P_1$ (kW)	$P_2$ (kW)	$pf_1$	$pf_2$	$\Delta$ ( $\mu$ S)
162	157	7.65	9.45	0.53	0.82	0.22	0.28	0
162	157	7.38	9.18	0.63	0.90	0.27	0.32	32
162	157	7.29	9.10	0.68	0.96	0.30	0.34	44
162	157	7.15	8.96	0.73	1.02	0.33	0.36	62
162	157	6.97	8.78	0.84	1.12	0.39	0.41	90
162	157	6.77	8.57	0.94	1.22	0.45	0.46	120
162	157	6.59	8.39	1.09	1.37	0.53	0.52	162
162	157	6.45	8.20	1.26	1.53	0.62	0.60	206
162	157	6.52	8.21	1.47	1.74	0.72	0.68	252
162	157	6.60	8.19	1.65	1.91	0.80	0.75	310
162	157	6.77	8.21	1.86	2.11	0.88	0.83	374
162	157	7.24	8.49	2.14	2.38	0.95	0.90	452
162	157	7.90	9.05	2.41	2.65	0.97	0.94	510
162	157	8.56	9.60	2.63	2.87	0.98	0.96	562
162	157	8.95	9.92	2.78	3.01	0.99	0.97	598
162	156	9.07	10.02	2.82	3.05	0.99	0.97	616

Table 16: Measurements recorded during motor tests with both stages connected in parallel, fed from a common 180 V supply, for increasing load. CCW rotation.

$E_{01}$ (V)	$E_{02}$ (V)	$I_1$ (A)	$I_2$ (A)	$P_1$ (kW)	$P_2$ (kW)	$pf_1$	$pf_2$	$\Delta$ ( $\mu$ S)
162	158	8.67	9.67	0.46	0.96	0.17	0.32	0
162	158	8.32	9.39	0.57	1.07	0.22	0.37	32
162	158	8.20	9.30	0.61	1.11	0.24	0.38	46
162	158	7.99	9.13	0.66	1.17	0.27	0.41	62
162	158	7.79	9.00	0.75	1.26	0.31	0.45	88
162	158	7.63	8.92	0.89	1.39	0.37	0.50	114
162	158	7.37	8.75	1.02	1.54	0.44	0.56	150
162	158	7.14	8.62	1.19	1.70	0.54	0.63	194
162	158	6.97	8.57	1.39	1.90	0.64	0.71	240
162	158	7.11	8.79	1.60	2.12	0.72	0.77	290
162	158	7.23	8.97	1.83	2.35	0.81	0.84	354
162	157	7.48	9.26	2.10	2.61	0.90	0.91	426
162	157	7.91	9.68	2.34	2.85	0.95	0.94	488
162	157	8.46	10.20	2.58	3.08	0.98	0.97	548
162	157	9.17	10.80	2.82	3.32	0.98	0.98	604